ANALYSIS OF THE HERSCHEL/HIFI 1.2 THZ WIDE SPECTRAL SURVEY OF THE ORION KLEINMANN-LOW NEBULA

by

Nathan R. Crockett

A dissertation submitted in partial fulfillment
of the requirements for the degree of
Doctor of Philosophy
(Astronomy and Astrophysics)
in The University of Michigan
2013

Doctoral Committee:

Professor Edwin A. Bergin, Chair
Professor John R. Barker
Professor Geoffrey A. Blake
Professor Nuria Calvet
Emeritus Professor Charles R. Cowley
Professor Eric Herbst

For my family...

ACKNOWLEDGMENTS

I would like to express my sincere gratitude to my advisor, Ted Bergin, who over the past four years has become a trusted mentor. I am deeply thankful for his guidance, scientific insights, enthusiasm, and patience during my time at the University of Michigan. He has been more than generous with his time and resources, and has supported and challenged me to perform at my best. A big thank you also to the rest of my committee, John Barker, Geoffrey Blake, Nuria Calvet, Charles Cowley, and Eric Herbst for their invaluable input in shaping the work presented in this dissertation. I wish also to express appreciation to members of the Bergin "Nerd Club", past and present, who have provided me with advice and support in matters related and unrelated to astronomy. In no particular order: Shiya Wang, Jeffrey Fogel, Sarah Ragan, Ruud Visser, Melissa McClure, Ilse Cleeves, Justin Neill, and Cécile Favre.

I would like to extend special thanks to Peter Schilke and Darek Lis who provided both expertise and technical support which made this dissertation possible. Thank you also to John Black for providing valuable advice and support in analyzing molecular line observations. In matters of data reduction, I owe a great debt of gratitude to members of the HIFI Instrument Control Center, where I spent 2 months, along with a number of other graduate students, learning how to reduce HIFI data.

I would like to acknowledge here the individuals who participated in the full band analysis of the Orion KL HIFI spectral survey: Edwin Bergin, Justin Neill, Cécile Favre, Peter Schilke, Dariusz C. Lis, Tom Bell, Geoff Blake, José Cernicharo, Martin Emprechtinger, Gisela B. Esplugues, Harshal Gupta, Maria Kleshcheva, Steven Lord, Nuria Marcelino, Brett McGuire, John Pearson, Thomas G. Phillips, Rene Plume, Floris van der Tak, Belén Tercero, and Shanshan Yu. Their efforts made this project

possible over a reasonable timescale.

A special thank you also to Joan Najita and Stephen Strom, with whom I worked at NOAO before attending the University of Michigan. Their energy and passion for science will always be an inspiration. I would also like to acknowledge Michael Meyer and Donald Garnett, both of whom advised me as an undergraduate at the University of Arizona. They were superb role models. Thanks for showing me the ropes.

Thank you to Sasha Muratov, Mike Anderson, Mark Haynes, Tina Hsu, Joel Lamb, Sarah Barbrow, John Prensner, Erin Rhode, Lou Chang, Maggie Dyer, Robin Stottlemyer, and Josh Brammer for their friendship, advice, and support. My deepest gratitude and love go to my girlfriend Shannon Chase. Finally, I would like to thank my father and mother, Kenneth and Teresa Crockett, as well as my brother and sister-in-law, Aaron and Amanda Crockett, for their support and love over the years.

Chapter 2 of this dissertation is based on an article in Astronomy & Astrophysics (Crockett et al., 2010), which is slightly modified and reproduced here with permission. Chapters 3 and 5 are based on publications to be submitted to the Astrophysical Journal (Crockett et al. 2013a,b, in preparation). Chapter 4 is based on a publication recently submitted to the Astrophysical Journal (Crockett et al. 2013, submitted).

HIFI has been designed and built by a consortium of institutes and university departments from across Europe, Canada and the United States under the leadership of SRON Netherlands Institute for Space Research, Groningen, The Netherlands and with major contributions from Germany, France and the US. Consortium members are: Canada: CSA, U.Waterloo; France: CESR, LAB, LERMA, IRAM; Germany: KOSMA, MPIfR, MPS; Ireland, NUI Maynooth; Italy: ASI, IFSI-INAF, Osservatorio Astrofisico di Arcetri-INAF; Netherlands: SRON, TUD; Poland: CAMK, CBK; Spain: Observatorio Astronómico Nacional (IGN), Centro de Astrobiología (CSIC-INTA). Sweden: Chalmers University of Technology - MC2, RSS & GARD; Onsala Space Observatory; Swedish National Space Board, Stockholm University - Stockholm Observatory; Switzerland: ETH Zurich, FHNW; USA: Caltech, JPL, NHSC. HIPE is a joint development by the Herschel Science Ground Segment Consortium,

consisting of ESA, the NASA Herschel Science Center, and the HIFI, PACS and SPIRE consortia. Support for this work was provided by NASA through an award issued by JPL/Caltech.

CONTENTS

LIST OF FIGURES

Figure

LIST OF TABLES

Table

LIST OF APPENDICES

Appendix

ABSTRACT

This dissertation presents a comprehensive analysis of a broad band spectral line survey of the Orion Kleinmann-Low nebula (Orion KL), one of the most chemically rich regions in the Galaxy, using the HIFI instrument on board the *Herschel* Space Observatory. This survey spans a frequency range from 480 to 1907 GHz at a resolution of 1.1 MHz. These observations thus encompass the largest spectral coverage ever obtained toward this massive star forming region in the sub-mm with high spectral resolution, and include frequencies $\gtrsim$ 1 THz where the Earth's atmosphere prevents observations from the ground. In all, we detect emission from 36 molecules (76 isotopologues). Combining this dataset with ground based mm spectroscopy obtained with the IRAM 30 m telescope, we model the molecular emission assuming local thermodynamic equilibrium (LTE). Because of the wide frequency coverage, our models are constrained over an unprecedented range in excitation energy, including states at or close to ground up to energies where emission is no longer detected. A χ^2 analysis indicates that most of our models reproduce the observed emission well. In particular complex organics, some with thousands of transitions, are well fit by LTE models implying that gas densities are high ($> 10^6$ cm^{-3}) and excitation temperatures and column densities are well constrained. Molecular abundances are computed using H_2 column densities also derived from the HIFI survey. The rotation temperature distribution of molecules detected toward the hot core is much wider relative to the compact ridge, plateau, and extended ridge. We find that complex N-bearing species, cyanides in particular, systematically probe hotter gas than complex O-bearing species. This indicates complex N-bearing molecules may be more difficult to remove from grain surfaces or that hot gas phase formation routes are important for these species. We also present a detailed non-LTE analysis of H_2S emission toward the hot core which

suggests this light hydride may probe heavily embedded gas in close proximity to a hidden self-luminous source (or sources), conceivably responsible for Orion KL's high luminosity. The abundances derived here, along with the publicly available data and molecular fits, represent a legacy for comparison to other sources and chemical models.

CHAPTER 1

Introduction

Over 150 molecules have been detected in the interstellar medium (ISM; Menten & Wyrowski, 2011) indicating a rich and intricate chemistry is at work in space. Fig. 1.1 is a screenshot taken from the University of Köln website[1] listing all of the molecules detected in the ISM. Most of these species are detected in the gas phase via rotation or vibration transitions in the mm, sub-mm, and infrared. The table shows that simple 2 – 4 atom molecules are common in the ISM, some of which contain only metals (e.g. OCS, NS, etc.) while others are highly saturated (e.g. H_2O, NH_3, etc.). The table also shows that organics, i.e. molecules containing carbon, are the most common species detected in the ISM. Astronomers typically label molecules with 6 atoms or more "complex" (Herbst & van Dishoeck, 2009), which, as illustrated in Fig. 1.1, make up approximately a third of all molecules detected in space. How this complexity develops is still not well understood, though it is clearly associated with stellar birth. Furthermore, complex organics are found in meteorites and cometary material that seeded the young forming Earth. These organics formed via pathways related to those operative during the star formation process, perhaps with an initial contribution from the ISM. Thus the study of organics in space is of intrinsic interest and clear astrobiological import. Theoretical chemical models have explored both gas phase and grain surface formation mechanisms, which are strongly tied to the local environment (see e.g. Millar et al., 1991; Charnley et al., 1992; Caselli et al., 1993; Rodgers & Charnley, 2001; Garrod & Herbst, 2006; Garrod et al., 2008).

So called "hot cores", the birth sites of massive stars, are the most prodigious

[1] http://www.astro.uni-koeln.de/cdms/molecules

emitters of molecular line radiation in the Galaxy, displaying emission from many of the organics listed in Fig. 1.1. These regions are essentially the dense gas in close proximity to massive stars. The local gas undergoes heating from the star which can release the products of icy grain mantles that formed during earlier stages and drive gas phase pathways that were previously inactive, leading to a rich chemical composition. Such regions are thus the best places to study how chemical complexity develops in the ISM. Studying the molecular content of these regions constrains chemical models that trace the evolution of hot cores. This dissertation presents a study of the chemical inventory of one of the most chemically rich massive star forming regions in the Milky Way, the Kleinmann-Low Nebula within the Orion Molecular Cloud (Orion KL), using an unbiased spectral line survey, i.e. a broadband spectrum focused on observing a continuous frequency interval as opposed to particular molecules, obtained using the HIFI spectrometer on board the *Herschel* space observatory.

1.1 Orion KL: A Brief overview

Because of its close distance (414 pc; Menten et al. 2007), high luminosity ($L \sim 10^5$ $L_\odot$; Wynn-Williams et al. 1984), and rich molecular line emission, Orion KL is an archetypal massive star forming region in the Milky Way. Orion KL was first discovered as the brightest continuum source at 22 μm within the Orion Molecular Cloud (Kleinmann & Low, 1967). This region is located approximately $1'$ NW of the Trapezium cluster and lies within $\sim 10 - 15''$ of the Becklin-Neugebauer (BN) object, another bright continuum source in the mid-IR (Becklin & Neugebauer, 1967). Subsequent observations in the IR showed that the KL region breaks up into a number of smaller infrared clumps, labelled "IRc" sources (Rieke et al., 1973; Gezari et al., 1998). Fig. 1.2 plots recently obtained SOFIA continuum images of Orion KL taken with the FORCAST camera at 7.7, 19.7, 31.5, and 37.1 μm from De Buizer et al. (2012). The locations of IRc sources are marked on the maps with white circles. From these plots, the elaborate physical structure of Orion KL is readily apparent.

Single dish spectral line surveys in the mm (Johansson et al., 1984; Sutton et al.,

1985; Blake et al., 1987; Turner, 1989; Greaves & White, 1991; Ziurys & McGonagle, 1993; Lee et al., 2001; Lee & Cho, 2002; Goddi et al., 2009b; Tercero et al., 2010, 2011) and sub-mm (Jewell et al., 1989; Schilke et al., 1997, 2001; White et al., 2003; Comito et al., 2005; Olofsson et al., 2007; Persson et al., 2007) reveal a rich chemical composition dominated by complex organics, which has motivated many theoretical studies of complex chemistry in the ISM (see e.g. Millar et al., 1991; Charnley et al., 1992; Caselli et al., 1993; Rodgers & Charnley, 2001; Garrod & Herbst, 2006; Garrod et al., 2008). Several molecular components are detected toward Orion KL. Though they are not spatially resolved by the single dish observations, emission from these components can be separated because they have characteristic line profiles that are significantly different from one another (Blake et al., 1987). In addition, interferometric observations have mapped the spatial distributions of these components using different molecular tracers (see e.g. Beuther et al., 2005, 2006; Friedel & Snyder, 2008; Wang et al., 2010; Goddi et al., 2011; Favre et al., 2011; Peng et al., 2012; Brouillet et al., 2013). These studies reveal the presence of an intricate temperature and density structure on scales $< 1 - 2''$. Line profiles are parameterized by the line center velocity relative to the Local Standard of Rest, v_{lsr}, and the full line width at half maximum, Δv. These so called spatial/velocity components are listed below, with typical values for v_{lsr}, Δv, and rotation temperature, T_{rot}, taken from Blake et al. (1987):

1. The extended ridge ($v_{lsr} \approx 9$ km/s, $\Delta v \approx 4$ km/s) corresponds to widespread, quiescent gas. Rotation temperatures measured toward the extended ridge are low ($T_{rot} \lesssim 60$ K) compared to the other spatial/velocity components. The extended ridge is rich in unsaturated, carbon rich species indicating the dominance of exothermic ion-molecule reactions that do not require activation energies (Herbst & Klemperer, 1973; Watson, 1973; Smith, 1992).

2. The hot core ($v_{lsr} \approx 3 - 5$ km/s, $\Delta v \approx 5 - 10$ km/s) is the hottest component observed toward Orion KL. Rotation temperatures toward this component can exceed 300 K. The hot core is rich in complex organic emission, particularly

N-bearing species, perhaps indicating an active warm gas-grain chemistry (see e.g. Caselli et al., 1993; Rodgers & Charnley, 2001; Garrod & Herbst, 2006; Garrod et al., 2008).

3. The compact ridge ($v_{lsr} \approx 7 - 8$ km/s, $\Delta v \approx 3 - 5$ km/s) is a group of externally heated clumps located $\sim 12''$ SW of the hot core (Wang et al., 2011; Favre et al., 2011). Rotation temperatures are typically close to 100 K. The compact ridge is also a strong emitter of complex organics indicating, like the hot core, that warm gas-grain chemistry is important (see e.g. Caselli et al., 1993; Rodgers & Charnley, 2001; Garrod & Herbst, 2006; Garrod et al., 2008). The compact ridge, however, is much richer in complex O-bearing organics (Blake et al., 1987).

4. The plateau ($v_{lsr} \approx 7 - 8$ km/s, $\Delta v \gtrsim 20$ km/s) collectively refers to two outflow components called the low velocity flow (LVF) and high velocity flow (HVF). The LVF and HVF are oriented along NE – SW (Genzel & Stutzki, 1989; Blake et al., 1996; Stolovy et al., 1998; Greenhill et al., 1998; Nissen et al., 2007; Plambeck et al., 2009; Goddi et al., 2009a) and NW – SE (Allen & Burton, 1993; Chernin & Wright, 1996; Schultz et al., 1999; O'dell, 2001; Doi et al., 2002; Nissen et al., 2012) axes, respectively, perpendicular to one another. Rotation temperatures vary approximately between 100 and 150 K.

Fig. 1.3 plots the $3_{2,1} - 3_{1,2}$ transition of HDO within the HIFI spectral survey of Orion KL with Gaussian profiles fit to different spatial/velocity components. The red, green, and blue Gaussians correspond to the hot core, plateau, and compact ridge, respectively. The yellow dashed line is the sum of these Gaussians. From the figure, we see that the different spatial/velocity components can be separated using the high spectral resolution of HIFI even though they are not spatially resolved by *Herschel*.

The ultimate power source behind Orion KL remains a mystery. Both Downes et al. (1981) and Wynn-Williams et al. (1984) showed that most of the IR clumps were externally heated. They argued the high total luminosity they measured to-

ward Orion KL (L $\sim$10^5 L$_\odot$), likely originated from IRc2, the brightest IRc source in the mid-IR ($\lambda \lesssim 13$ μm). Higher spatial resolution observations in the near-IR presented by Dougados et al. (1993), however, showed that IRc2 breaks up into four smaller components, some of which may not be self-luminous (Robberto et al., 2005). Gezari et al. (1998), furthermore, re-computed the total luminosity for IRc2 to be L $\sim$ 1000 L$_\odot$, two orders of magnitude lower than the nominal Orion KL luminosity computed by Wynn-Williams et al. (1984), using higher spatial resolution IR observations. It is thus currently thought that most, if not all, of the IRc sources are emitting reprocessed radiation originating from some, as of yet, unidentified heavily embedded source or sources.

If IRc2 does not harbor a massive protostar, then what is powering Orion KL? One possibility is that radio source I, which has no IR counterpart and is located $\lesssim 1''$ south of IRc2, is supplying the luminosity. Source I is coincident with a cluster of SiO masers (Menten & Reid, 1995). Because such masers have only been detected toward very luminous stars (L $\gtrsim 10^4$ L$_\odot$), this strongly suggests the presence of a highly embedded energetic source. Okumura et al. (2011), furthermore, observe a 7.8/12.4 μm color temperature peak toward source I indicating the presence of a self luminous source. Source I is also located at the center of the LVF implying that this source is indeed a high mass protostar which could drive this outflow (Greenhill et al., 2004b; Beuther & Nissen, 2008; Plambeck et al., 2009). Other possible self-luminous sources which may be important for this peculiar region are source n (Lonsdale et al., 1982), which is only strongly detected at wavelengths $\lesssim 3.8$ μm, and like source I, has a radio counterpart (Menten & Reid, 1995) and the sub-mm source SMA1 (Beuther et al., 2004), toward which strong vibrationally excited lines of CH_3OH, SO_2, and HC_3N have been detected (Beuther et al., 2005). Additionally, 19.7/31.5 μm and 31.5/37 μm color temperature maps derived from the SOFIA observations shown in Fig. 1.2 reveal a color temperature peak at the position of IRc4, indicating the possibility of an embedded self-luminous source at that location (De Buizer et al., 2012). Finally, Zapata et al. (2011) proposed that the Orion hot core is heated externally via outflowing material from an "explosive event", perhaps a stellar merger

involving Source I and the BN object, which occurred approximately 500 years ago. At present time, therefore, the source or sources responsible for Orion KL's high luminosity is still a topic of debate.

1.2 Contribution of HIFI: A Homogeneous Wide Band Spectral Survey

This dissertation presents a comprehensive analysis of the HIFI 1.2 THz wide spectral survey toward Orion KL. HIFI is the high resolution spectrometer on board the *Herschel* space observatory and provides near continuous coverage between 470 and 1907 GHz. Fig. 1.4 (bottom panel) plots the full HIFI scan toward Orion KL with the atmospheric transmission plotted in the upper panel. From the plot, we see that HIFI provides frequency coverage beyond 1 THz as well as several other sub-mm regions that are completely inaccessible from the ground because of atmospheric absorption. Such spectral coverage, $\nu > 1$ THz in particular, represented a *terra incognita* for high resolution spectral surveys. Because many of the molecules listed in Fig. 1.1 were first detected toward Orion KL, this source is a logical choice for an unbiased exploration of these spectral regions.

Because of its wide bandwidth, the HIFI scan is an ideal tool for obtaining the chemical inventory of Orion KL. The entire spectrum, moreover, is obtained with the same instrument, meaning the relative calibration between lines has a high degree of fidelity. Multi transitional studies, therefore, can be reliably carried out using an unprecedented number of lines. This is true not only for complex organics, but also for species with more widely spaced transitions, especially molecules with large numbers of lines at frequencies higher than 1 THz, i.e. light hydrides such as H_2O and H_2S.

1.3 Molecules as Physical Probes

Analysis of molecular line data can provide important constraints on the density, temperature, and local radiation field within molecular gas. In this section, we de-

scribe the methods typically used to interpret sub-mm spectra and applied in this dissertation.

1.3.1 The Assumption of LTE

When analyzing molecular line emission it is often convenient to assume local thermodynamic equilibrium (LTE). This means the gas density is high enough for collisions to dominate the excitation and de-excitation of a given molecule, with all energy levels thermalized to a single excitation temperature equal to the kinetic temperature of the gas. Using the Boltzmann equation, this assumption leads to the following equation,

$$\frac{N_u}{g_u} = \frac{N_{tot}}{Q(T_{ex})} e^{-E_u/kT_{ex}}. \tag{1.1}$$

where N_u is the upper state column density, g_u is the statistical weight, N_{tot} is the total column density, E_u is the upper state energy, T_{ex} is the excitation temperature, and $Q(T_{ex})$ is the partition function. Taking the natural logarithm of both sides of Eq. 1.1 yields,

$$ln\left(\frac{N_u}{g_u}\right) = ln\left[\frac{N_{tot}}{Q(T_{ex})}\right] - E_u/kT_{ex}, \tag{1.2}$$

If a molecule is in LTE then plotting the left hand side of Eq. 1.2 versus E_u will yield a straight line. Such a plot is known as a rotation diagram and is useful because T_{ex} and N_{tot} can be derived from the slope and y-intercept, respectively. The temperature derived from this type of plot is often referred to as a rotation temperature, T_{rot}.

Plotting a rotation diagram requires upper state column density measurements, which can be derived directly from molecular line data. Assuming $T_{ex} >> T_{bg}$, where T_{ex} is the excitation temperature and T_{bg} is the background temperature, Goldsmith & Langer (1999) derive the following equation relating N_u, to the integrated intensity (in velocity space) of a spectral line, $\int T d\mathrm{v}$,

$$N_u = \frac{8\pi k\nu^2}{hc^3 A_{ul}} \frac{\int T d\mathrm{v}}{\eta_{bf}} \left(\frac{\tau}{1-e^{-\tau}}\right). \tag{1.3}$$

Here, ν is the frequency, k is Boltzmann's constant, c is the speed of light, τ is the optical depth of the line at center, and η_{bf} is a beam filling factor which corrects for

beam dilution. The beam filling factor is often estimated assuming both the telescope beam and source have Gaussian profiles,

$$\eta_{bf} = \frac{\theta_s^2}{\theta_s^2 + \theta_b^2}. \tag{1.4}$$

Here, θ_s and θ_b are the FWHM sizes of the source and telescope beam, respectively. Looking at Eq. 1.3, we see that upper state column densities are most easily derived for optically thin lines ($\tau << 1$) because the expression in parentheses is approximately 1. In instances when optically thick emission is suspected, one must estimate the optical depth. For species that contain resolvable hyperfine structure (e.g. NH_3), this can be done by comparing the observed intensities of these components. One can also estimate τ if multiple isotopologues are observed for the same transition. This, however, requires that an isotopic ratio be assumed.

Rotation diagrams are commonly used to analyze unbiased spectral surveys because it is a convenient and straight forward way to estimate temperature and column density. Alternatively, one can use a solution to the radiative transfer equation to model the emission directly assuming LTE level populations. Two recent spectral survey studies have adopted this approach: one toward Orion KL (Comito et al., 2005) and one toward the high mass star forming region NGC 6334 (Zernickel et al., 2012). The program these studies used, and is also employed here to perform the modeling, is XCLASS, which uses the one dimensional solution to the radiative transfer equation assuming a single temperature,

$$T_A(\nu) = \sum_m \sum_c \eta_{bf}(\theta_{m,c})[J(T_{ex}^{m,c}) - J(T_{bg})](1 - e^{-\tau(\nu)^{m,c}})e^{-\tau_d}. \tag{1.5}$$

Here $T_A(\nu)$ is the antenna temperature, $\tau(\nu)$ is the optical depth of the line, $\tau_{\rm d}$ is the optical depth of the dust, T_{ex} is the excitation temperature, T_{bg} is the background temperature, and J is the source function defined as,

$$J(T, \nu) = \frac{h\nu}{k}\left(e^{h\nu/kT} - 1\right)^{-1}. \tag{1.6}$$

The indices m and c correspond to the molecule and component, with the total spectrum being the sum. Assuming LTE the optical depth of each transition, designated with index l, is governed by a single $\mathrm{T_{ex}}$ computed using the equation,

$$\tau(\nu)_l^{m,c} = \frac{c^3}{8\pi\nu^3}(A_{ul}N_{tot}^{m,c})\frac{g_l e^{-E_l/kT_{ex}^{m,c}}}{Q(m,T_{ex}^{m,c})}\left(1-e^{-h\nu/kT_{ex}^{m,c}}\right)\phi(\nu)^{m,c} \tag{1.7}$$

Where the total optical depth over the entire spectrum for a given molecule and component is,

$$\tau(\nu)^{m,c} = \sum_l \tau(\nu)_l^{m,c} \tag{1.8}$$

and ϕ defines a Gaussian profile for the line,

$$\phi(\nu)^{m,c} = \frac{2\sqrt{ln2}}{\sqrt{\pi}\Delta \mathrm{v}^{\mathrm{m,c}}} exp\left[-\frac{(\nu-(\nu_l+\nu_{lsr}^{m,c}))^2}{2\sigma^2}\right]. \tag{1.9}$$

Here, Δv is the line full width at half maximum, ν_l is the rest frequency of the line, ν_{lsr} is the line offset, and σ is the standard deviation of the Gaussian profile in frequency space, that is $\sigma = 0.425(\nu_l/c)\Delta\mathrm{v}$.

The dust optical depth is parameterized by a power law,

$$\tau_d = 2\mathrm{m_H}(\chi_{\mathrm{dust}})\mathrm{N_{H_2}}\kappa_{1.3\mathrm{mm}}\left(\frac{\nu}{230\ \mathrm{GHz}}\right)^{\beta}, \tag{1.10}$$

where $\mathrm{N_{H_2}}$ is the column density of $\mathrm{H_2}$, m_H is the mass of a hydrogen atom, χ_{dust} is dust to gas mass ratio, and $\kappa_{1.3\mathrm{mm}}$ is the dust opacity at 1.3 mm (230 GHz). We assume here that $\chi_{dust} = 0.01$ and $\beta = 2$.

In the optically thin limit, rotation diagrams and LTE spectral modeling are equivalent. Fig. 1.5 (left column) plots a CH_3OH Q-branch near 830 GHz as modeled by the XCLASS program. Q-branches are useful because transitions in these bands cover a large range in excitation energy over a small frequency interval. The band plotted in Fig. 1.5 covers a range in E_u from $\sim$ 100 – 1100 K. The upper and lower panels plot models for $\mathrm{T_{ex}} = \mathrm{T_{rot}} = 100$ and 300 K, respectively. The panels in the right column plot the equivalent rotation diagrams. From the figure, we clearly see

that the shape of the Q-branch changes for the two temperature cases, an advantage provided by broad band data. The rotation temperature can thus be readily derived. In large part, the column density governs the overall intensity level as long as the lines are optically thin.

1.3.2 Non-LTE Conditions

The density, n_{H_2}, required to achieve LTE is called the critical density, n_c, and can be estimated by taking the ratio of the collision rate, C_{ul}, (in units of cm^3 s^{-1}) and the Einstein coefficient for spontaneous decay, A_{ul}, (in units s^{-1}) for a given state,

$$n_c = \frac{A_{ul}}{C_{ul}} \tag{1.11}$$

The indices u and l indicate the upper and lower state, respectively. If $n_{H_2} << n_c$, then LTE is not a good approximation. In these instances, computer codes that solve the equations of statistical equilibrium are needed to accurately model molecular line data. Such codes require knowledge of the collision rates, which do not exist for the vast majority of complex organics detected in the ISM. C_{ul} values must therefore be estimated or LTE assumed. Recently, MADEX, a non-LTE code, has been used to model emission from specific molecules with collision rates in a mm spectral survey toward Orion KL (Tercero et al., 2010, 2011). RADEX (van der Tak et al., 2007) is another publicly available non-LTE code that is often used to model molecular line data, which is applied in Chapter 4 of this dissertation.

Using more advanced non-LTE codes to model molecular line data is desirable if LTE conditions are not met because they yield more accurate column density measurements and place constraints on the density of the emitting gas. The rotation and inversion transitions of ammonia, for example, have Einstein A coefficients of order 10^{-2} and 10^{-7} s^{-1}, respectively. Collision rates for both types of transitions are roughly 5×10^{-11} cm^3 s^{-1}. Critical densities for the NH_3 rotation transitions are thus roughly 5 orders of magnitude higher than the inversion transitions. Fig. 1.6 plots the predicted peak intensities of the NH_3 (4,4) inversion and $2_1^- - 1_1^+$ rotation

transitions as a function of density as predicted by RADEX. From the plot, we see that the inversion transition is thermalized at a density of $\sim 10^5$ cm^{-3} while the rotation transition isn't until $\sim 10^8$ cm^{-3}. The inversion transition thus becomes insensitive to the density of the gas for $n_{H_2} \gtrsim 10^4$ cm^{-3}. Though LTE is not a good approximation when $n_{H_2} \lesssim 10^8$ cm^{-3} for the rotation transition, it is sensitive to the density of the gas and can be used as a robust tracer of gas density.

1.4 Goals and Organization of the Dissertation

In this dissertation, I present a comprehensive analysis of the *Herschel*/HIFI 1.2 THz wide spectral survey toward Orion KL. In Chapter 2, I present initial analysis of the Orion KL HIFI spectrum at frequencies > 1 THz. I note the number of observed emission lines is significantly lower at THz frequencies compared to mm and sub-mm wavelengths and discuss possible reasons for this drop off in line density. In Chapter 3, I present the full band analysis of the entire Orion KL HIFI spectrum. Our analysis indicates that 1.7×10^4 lines are detected over the entire spectrum originating from 36 molecules (76 isotopologues). I report column densities, rotation temperatures, and molecular abundances for most molecules based on XCLASS LTE model fits. A $\chi^2_{\rm red}$ analysis indicates excellent agreement between the data and models for most species. In Chapter 4, I present a detailed non-LTE analysis of H_2S emission toward the hot core using RADEX, which indicates H_2S is probing very dense gas ($n_{H_2} \gtrsim 5 \times 10^7$ cm^{-3}). The most highly excited states, furthermore, require a far-IR radiation field that is enhanced by a factor of 8 relative to what is observed, suggesting an origin in close proximity to a heavily embedded source. In Chapter 5, I discuss some of the chemical implications of the full band models reported in Chapter 3. I specifically discuss possible origins of the markedly hot cyanides detected toward the hot core. In Chapter 6, I present conclusions and discuss future work.

2 atoms	3 atoms	4 atoms	5 atoms	6 atoms	7 atoms	8 atoms	9 atoms	10 atoms	11 atoms	12 atoms	>12 atoms
H_2	C_3 *	*c*-C_3H	C_5 *	C_5H	C_6H	CH_3C_3N	CH_3C_4H	CH_3C_5N	HC_9N	*c*-C_6H_6 *	$HC_{11}N$
AlF	C_2H	*l*-C_3H	C_4H	*l*-H_2C_4	CH_2CHCN	$HC(O)OCH_3$	CH_3CH_2CN	$(CH_3)_2CO$	CH_3C_6H	$C_2H_5OCH_3$?	C_{60} * 2012
AlCl	C_2O	C_3N	C_4Si	C_2H_4*	CH_3C_2H	CH_3COOH	$(CH_3)_2O$	$(CH_2OH)_2$	C_2H_5OCHO	*n*-C_3H_7CN	C_{70} *
C_2**	C_2S	C_3O	*l*-C_3H_2	CH_3CN	HC_5N	C_7H	CH_3CH_2OH	CH_3CH_2CHO			
CH	CH_2	C_3S	*c*-C_3H_2	CH_3NC	CH_3CHO	C_6H_2	HC_7N				
CH^+	HCN	C_2H_2*	H_2CCN	CH_3OH	CH_3NH_2	CH_2OHCHO	C_8H				
CN	HCO	NH_3	CH_4 *	CH_3SH	*c*-C_2H_4O	*l*-HC_6H *	$CH_3C(O)NH_2$				
CO	HCO^+	HCCN	HC_3N	HC_3NH^+	H_2CCHOH	CH_2CHCHO (?)	C_8H^-				
CO^+	HCS^+	$HCNH^+$	HC_2NC	HC_2CHO	C_6H^-	CH_2CCHCN	C_3H_6				
CP	HOC^+	HNCO	HCOOH	NH_2CHO		H_2NCH_2CN					
SiC	H_2O	HNCS	H_2CNH	C_5N		CH_3CHNH 2013					
HCl	H_2S	$HOCO^+$	H_2C_2O	*l*-HC_4H *							
KCl	HNC	H_2CO	H_2NCN	*l*-HC_4N							
NH	HNO	H_2CN	HNC_3	*c*-H_2C_3O							
NO	MgCN	H_2CS	SiH_4 *	H_2CCNH (?)							
NS	MgNC	H_3O^+	H_2COH^+	C_5N^-							
NaCl	N_2H^+	*c*-SiC_3	C_4H^-	HNCHCN 2013							
OH	N_2O	CH_3 *	HC(O)CN								
PN	NaCN	C_3N^-	HNCNH 2012								
SO	OCS	PH_3 ?	CH_3O 2012								
SO^+	SO_2	HCNO									
SiN	*c*-SiC_2	HOCN									
SiO	CO_2 *	HSCN									
SiS	NH_2	H_2O_2 2011									
CS	H_3^+ *	C_3H^+ (?) 2012									
HF	H_2D^+, HD_2^+										
HD	SiCN										
FeO ?	AlNC										
O_2	SiNC										
CF^+	HCP										
SiH ?	CCP										
PO	AlOH										
AlO	H_2O^+										
OH^+	H_2Cl^+										
CN^-	KCN										
SH^+ 2011	FeCN 2011										
SH 2012	HO_2 2012										
HCl^+ 2012	TiO_2 2013										
TiO 2012/13											

Figure 1.1: List of molecules detected in the ISM organized by number of atoms. This table is a screenshot from the University of Koln website (http://www.astro.uni-koeln.de/cdms/molecules).

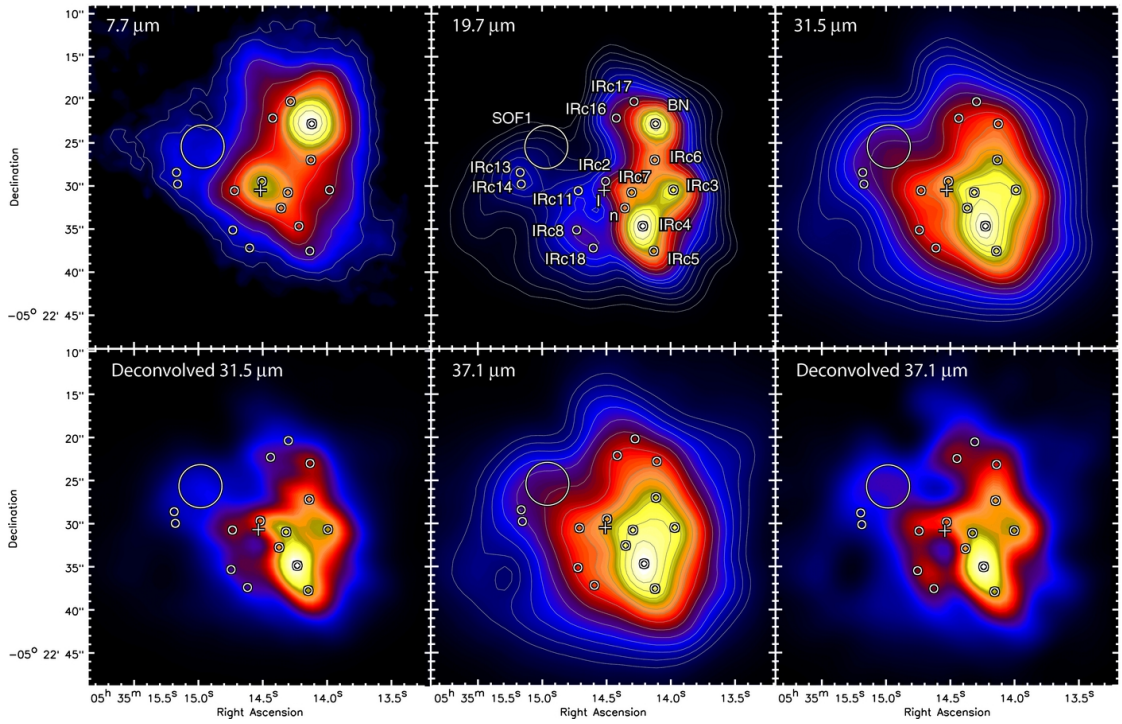

Figure 1.2: SOFIA mid-IR continuum maps of Orion KL taken with the FORCAST camera. The locations of known IR clumps, so called IRc sources, as well as near-IR source n and BN are indicated by white circles and are labeled in the upper middle panel. Radio source I is indicated by a white cross. This figure was taken from De Buizer et al. (2012).

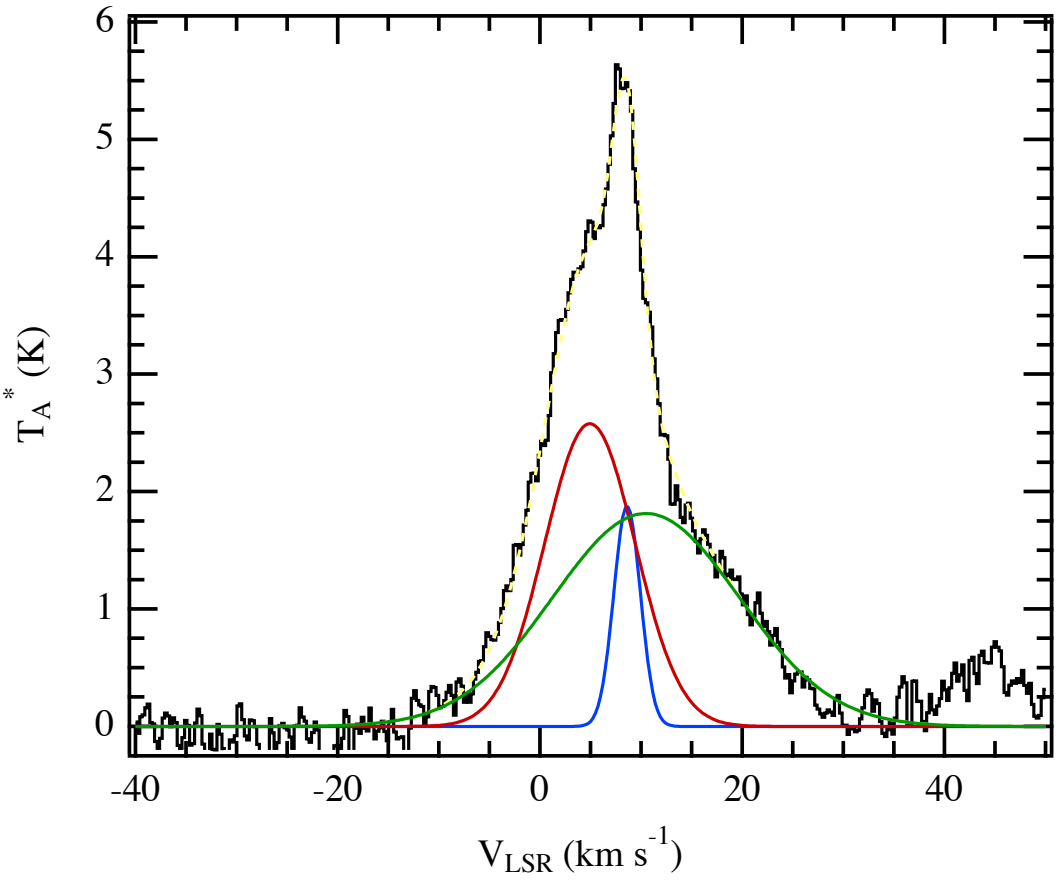

Figure 1.3: The HDO $3_{2,1}$ – $3_{1,2}$ transition observed in the Orion KL HIFI scan is plotted in black with Gaussian fits to different spatial/velocity components overlaid as different colors. The red, green, and blue Gaussians represent the hot core, plateau, and compact ridge spatial/velocity components, respectively. The yellow dashed line is the sum of the fits.

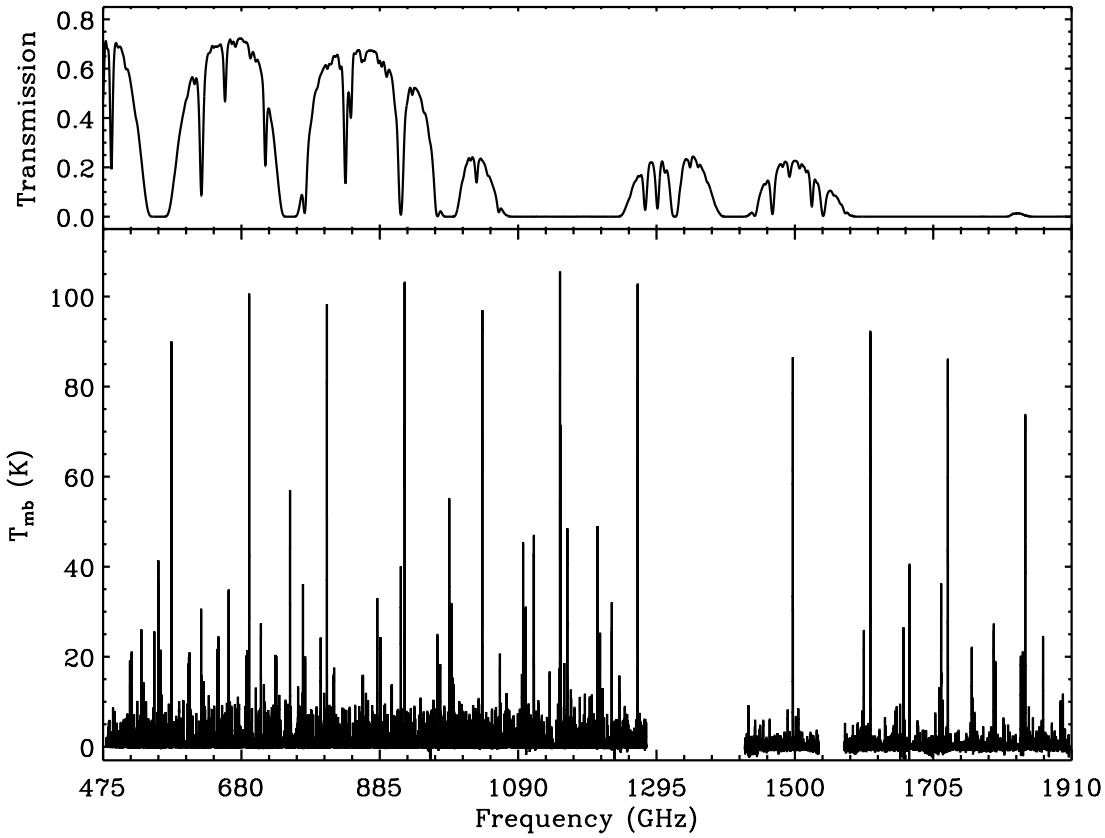

Figure 1.4: The full HIFI spectral scan of Orion KL is plotted in the bottom panel with the atmospheric transmission plotted in the top panel.

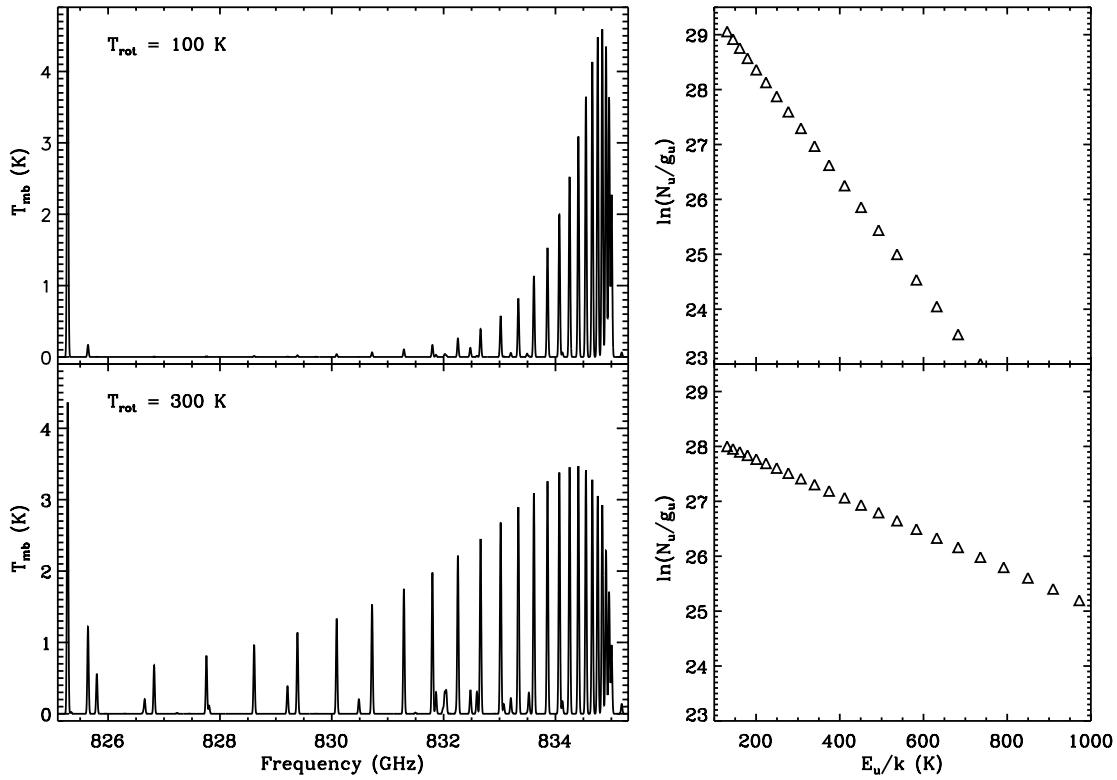

Figure 1.5: XCLASS model predictions for a methanol Q-branch are plotted in the left column. The upper and lower panels correspond to T_{rot} = 100 and 300 K, respectively. The upper and lower panels in the right column plot corresponding rotation diagrams.

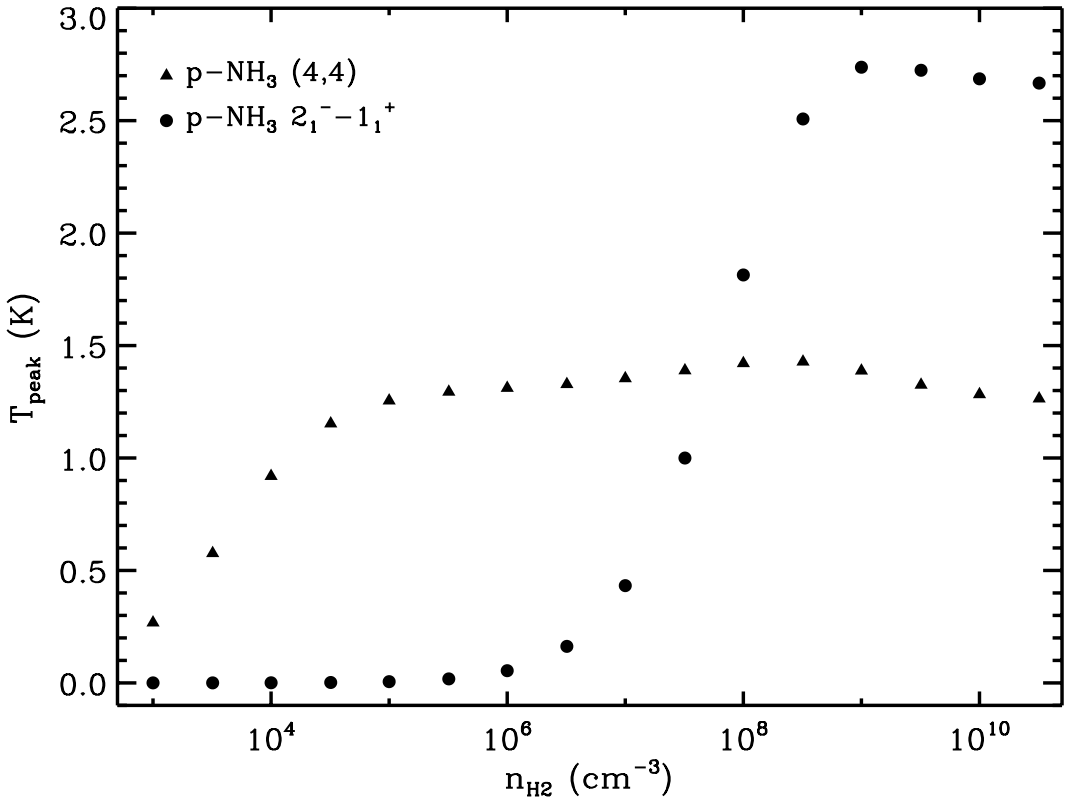

Figure 1.6: Peak line intensity vs. density as predicted by RADEX assuming T_{kin}=100 K, Δv=8.0 km/s, $N_{col}(NH_3)=10^{15}$ cm^{-3}, and T_{bg}=2.73 K. Predicted peak intensities from the p-NH_3 (4,4) inversion and $2_1^- – 1_1^+$ rotation transitions are plotted as triangles and circles, respectively. Peak intensities plotted here include a beam filling factor correction assuming a source size of 5″ and the *Herschel* telescope diameter of 3.5 m.

CHAPTER 2

The Terahertz Spectrum of Orion KL Seen at High Spectral Resolution

2.1 Introduction

The Kleinmann-Low nebula within the Orion molecular cloud (Orion KL) is the best studied massive star forming region in the Milky Way. This region is characterized by a high IR luminosity (Kleinmann & Low, 1967) and rich molecular line emission. As such, it has been the subject of numerous molecular line surveys in the millimeter and submillimeter that have characterized its mm/sub-mm wave spectrum (see e.g. Blake et al., 1987; Schilke et al., 1997; Comito et al., 2005; Tercero et al., 2010, and references therein). These surveys reveal the presence of a prodigious variety of molecular species in addition to several distinct spatial/velocity components (i.e. the hot core, compact ridge, plateau, and extended ridge; Blake et al., 1987; Persson et al., 2007). These observations provide insight into the complex chemical and physical processes that characterize how massive stars form and interact with their natal environment. Because Orion KL is the closest such massive star forming region ($\sim$414 pc; Menten et al. 2007), it is an ideal choice for further inquiry in understanding the chemistry and physics of the gas in close proximity to these stars.

Although the subject of much spectroscopic study in the mm /sub-mm ($\lambda \gtrsim 300\mu$m) during the past 30 years, high resolution observations at Terahertz (THz) frequencies of Orion KL have been unavailable from the ground due to atmospheric absorption. ISO provided the first comprehensive spectroscopic view of Orion KL at these wavelengths. Lerate et al. (2006) presented spectroscopic observations in the wavelength range 44 – 188 μm (1.6 – 6.8 THz) with a resolving power of $\lambda/\Delta\lambda \sim$

6800-9700 using the long wavelength spectrometer (LWS) on board ISO. These data showed a spectrum dominated by emission from H_2O, OH, and CO, but little or no emission from more complex species (such as methanol, methyl formate, dimethyl ether, etc.), which litter the spectrum at submillimeter wavelengths.

The HIFI instrument (de Graauw et al., 2010) on board the *Herschel* Space Observatory (Pilbratt et al., 2010) provides the first opportunity to characterize the THz spectrum with high spectral resolution and sensitivity. In this chapter, we present the first high resolution ($\lambda/\Delta\lambda \sim 10^6$) spectrum of Orion KL above 1.57 THz obtained using the HIFI instrument. These observations, taken as part of the guaranteed time key program *Herschel observations of EXtra-Ordinary Sources: The Orion and Sagittarius B2 Starforming Regions* (HEXOS), are able to probe the chemical inventory and kinematic structure of Orion KL at an unprecedented level. In this chapter, we characterize the high resolution THz spectrum. We further demonstrate and discuss why the observed line density is reduced when compared to lower frequencies.

2.2 Observations

The observations were carried out on March 22-23, 2010 using the wide band spectrometer (WBS) with a spectral resolution of 1.1 MHz (0.19 km s^{-1} at 1.75 THz) over a ∼2.4 GHz IF bandwidth. The data were taken in dual beam switch (DBS) mode using the fast chop setting pointed towards the Orion hot core at coordinates $\alpha_{J2000} = 5^h35^m14.5^s$ and $\delta_{J2000} = -5°22'30.9''$. The beam size at 1.75 THz is $12''$ and the DBS reference beams lie approximately $3'$ east and west. Both horizontal, H, and vertical, V, polarization data were obtained. However, we only present the H polarization here because the mixer is optimized for the H polarization. These data were reduced using HIPE (Ott, 2010) with pipeline version 2.4.

The observations presented here are full spectral scans of bands 6b and 7b, meaning they cover a frequency range of 1573.4 - 1702.8 GHz (176.2 - 190.7 μm) and 1788.4 - 1906.8 GHz (157.3 - 167.7 μm), respectively. These spectral scans consist of double-sideband (DSB) spectra with a redundancy of 4, which are deconvolved into single-sideband (SSB) spectra. This procedure is outlined in Bergin et al. (2010).

We applied the standard HIFI deconvolution using the *doDeconvolution* task within HIPE with no channel weighting or gain correction. Strong spurs and noisy DSB data sets were not included in the deconvolution and no fringing correction was applied. All data presented in this Letter are deconvolved SSB spectra.

After the deconvolution was performed, the data were exported to FITS format and all subsequent data reduction and analysis was performed using the IRAM GILDAS package. Main beam efficiencies for bands 6b and 7b were assumed to be 0.64 and 0.63, respectively. We estimate the typical RMS in both bands to be $T_A^* \approx 0.9$ K at the original spectral resolution.

2.3 Results

The SSB spectra for bands 6b and 7b are given in Fig. 2.1 smoothed to a velocity resolution of $\sim$4.5 km s^{-1} and corrected for a $V_{LSR} = 9$ km s^{-1} with the most prominent lines (peak $T_{MB} \gtrsim 7$ K) labelled. Polynomial baselines of order 2 are also subtracted from each spectrum. We find that these observations are dominated by strong lines of CO, H_2O, and OH as was reported by Lerate et al. (2006). With the higher spectral resolution of HIFI, we also detect additional strong lines of CH_3OH, H_2S, HCN, and HDO. Line identifications were made with the aid of the XCLASS program[1] which accesses both the CDMS (Müller et al., 2001, 2005, http://www.cdms.de) and JPL (Pickett et al., 1998, http://spec.jpl.nasa.gov) molecular databases. We list these transitions along with their integrated intensities in Table 2.1. Line intensities were measured using the CLASS data reduction and analysis software package. In instances where there were blends, Gaussian profiles were fit to the lines and the results from the fitted profiles are reported; otherwise the total intensity is measured directly using the BASE command. All line intensities were measured using spectra smoothed to a velocity resolution of $\sim$1 km s^{-1}. Uncertainties in the integrated intensities, σ_I, were computed using the relation σ_I(K km s^{-1}) $=\sqrt{N}(\delta v)RMS$ where δv is the resolution in velocity space, N is the number of channels over which the in-

[1]http://www.astro.uni-koeln.de/projects/schilke/XCLASS

tensity is measured, and RMS is the root mean square deviation in the vicinity of the line. In addition to the lines listed in Table 2.1, we also detect many additional weak transitions of CH_3OH, SO_2, H_2S, and H_2O along with their isotopologues. Examples of several weak lines detected in bands 6b and 7b are plotted in Fig. 2.2. Integrated line intensities for these weaker transitions along with peak intensities for all lines will be reported in a later study.

When comparing these spectra to other lower frequency HIFI bands, it is readily apparent that the line density is significantly diminished when compared to the lower frequency bands (see e.g. Bergin et al., 2010; Wang et al., 2010). We estimate that the total fraction of channels taken up by lines is $\sim$0.23 in the lower frequency bands compared to $\sim$0.07 in bands 6 and 7. We reached these estimates by counting the number of channels in emission in the frequency ranges 858.1 – 958.1 GHz (band 3b) and 1788.4 – 1898.5 GHz (band 7b). We adopt these line density estimates as being representative of the low and high frequency bands, respectively. Although not formally presented in this chapter, a full spectral scan of Orion KL taken in band 3b was also obtained as part of the HEXOS key program and used to estimate the line density here. These data were reduced in the same way as bands 6b/7b. Both bands were smoothed to a velocity resolution of $\sim$1 km s^{-1} and any channel that had a value $T_{MB} > 2.5$ K (after baseline subtraction) was flagged as being in emission in 7b. This threshold is approximately what we have estimated as 3$\times$ the RMS in T_{MB} in band 7b at a resolution of 1 km s^{-1} (RMS $\sim$ 0.8 K). Because the beam size, θ, decreases as a function of frequency ($\theta_{3b}\sim24''$), this value was scaled to an equivalent RMS in band 3b using the following relation,

$$T_{RMS_{3b}} = T_{RMS_{7b}} \left(\frac{\theta_{7b}}{\theta_{3b}}\right)^2, \tag{2.1}$$

which assumes that the source is significantly smaller than both beam sizes. Thus the reduced beam size should be more coupled to the smaller spatial components (e.g. the hot core). One might therefore naively expect the line density to increase at THz frequencies. The opposite trend, however, is observed.

2.4 Discussion

One of the primary reasons for the reduced line density in the high frequency bands is the fall off in emission from complex organic molecules known to exist in the interstellar medium (ISM), commonly referred to as "weeds", such as CH_3OCH_3, SO_2, C_2H_5CN, and, of course, CH_3OH. In Fig. 2.3 we present the number of emissive lines for select "weeds" as a function of frequency. To estimate these numbers we assumed LTE and predicted the emission for each species assuming T = 150K. We use the total column estimated for each molecule on the basis of Comito et al. (2005) and in addition assumed a velocity width of 5 km s^{-1}. If the predicted emission was above 0.1 K then we counted the line as potentially emissive in our 100 GHz bins. In this fashion we counted $N_{0.1K}$, which is shown in the figure. As can be seen, there is a general decrease in emission for all species but its particularly evident for CH_3OCH_3 and C_2H_5CN. CH_3OH has a small factor of 2 decrease in the number of lines and, at the zeroth level, this is seen in our data which has numerous weak methanol transitions scattered throughout the band.

Another possibility is that the dust emission from the hot core is optically thick in the high frequency bands; thus the dust would absorb all of the photons emitted from the molecules in the hot core. To explore this more closely we can examine the dust opacity expected within the hot core itself. Plume et al. (2012) used multiple transitions of $C^{18}O$ and spectrally isolated the hot core. They estimate an $N(C^{18}O) = 6.2\times10^{16}$ cm^{-2} which yields a total H_2 column of 3.1×10^{23} cm^{-2} assuming $n(C^{18}O)/n(H_2) = 2\times10^{-7}$. Using the relation given in Hildebrand (1983, Equation 10), we estimate a $\tau\sim0.1$ at 171 μm, putting it slightly lower than being optically thick.

It is clear that there are other emission components in this region as we see widespread emission from a variety of molecules in the high frequency bands. However, we still observe many molecules (CH_3OH, H_2O, HDO, and HCN) that have velocity components in their spectral profiles that are coincident to those expected from the hot core and other components (e.g. the outflows). If these emission com-

ponents do arise in the the hot core, it is likely that the molecular emission region must lie in front of any optically thick core. Given the presence of strong physical gradients in the density and temperature profiles (Wright et al., 1996; Blake et al., 1996) and the fact that the dust is marginally optically thick, this is not unrealistic.

A final contributor to the decrease in the line emission could be non-LTE excitation. At high frequencies there are a larger number of high excitation lines which could be more difficult to excite even at densities of 10^6 – 10^7 cm^{-3}. This needs to be more directly calculated using a molecule such as CH_3OH with collision rates that extend to temperatures greater than 200 – 300 K.

2.5 Summary

We have characterized the high frequency spectrum of Orion KL. We find that the spectrum is dominated by strong lines of CO, H_2O, HDO, OH, CH_3OH, H_2S, HCN, and NH_3. We also detect many weaker transitions of CH_3OH, H_2O, HDO, and SO_2. We find that the line density is diminished in the high frequency bands when compared to the lower frequency bands and provide a number of possible explanations as to why this may be.

Table 2.1: Strong Lines in Bands 6b and 7b

Molecule	Frequency (MHz)	Transition	$\int T_{MB} dv$ (K km s^{-1})	Notes
		Band 6b		
H_2O	1574232.073	$6_{4,3}$ – $7_{1,6}$	70.8 ± 6.7	
CH_3OH	1586012.991	$8_{5,1}$ – $7_{4,1}$	85.3 ± 3.0	3
	1586013.008	$8_{5,0}$ – $7_{4,0}$		3
H_2S	1592669.425	$7_{2,5}$ – $7_{1,6}$	69.5 ± 3.4	
HCN	1593341.504	18–17	138.4 ± 5.5	1
$H_2{}^{34}S$	1595984.323	$4_{2,3}$ – $3_{1,2}$	76.3 ± 5.1	
CH_3OH	1597947.024	$9_{6,0}$ – $8_{5,0}$	84.4 ± 4.1	3
	1597947.024	$9_{6,1}$ – $8_{5,1}$		3
H_2S	1599752.748	$4_{2,3}$ – $3_{1,2}$	258.0 ± 6.4	
H_2O	1602219.182	$4_{1,3}$ – $4_{0,4}$	959.0 ± 8.5	
$H_2{}^{34}S$	1605957.883	$6_{1,5}$ – $6_{0,6}$	116.0 ± 6.0	3
$H_2{}^{18}O$	1605962.460	$4_{1,3}$ – $4_{0,4}$		3
H_2S	1608602.794	$6_{2,5}$ – $6_{1,6}$	91.8 ± 4.2	
CO	1611793.518	14 – 13	4653.0 ± 12.0	2
$H_2{}^{18}O$	1633483.600	$2_{2,1}$ – $2_{1,2}$	192.0 ± 9.3	3
CH_3OH	1633493.496	$13_{4,0}$ – $12_{3,0}$		3
H_2S	1648712.816	$4_{2,2}$ – $3_{3,1}$	124.9 ± 4.9	1
^{13}CO	1650767.302	15 – 14	287.0 ± 8.0	3
CH_3OH	1650817.827	$21_{4,0}$ – $20_{3,0}$		3
$H_2{}^{18}O$	1655867.627	$2_{1,2}$ – $1_{0,1}$	75.6 ± 8.2	2
H_2O	1661007.637	$2_{2,1}$ – $2_{1,2}$	1008.0 ± 9.2	2
$H_2{}^{17}O$	1662464.387	$2_{1,2}$ – $1_{0,1}$	155.0 ± 7.4	2
H_2O	1669904.775	$2_{1,2}$ – $1_{0,1}$	2266.0 ± 10.4	2
HCN	1681615.473	19 – 18	136.0 ± 5.8	
CH_3OH	1682556.723	$10_{5,1}$ – $9_{4,1}$	76.6 ± 3.9	3

	1682556.856	$10_{5,0} - 9_{4,0}$		3
HDO	1684605.824	$6_{1,5} - 6_{0,6}$	71.9 ± 4.2	
		Band 7b		
H_2O	1794788.953	$6_{2,4} - 6_{1,5}$	969.0 ± 8.5	
H_2O	1797158.762	$7_{3,4} - 7_{2,5}$	648.0 ± 4.9	
NH_3	1808935.550	$3_{1,1} - 2_{1,0}$	158.0 ± 6.4	2
NH_3	1810377.792	$3_{2,1} - 2_{2,0}$	50.1 ± 8.3	2
$H_2{}^{18}O$	1815853.411	$5_{3,2} - 5_{2,3}$	91.0 ± 5.5	
CH_3OH	1817752.285	$7_{7,0} - 6_{6,0}$	35.7 ± 3.2	
OH	1834747.350	$^2\Pi_{1/2}3/2^- - 1/2^+$	627.0 ± 9.7	2, 4
OH	1837816.820	$^2\Pi_{1/2}3/2^+ - 1/2^-$	640.0 ± 11.5	2, 4
CO	1841345.506	16 – 15	3820.0 ± 10.4	2
H_2S	1846768.559	$6_{1,6} - 5_{0,5}$	237.0 ± 5.8	
H_2S	1852685.693	$5_{1,4} - 4_{2,3}$	181.0 ± 4.8	
H_2S	1862435.697	$5_{2,4} - 4_{1,3}$	84.7 ± 5.2	
H_2S	1865620.670	$3_{3,0} - 2_{2,1}$	173.6 ± 7.8	
H_2O	1867748.594	$5_{3,2} - 5_{2,3}$	864.0 ± 8.8	
H_2O	1880752.750	$6_{3,4} - 7_{0,7}$	135.0 ± 5.4	
H_2S	1882773.396	$8_{3,6} - 8_{2,7}$	37.9 ± 4.0	
H_2O	1893686.801	$3_{3,1} - 4_{0,4}$	265.0 ± 5.9	
$H_2{}^{18}O$	1894323.823	$3_{2,2} - 3_{1,3}$	161.0 ± 6.4	
H_2S	1900140.572	$7_{1,6} - 7_{0,7}$	83.80 ± 6.7	3
	1900177.906	$7_{2,6} - 7_{1,7}$		3

Notes: 1 – Line intensities were fit using Gaussian profiles because of a blend. 2 – Lines contained self absorption. 3 – Subsequent lines with this note were severely blended and could not be separated by line fitting. The same integrated intensity is reported for both entries. 4 – Other OH transitions contributed to the integrated intensity reported. The strongest transition is given.

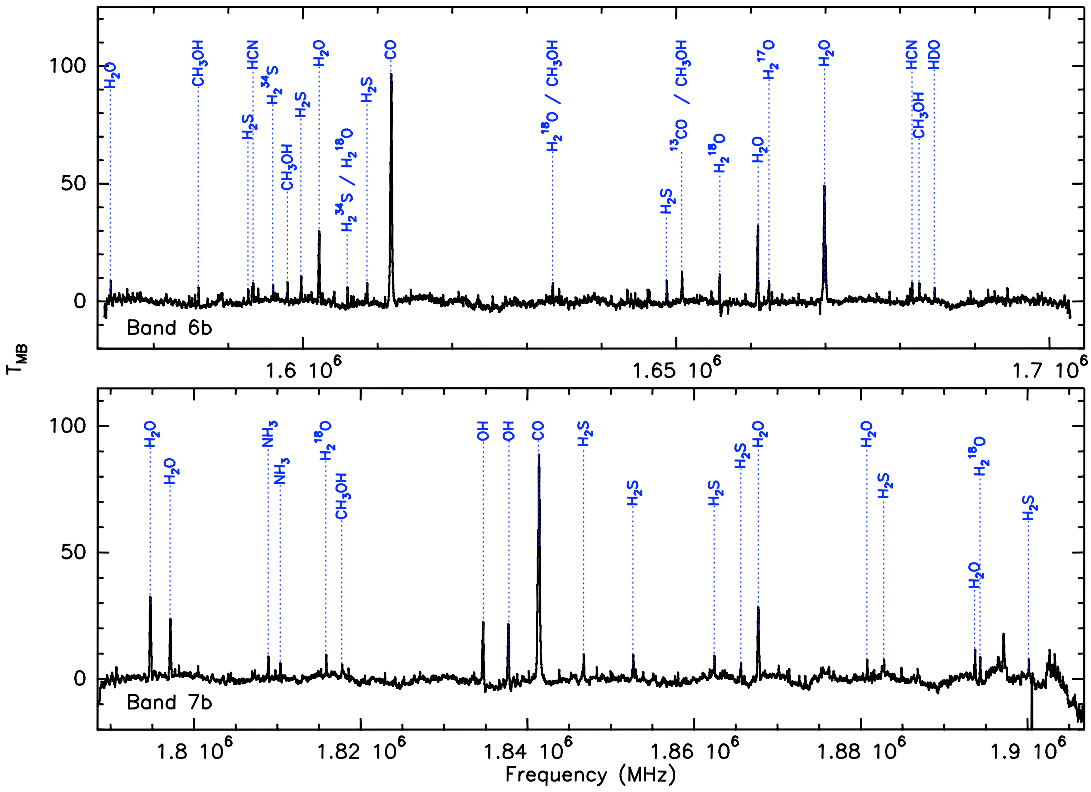

Figure 2.1: SSB spectrum of the Orion KL hot core in bands 6b (top panel) and 7b (bottom panel) smoothed to a velocity resolution of $\sim$4.5 km s^{-1}. The strongest lines ($T_{MB} \gtrsim 7$ K) are labelled.

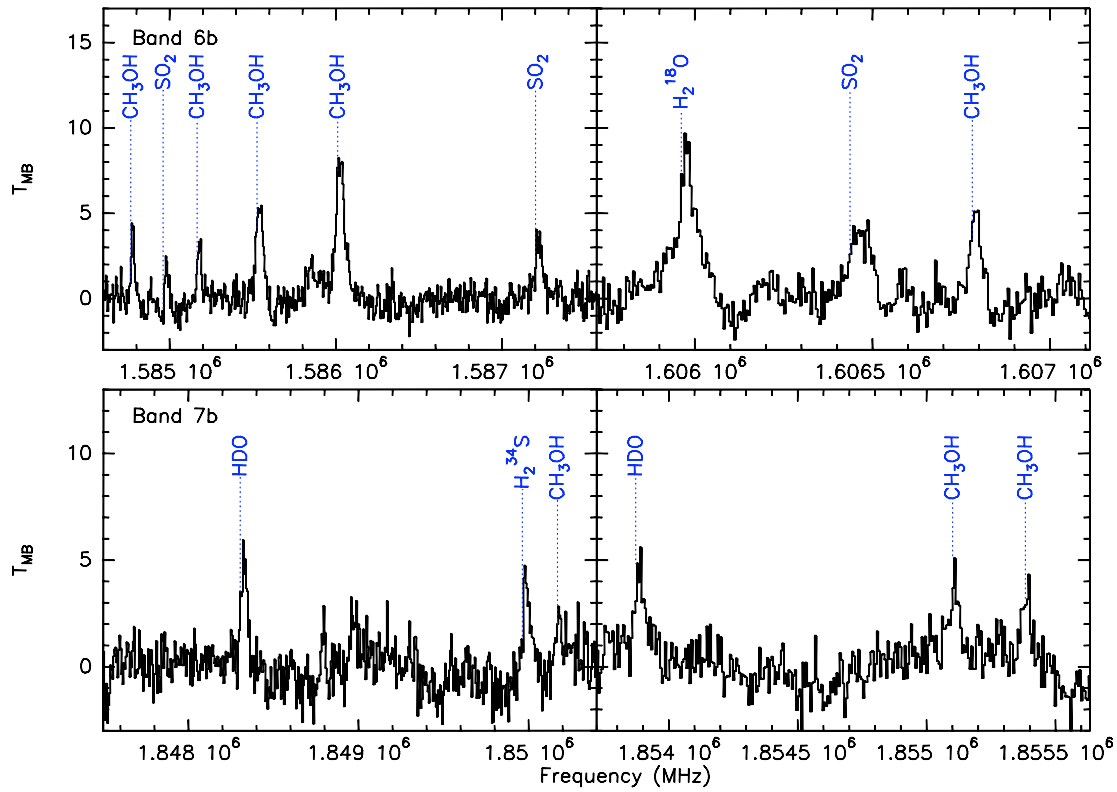

Figure 2.2: A small sample of weak lines in bands 6b (top panels) and 7b (bottom panels). All spectra are smoothed to a resolution of $\sim$1 km s^{-1}.

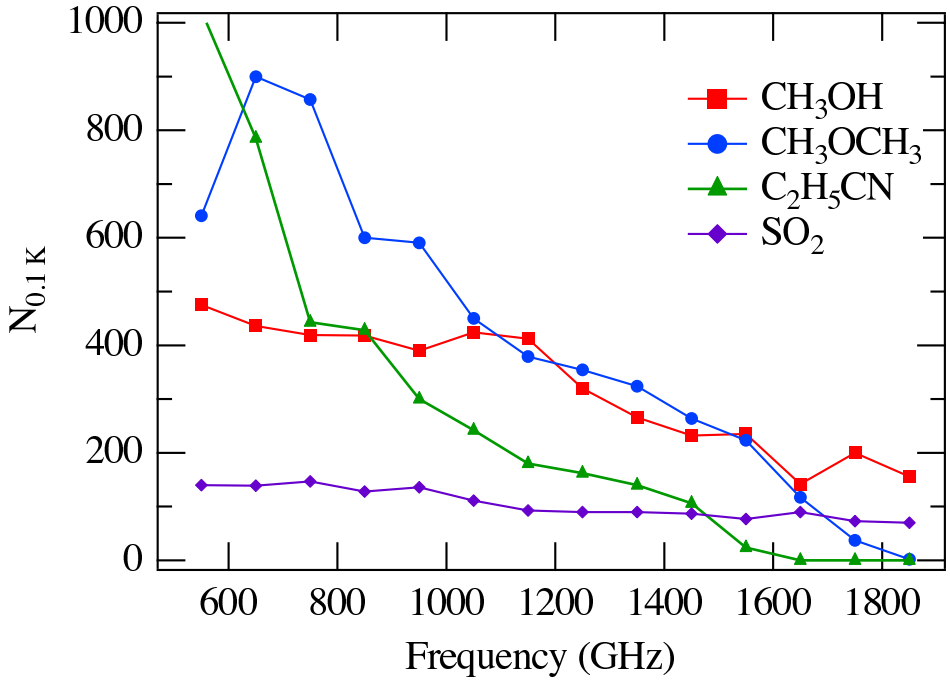

Figure 2.3: Predicted number of lines with peak emission > 0.1 K based on an LTE model in 100 GHz bins for select "weeds" as a function of frequency.

CHAPTER 3

The Full Band Model

3.1 Introduction

The origin of chemical complexity in the interstellar medium (ISM) is still not well understood. Approximately 175 molecules, not counting isotopologues, have been detected in the ISM (Menten & Wyrowski, 2011). The majority of complex molecules are thought to originate on grain surfaces although it is possible that gas phase processes play a significant but, as of yet, unknown role (Herbst & van Dishoeck, 2009). One of the best ways to probe the chemistry that is occurring within the ISM is via unbiased spectral line surveys in the mm and sub-mm, where molecular line emission is strong. Massive star forming regions are among the most prolific emitters of complex organic molecules, the presence of which are produced primarily by energetic protostars that heat the surrounding material liberating molecules from dust grains and driving chemical reactions that cannot occur at lower temperatures (see e.g. Herbst & van Dishoeck, 2009; Garrod & Herbst, 2006; Garrod et al., 2008, and references therein). Unbiased spectral line surveys offer a unique avenue to explore the full chemical inventory and active molecular pathways in the dense ISM. Molecular rotational emissions are, for the most part, concentrated at mm and sub-mm wavelengths but the interference of atmospheric absorption has left broad wavelength regimes unexplored which has hampered our ability to obtain a complete unbiased viewpoint of the molecular content of these regions.

In this study, we present a comprehensive full band analysis of the HIFI 1.2 THz wide spectral survey toward the Orion Kleinmann-Low nebula (Orion KL), one of the archetypal massive star forming regions in our Galaxy. Specifically, we model

the emission in order to obtain reliable molecular abundances. Because of its close distance (414 pc; Menten et al., 2007) and high luminosity (10^5 $L_\odot$; Wynn-Williams et al., 1984), Orion KL has been exhaustively studied not only in the (sub-)mm but throughout the electromagnetic spectrum (Genzel & Stutzki, 1989; O'dell, 2001). As such, numerous single dish spectral line surveys have been carried out toward Orion KL in the mm (Johansson et al., 1984; Sutton et al., 1985; Blake et al., 1987; Turner, 1989; Greaves & White, 1991; Ziurys & McGonagle, 1993; Lee et al., 2001; Lee & Cho, 2002; Goddi et al., 2009b; Tercero et al., 2010, 2011) and sub-mm (Jewell et al., 1989; Schilke et al., 1997, 2001; White et al., 2003; Comito et al., 2005; Olofsson et al., 2007; Persson et al., 2007). These studies show that Orion KL is one of the most chemically rich sources is the Milky Way and that the molecular line emission originates from several spatial/velocity components representing a diverse set of environments within Orion KL. Although not spatially resolved by single dish observations, these components can be differentiated using high resolution spectroscopy because they have significantly different line widths and central velocities.

The observations presented in this study were obtained as part of the *Herschel Observations of EXtra Ordinary Sources* (HEXOS) guaranteed time key program and span a frequency range from 480 to 1907 GHz, providing extraordinary frequency coverage in the sub-mm and far-IR. This dataset alone provides a factor of 2.5 larger frequency coverage than all previous high resolution (sub-)mm spectral surveys combined. This dataset thus allows us to robustly constrain the emission of both complex organics, using hundreds to thousands of lines, and lighter species with more widely spaced transitions over an unprecedented range in excitation energy. Molecular abundances derived in this study thus span the entire range of ISM chemistry, from simple molecules to complex organics. The HIFI spectrum at $\nu \gtrsim 1$ THz, furthermore, represents the first high spectral resolution observations of Orion KL in this spectral region, which are not accessible from the ground, giving access to transitions of light hydrides such as H_2O and H_2S. We emphasize that these data were obtained with the same instrument and near uniform efficiency meaning that relative line intensities across the entire band are tremendously reliable.

This chapter is organized in the following way. In Sec. 3.2, we present the observations and outline our data reduction procedure. Our modeling methodology is described in Sec. 3.3. Our results are presented in Sec. 3.4. This includes line statistics and reduced χ^2 calculations for our models (Sec. 3.4.1), our derived molecular abundances (Sec. 3.4.2), and unidentified (U) line statistics (Sec. 3.4.3). Descriptions of individual molecular fits are given in Sec. 3.5. We give a discussion of our results in Sec. 3.6. Finally, our conclusions are summarized in Sec. 3.7.

3.2 Observations and Data Reduction

The data presented in this work were obtained using the HIFI instrument (de Graauw et al., 2010) on board the *Herschel* Space Observatory (Pilbratt et al., 2010). The full HIFI spectral survey toward Orion KL is composed of 18 observations, each of which is an independent spectral scan obtained using the wide band spectrometer (WBS) covering the entire frequency range of the band in which the observation was taken. All available HIFI bands (1a – 7b) are represented in this dataset meaning total frequency coverage between 480 and 1900 GHz with two gaps at 1280 – 1430 GHz and 1540 – 1570 GHz. The WBS has a spectral resolution of 1.1 MHz (corresponding to 0.2 – 0.7 km/s across the HIFI scan) and provides separate observations for horizontal (H) and vertical (V) polarizations. The scans were taken such that any given frequency was covered by six subsequent LO settings for bands 1 – 5, or 4 LO settings for bands 6 – 7. Additional details concerning HIFI spectral surveys can be found in Bergin et al. (2010).

The telescope was pointed toward $\alpha_{J2000} = 5^h35^m14.3^s$, $\delta_{J2000} = -5°22'33.7''$ in bands 1 – 5, where the beam size, θ_b, was large enough ($\sim$ 44 – 17″) to include emission from all spatial/velocity components. For bands 6 and 7, however, the beam size was small enough ($\sim$ 15 – 11″) that individual pointings toward the hot core ($\alpha_{J2000} = 5^h35^m14.5^s$, $\delta_{J2000} = -5°22'30.9''$) and compact ridge ($\alpha_{J2000} = 5^h35^m14.1^s$, $\delta_{J2000} = -5°22'36.5''$) were obtained. We assume the nominal *Herschel* pointing uncertainty of 2″ (Pilbratt et al., 2010). All data were taken using dual beam switch (DBS) mode such that the reference beam was chopped 3′ east or west of the target

position.

The method we used to reduce the data begins with standard HIPE (Ott, 2010) pipeline processing (version 5.0, CIB 1648) to produce so called "Level 2" double sideband (DSB) spectra at individual LO settings. Spurious spectral features ("spurs") and baselines were also removed from each scan before they were deconvolved into a single sideband (SSB) spectrum. The finished product of this procedure is a deconvolved, H/V polarization averaged, SSB spectrum for each band with the continuum emission removed. We note that even though the continuum emission was removed from the DSB data prior to deconvolution, baseline offsets as large as $\pm$ 0.1 K in the SSB spectra are present. Table 3.1 lists the date, observation ID (OBSID), frequency coverage, integration time, and T_A^* RMS for each observation. We note that the RMS level can vary significantly across a given band. Values reported in Table 3.1 are, therefore, merely the most representative RMS estimates.

All scans were corrected for aperture efficiency using Eqs. 1 and 2 from Roelfsema et al. (2012). In bands 1 – 5, we applied the aperture efficiency, which is linked to a point source, because the *Herschel* beam is large relative to the size of the hot core and compact ridge ($\sim$10$''$). For bands 6 and 7, on the other hand, we applied the main beam efficiency because the beam size is comparable to the size of the hot core and compact ridge and the main beam efficiency is coupled to an extended source. We, however, refer to all line intensities as main beam temperatures, T_{mb}, in this work for the sake of simplicity. Fig. 3.1 plots the entire HIFI spectral survey toward Orion KL. From the figure, the high sub-mm line density, characteristic of Orion KL, is readily apparent. Figs 3.2 – 3.6 plot each band individually so that more details of the spectrum can be seen. In particular, these figures show a marked decrease in the observed line density as a function of frequency, which, as described in Chapter 2, is mainly due to a drop off in the number of emissive transitions from complex organics (Crockett et al., 2010).

In addition to these data products, we also provide SSB spectra with the continuum present. These data were produced by deconvolving DSB spectra after spur removal but before baseline subtraction. The resulting SSB spectra thus con-

tained the continuum but had higher noise levels due to baseline offsets between scans. We next fit a second order polynomial to the continuum in each band. We then added these polynomial fits to the baseline subtracted SSB scans, thus yielding a spectrum which includes the continuum but does not contain the extra noise brought about by baseline offsets. All data products are available online at http://herschel.esac.esa.int/UserProvidedDataProducts.shtml in ascii, CLASS, and HIPE readable FITS formats. Model fits of individual molecular species (Sec. 3.3) are also available here.

3.3 Modeling Methodology

We modeled the emission of each detected molecule, including isotopologues, one at a time. Summing all of the individual fits, thus, yielded the total molecular emission, i.e. the "full band model". This procedure was carried out by multiple individuals simultaneously, each person modeling several molecules, allowing for blended lines to be more quickly identified. A list of the individuals who participated in this analysis, along with the molecules they modeled, is given in Appendix A. The molecular emission was fit using the XCLASS[1] program. We note that two species, CO and H_2O (main isotopologues only), were too optically thick to model with either program. Consequently, we fit simple Gaussian profiles to these species and include those fits in the full band model.

In order to constrain the molecular emission at mm wavelengths, we include a spectral survey obtained with the IRAM 30 m telescope in our analysis. This dataset is described in Tercero et al. (2010) and covers frequency ranges 200 – 280 GHz, 130 – 180 GHz, and 80 – 116 GHz, corresponding to spectral windows at 1, 2, and 3 mm, respectively. These observations were pointed toward IRc2 at $\alpha_{2000.0} = 5^h45^m14.5^s$ and $\delta_{2000} = -5°22'30.0''$. Because the beam size varies between $29''$ and $9''$, these observations are most strongly coupled to the hot core especially at high frequencies where the beam size is smallest. As a result, our models often over predicted emission

[1]http://www.astro.uni-koeln.de/projects/schilke/XCLASS

toward the compact ridge relative to the data in the 1 mm band.

By combining the HIFI and IRAM surveys, we are essentially modeling the entire spectrum of a given molecule including low energy states, i.e. ground state transitions or close to it, up to energy levels where emission is no longer detected. This is true even for lighter molecules, with widely spaced transitions. Because of the extremely large number of observed lines in the HIFI survey ($\sim 1.7 \times 10^4$; see Sec. 3.4.1), we do not compile line lists for detected molecules. Instead, we provide individual molecular fits to the data which are publicly available online at http://herschel.esac.esa.int/UserProvidedDataProducts.shtml, along with the reduced data (see Sec. 3.2). The model spectra are available in ascii, CLASS, and HIPE readable FITS formats.

3.3.1 Description of Orion KL Components

Molecular line emission toward Orion KL originates from several distinct spatial/velocity components. These components are typically labeled as the "hot core", "compact ridge", "plateau", and "extended ridge" (Blake et al., 1987). Using HIFI's high spectral resolution, we are able to differentiate these components even though they all lie within the *Herschel* beam because they have line profiles with significantly different velocities relative to the Local Standard of Rest, v_{lsr}, and full widths at half maximum, Δv (Blake et al., 1987). We briefly describe each component in the following.

The hot core, so named because it is a hot and dense ($\gtrsim 10^7$ cm^{-3}) clump of gas which may be harboring one or more massive protostars, is characterized by lines with v_{lsr} $\sim$4 – 6 km/s and $\Delta v \approx$ 7–12 km/s. This region, originally detected via inversion lines of NH_3 (Ho et al., 1979), is in general rich in nitrogen bearing molecules. Interferometric observations of CH_3CN and NH_3 reveal an intricate, clumpy structure on size scales $\lesssim$ 1–2$''$ and a non-uniform temperature distribution with measured rotation temperatures varying between $\sim$150 – 600 K (Wang et al., 2010; Goddi et al., 2011). The ultimate heating source, however, remains unclear. In fact, both Zapata et al. (2011) and Goddi et al. (2011) conclude that the Orion KL hot core is most likely externally heated, though they disagree on the source, meaning the title

"hot core" may be inaccurate.

The compact ridge is a group of dense clumps of quiescent gas, which are likely externally heated (Wang et al., 2011; Favre et al., 2011), located approximately 12″ south-west of the hot core. This region is characterized by high densities ($\sim 10^6$ cm^{-3}) and temperatures of $\sim$ 80–150 K (Blake et al., 1987). Line profiles emitted from the compact ridge have narrow line widths, Δv $\approx$ 3 – 6 km/s and line centers at $v_{lsr} \approx$ 7 – 9 km/s. Compared to the hot core, the compact ridge is much richer in complex oxygen bearing organics (Blake et al., 1987; Friedel & Snyder, 2008; Beuther et al., 2005).

The plateau includes at least two outflows often referred to as the low velocity flow (LVF) and high velocity flow (HVF). The LVF is oriented along a NE – SW axis (Genzel & Stutzki, 1989; Blake et al., 1996; Stolovy et al., 1998; Greenhill et al., 1998; Nissen et al., 2007; Plambeck et al., 2009; Goddi et al., 2009a), and is thought to be driven by radio source I, an embedded massive protostar with no sub-mm or IR counterpart (Menten & Reid, 1995; Plambeck et al., 2009). The HVF, on the other hand, is oriented along a NW–SE axis, perpendicular to the LVF (Allen & Burton, 1993; Chernin & Wright, 1996; Schultz et al., 1999; O'dell, 2001; Doi et al., 2002; Nissen et al., 2012). There have been several suggestions as to the ultimate power source behind the HVF. Beuther & Nissen (2008), for example, suggest that the sub-mm source SMA1 may be driving this outflow. Plambeck et al. (2009), on the other hand, argue that the HVF is merely a continuation of the LVF. Yet another possibility is that the HVF is powered by the decay of a multi star system possibly involving radio source I, IR source n, and BN (Rodríguez et al., 2005; Gómez et al., 2005, 2008; Zapata et al., 2009; Bally et al., 2011; Nissen et al., 2012). The plateau is characterized by wide line widths (Δv $\gtrsim$ 20 km/s) at $v_{lsr} \sim$ 7 – 8 km/s and rotation temperatures $\sim$ 95 – 150 K (Blake et al., 1987).

The extended ridge represents the most widespread, quiescent gas toward Orion KL. Measured rotation temperatures are typically $\lesssim$ 60 K and the line profiles are narrow, Δv $\approx$ 2 – 4 km/s, with line centers at $v_{lsr} \approx$ 8 – 10 km/s (Blake et al., 1987).

3.3.2 Hot Core South

During the course of modeling the data, we noticed that several molecules contained a spectral component with $\Delta v \sim 5 - 10$ km/s and $v_{lsr} \sim 6.5 - 8$ km/s, in between line parameters typically associated with the hot core and compact ridge. The presence of this type of component was noted previously by Neill et al. (2013) who present a detailed analysis of water and HDO emission in the Orion KL HIFI survey. Specifically, $HD^{18}O$ lines detected in the HIFI scan have an average $v_{lsr} = 6.7$ km/s and $\Delta v = 5.4$ km/s, consistent with this "in between" component. Using HDO interferometric maps obtained from the publicly available ALMA band 6 line survey of Orion KL, taken as part of ALMA's science verification (SV) phase, the Neill study showed that this emission likely originates from a heavily deuterated clump approximately $1''$ south of the hot core sub-mm continuum peak.

We employ the ALMA-SV dataset here to map, in addition to HDO, $^{13}CH_3OH$, another species which contains an "in between" component in the HIFI scan ($v_{lsr} = 7.5$ km/s, $\Delta v = 6.5$ km/s), $^{13}CH_3CN$, a hot core tracer with typical line parameters for that region ($v_{lsr} \approx 5.5$ km/s, dv ≈ 8 km/s), and CH_3OCHO, a prominent compact ridge tracer also with typical line parameters ($v_{lsr} \approx 8$ km/s, $\Delta v \approx 3$ km/s). Fig. 3.7 contains four panels each plotting an integrated intensity map (color scale) of a transition from one of these molecules. The continuum at 230.9 GHz, provided on the ALMA-SV website, is overlaid as white contours in each panel. White crosses indicate the locations of IRc7 and methyl formate peaks MF1, MF4, and MF5 in the notation of Favre et al. (2011). The sub-mm clump associated with the hot core is also labeled. We used the same data product presented in Neill et al. (2013) to make Fig. 3.7. Details concerning how these data were processed can be found in that work.

From Fig. 3.7, we see that $^{13}CH_3CN$ traces the hot core continuum closely while HDO, as first pointed out by Neill et al. (2013), traces a clump $\sim 1''$ south of the continuum peak. The $^{13}CH_3OH$ map in Fig. 3.7 is integrated in the velocity range $3 - 5$ km/s to avoid emission from the compact ridge, which methanol also traces. As such, Fig. 3.7 shows that $^{13}CH_3OH$ emission from the "in between" component does not originate from the compact ridge as traced by methyl formate. Rather, this

emission is strongest just south of where $^{13}CH_3CN$ peaks. Because the difference is more subtle than with HDO, Fig. 3.8 plots the $^{13}CH_3OH/^{13}CH_3CN$ integrated intensity ratio, which shows a clear gradient in $^{13}CH_3OH$ emission relative to $^{13}CH_3CN$ from north to south. Given that HDO and $^{13}CH_3OH$ both trace regions south of the $^{13}CH_3CN$ peak, we assume other molecules displaying emission from this "in between" component originate from a similar region. We thus label this component "hot core south" or hot core (s).

3.3.3 XCLASS Modeling

All molecular species were modeled using XCLASS. This program uses both the CDMS (Müller et al., 2001, 2005, http://www.cdms.de) and JPL (Pickett et al., 1998, http://spec.jpl.nasa.gov) databases to produce model spectra assuming local thermodynamic equilibrium (LTE). Input parameters are the telescope diameter, D_{tel}, source size, θ_s, rotation temperature, T_{rot}, total column density, N_{tot}, line velocity relative to the Local Standard of Rest, v_{lsr}, and line full width at half maximum, Δv. In order to account for dust extinction, the user also specifies the total H_2 column density, N_{H_2}, dust opacity at 1.3 mm, $\kappa_{1.3}$, and dust extinction power law, β. Additional information regarding XCLASS, e.g. specific equations used in the code, can be found in Comito et al. (2005) and Zernickel et al. (2012).

We assume that all molecules emitting from the same spatial/velocity component have the same source size, which is a simplifying assumption. The aim of this study, however, is not a detailed analysis of any single molecule. It is a holistic analysis of the entire spectrum. This is therefore a reasonable approximation and is in line with previous spectral survey papers of Orion KL (see e.g. Tercero et al., 2010, 2011). Adopted source sizes for each spatial/velocity component are given in Table 3.2. We estimate θ_s for the hot core and compact ridge using interferometric observations from Beuther & Nissen (2008) and Favre et al. (2011), respectively. The plateau source size was obtained from *Herschel*/HIFI water maps taken as part of the HEXOS program (Melnick et al. 2013, in preparation). Finally, we assume a source size of $180''$ for the extended ridge to reflect the fact that the extended ridge completely fills the

Herschel beam at all frequencies. For several molecules, we were forced to use θ_s values that differed from those given in Table 3.2. These deviations are explained in the descriptions of individual molecular fits presented in Sec. 3.5.

N_{H_2} estimates for each spatial/velocity component are also given in Table 3.2. We obtained these values from Plume et al. (2012), who use $C^{18}O$ lines within the Orion KL HIFI scan to derive total $C^{18}O$ column densities which they convert to N_{H_2} estimates by assuming a CO abundance of 1.0×10^{-4} and ^{16}O / $^{18}O = 500$. We modified the H_2 column densities for the compact ridge and plateau because the Plume study assumed source sizes for these components that are different than what we adopt here. Consequently, we recalculated the $C^{18}O$ upper state columns assuming the source sizes used in this study and applied the same correction factors reported by Plume et al. (2012).

For the dust extinction power law (Eq. 1.10), we assume $\kappa_{1.3} = 0.42$ cm^2 g^{-1} and $\beta = 2$, corresponding to the midpoint between MRN and MRN with thin ice mantles (Ossenkopf & Henning, 1994). During the course of modeling the data, we found that the N_{H_2} values derived from the $C^{18}O$ lines tended to underestimate the extinction necessary to reproduce the emission in the highest frequency bands where the dust optical depth is highest. In other words, molecules fit well at frequencies below ~ 1 THz always tended to be over predicted at higher frequencies. As a result, we used a higher N_{H_2} estimate to compute the dust optical depth in the XCLASS models. We adopted a value of $N_{H_2} = 2.5 \times 10^{24}$ cm^{-2} for the hot core, compact ridge, and plateau, which reproduces the observed emission well. This value is more commensurate with N_{H_2} measurements based on dust emission toward Orion KL (Favre et al., 2011), and corresponds to a range in τ_d of $\sim 0.2 - 2.4$ at HIFI frequencies. At the low end of HIFI's frequency coverage, τ_d thus reduces the observed line intensities by approximately 20%. At high frequencies (bands 6 and 7), the dust optical depth is more significant, reducing the observed line intensities by a factor of $\sim 5 - 10$. Because the extended ridge represents extended, lower density gas, we retained the N_{H_2} value given in Table 3.2 when computing the dust optical depth for this spatial/velocity component.

We fit an XCLASS model to the emission of each molecule by first selecting a sample of transitions with varying line strengths that covered the entire range in excitation energy over which emission was detected. For simple species, with relatively few lines, this was straightforward. For more complex organics, however, we had many lines, thousands in some cases, from which to choose. Care was taken to select lines that were not blended with any other species. This was done by overlaying the full band model and observed spectrum while we selected transitions on which to base our fit. Because the full band model is the sum of all molecular fits, it evolved as the individual molecular fits changed. Once a sample of lines was selected, each transition was plotted simultaneously in a different panel with the panels arranged so that the upper state energy increased from the lower left panel to the upper right. The emission was then fit by varying the input parameters (i.e. T_{rot}, N_{tot}, v_{lsr}, and Δv) until good agreement was achieved between the data and model at all excitation energies. The goodness of fit was assessed by eye, we then computed a reduced χ^2 metric, described in Appendix B, for each model, and the fits were revised iteratively.

When we observed more than one isotopologue for a given molecule, effort was made to produce models which used consistent values for T_{rot}, Δv, and v_{lsr} for all isotopic species. We, however, sometimes made small adjustments to these parameters to get the optimum fit. The major difference between the models is thus the column density, the ratio of which should be equal to the isotopic abundance ratio. Among rarer isotopologues, isotopic ratios inferred from our models are commensurate with those derived previously toward Orion KL (Tercero et al., 2010; Blake et al., 1987) indicating optically thin emission. Our models, however, also indicate that many of the most abundant isotopologues are optically thick, meaning our models likely underestimate N_{tot}. Furthermore, we often had to fit very optically thick isotopologues with higher rotation temperatures than their more optically thin counterparts in order to reproduce the observed line intensities over all energies. Emission from these species therefore is too optically thick from which to derive reliable T_{rot} and N_{tot} values using XCLASS. As a result, these models serve mainly as templates for the observed data. Molecular fits for species that fall into this category are marked

with an "X" in Table 3.3. This table is broken down by spatial/velocity component because a particular species may not be optically thick in all of its components.

While modeling the hot core and plateau with XCLASS, we found that, for some molecules, a single temperature fit failed to reproduce the observed emission, which suggests the presence of temperature gradients in these components. This was most apparent when trying to simultaneously fit both the IRAM and HIFI data. Because the IRAM data, in general, probed lower energy transitions compared to HIFI, the IRAM spectra sometimes required additional cooler sub-components in order for a single model to fit both datasets well. We, thus, included additional sub-components when necessary to simulate temperature gradients. For the hot core, the sub-component responsible for most of the emission in the HIFI scan always had a source size of $10''$. Hotter or cooler sub-components were then added such that the source size increased or decreased by successive factors of two. Temperature gradients were organized such that T_{rot} increased as θ_s decreased (i.e. the more compact emission is hotter), corresponding to an internally heated clump. For the plateau, we kept a $30''$ source size for all sub-components to simulate the fact that the plateau fills most of the *Herschel* beam at HIFI frequencies.

Figs. 3.9, 3.10, and 3.11 plot examples of our molecular fits for $H^{13}CN$, a polyatomic linear rotor, $^{34}SO_2$, an asymmetric rotor, and CH_3OCHO, a complex organic, respectively. These figures illustrate the diversity in observed line profiles not only between molecules which trace different spatial/velocity components but also from the same species at different excitation energies. The latter arises because the hot core, compact ridge, plateau, and extended ridge are emissive over different ranges in excitation energy. XCLASS model parameters for molecular fits from which we obtain robust T_{rot} and N_{tot} information are given in Table 3.4. We do not include models marked in Table 3.3 because they do not provide any physical information.

3.3.4 Vibrationally Excited Emission

We detect vibrationally excited emission from several molecules within the HIFI scan. These species are HCN (ν_2=1 and ν_2=2), $H^{13}CN$ (ν_2=1), HNC (ν_2=1), HC_3N (ν_7=1),

CH_3CN (ν_8=1), NH_3 (ν_2=1), SO_2 (ν_2=1), and H_2O (ν_2=1). As with different isotopologues, we attempted to fit self consistent models between vibrationally excited and $\nu = 0$ models, i.e. the same T_{rot} and N_{tot}, though adjustments to T_{rot} in the vibrationally excited models were sometimes employed to improve the fit. For most of the molecules with detected vibrationally excited modes, total column densities inferred from ground and vibrationally excited states agree to within a factor of two. We, however, required significantly higher total column densities to fit the vibrationally excited HCN (hot core) and CH_3CN (plateau only) emission. The ν_2=1 $H^{13}CN$ and ν_2=2 HCN models suggest total HCN column densities toward the hot core that are higher than that predicted by the $HC^{15}N$ ground vibrational state model by factors of approximately 20 and 6, respectively, once N_{tot} values are scaled according to appropriate isotopic ratios (see Sec. 3.4.2). We note here that emission from HCN, ν_2=1 and $H^{13}CN$, ν=0 is likely optically thick. Similarly, the CH_3CN, ν_8=1 plateau model requires a total column density that is a factor of ~ 3.5 times higher than that predicted by $^{13}CH_3CN$ and $CH_3{}^{13}CN$ isotopologues once N_{tot} is properly scaled. The need for higher total column densities in the HCN and CH_3CN vibrationally excited models implies that these energetic modes are more heavily populated than predicted by our $\nu = 0$ models and is possibly the result of pumping from mid/far-IR photons.

3.4 Results

3.4.1 The Full Band Model and Line Statistics

In total, we detect 76 isotopologues from 36 molecules. Emission from each species has been modeled simultaneously over the entire HIFI 1.2 THz wide bandwidth and at mm wavelengths. We, in general, find excellent agreement between the data and models. Summing the molecular fits, we obtain the full band model for Orion KL. Fig. 3.12 plots three sections from the HIFI spectrum with the full band model overlaid as a solid red line. Individual models for the five most emissive molecules in these regions are also overlaid as different colors. Fig. 3.12 focuses on frequencies less than 1280 GHz and intensity scales ≥ 5 K. The plot thus gives a flavor for how

well the full band model reproduces strong lines in bands 1a – 5b. Fig. 3.13, on the other hand, plots three regions at the low frequency end of the survey at T_{mb} levels less than 0.8 K, highlighting weak emission fit by the full band model largely from complex organics. A similar sample of three spectral regions in bands 6 and 7, the highest frequency bands in the HIFI survey, is plotted in Fig. 3.14. We see from this plot that the high frequency bands are dominated by emission from lighter species as well as CH_3OH.

In order to quantify how well each molecular fit reproduced the data, we computed a reduced chi squared, χ^2_{red}, statistic for each model. The χ^2_{red} calculations are described in Appendix B and are reported in Table 3.5 in ascending order along with the database from which we obtained each spectroscopic catalog. Our models approximate temperature in a simple way (i.e. adding multiple sub-components). Our models, furthermore, make a number of simplifying assumptions. First, we assume LTE level populations. Second, XCLASS does not include radiative excitation effects which are likely important for some molecules, especially those with detected vibrational modes. Third, we assume the emitting source size does not change as a function of excitation energy, though we tried to mitigate this issue by changing the source size toward certain spatial/velocity components when temperature gradients were invoked. As a result, we do not expect all of our fits to have $\chi^2_{red} \sim 1$. These calculations, however, do convey which models reproduce the data best.

From Table 3.5 we see that a little less than half (43%) of the XCLASS models have $\chi^2_{red} \leq 1.5$ indicating excellent agreement between the data and models. Another group, 34% of the fits, have $\chi^2_{red} = 1.5$ – 3.5, which by eye fit the data quite well, but do not agree with the data as closely as those models with $\chi^2_{red} \leq 1.5$. Finally, 23% of the fits have $\chi^2_{red} > 3.5$, that do not reproduce the data as well as the former two categories. For the most part, these models have high χ^2_{red} values because LTE is not a good approximation or they were very optically thick. We note, the HCl and OH models have high χ^2_{red} values because they contain an absorption component which we did not fit (see Sec. 3.5).

Using our XCLASS models as a template for the data, we computed the number

of detected lines, N_L, and total integrated intensity in velocity space, $\int T_{mb} dv$, toward each spatial/velocity components for each molecular fit. These values are reported in Table 3.6 and are organized such that the total integrated intensity toward all components (last column) is in descending order. For these calculations, we consider a "line" to be any feature with a discernible peak given the resolution of HIFI. Hence, a detected "line" which contains multiple unresolved hyperfine transitions, for example, is only counted once. In order for a line to be considered detected, it had to have a peak intensity ≥ 3 times the local RMS, where we used a single RMS for each band which was computed on the T_{mb} scale after the data had been uniformly smoothed to a velocity resolution of ~ 0.5 km/s.

From Table 3.6, we see that CH_3OH (sum of A and E) is the most emissive molecule, both in terms of total integrated flux and number of detected lines. After methanol, the total integrated flux is dominated by molecules with strong plateau components (e.g. CO, SO_2, and H_2O). Dimethyl ether is second most emissive complex organic in terms of total integrated intensity, while methyl formate has the highest number of detected lines after methanol and its isotopologues. Summing N_L from all modeled species we obtain a total of $\sim 1.7 \times 10^4$ identified lines in the Orion KL HIFI survey.

3.4.2 Abundances

We compute molecular abundances by dividing the column densities in Tables 3.4 by N_{H_2} values given in Table 3.2. These abundances were derived using high resolution spectroscopy over the widest frequency coverage ever obtained toward Orion KL, employing the same instrument with close to uniform efficiency. We emphasize each complex organic was typically constrained by over 500 lines that, when combined with the mm data, encompassed all excitation energies. The emission from lighter molecules (e.g. HCN, CS, etc.), with more widely spaced transitions, is also globally constrained in terms of excitation energy because of the wide band width.

For the rare isotopologue models, we obtained molecular abundances by multiplying N_{tot} by an assumed isotopic ratio. When more than one isotopologue was observed

for a given molecule, they were averaged together. We assume the following isotopic ratios: $^{12}C/^{13}C = 45$, $^{32}S/^{33}S = 75$, $^{32}S/^{34}S = 20$, $^{16}O/^{18}O = 250$, and $^{14}N/^{15}N = 234$. The C, S, and O ratios were taken from Tercero et al. (2010), who derived these values by modeling OCS and H_2CS emission present in the IRAM 30 m line survey. The N isotopic ratio was taken from Adande & Ziurys (2012), who compute this value by analyzing CN hyperfine transitions, from which reliable optical depths could be measured. Molecular abundances, derived from our XCLASS models, are given in Table 3.7. For those molecules that required temperature gradients, abundances were computed using N_{tot} from the sub-component which dominated the emission in the HIFI scan. In other words, we did not consider cooler sub-components we added primarily to fit the IRAM data. Our derived abundances are thus most strongly coupled to the warmest gas in Orion KL.

Fig. 3.15 is a bar chart which plots abundance as a function of molecule. Each spatial/velocity component is plotted in a different panel. Hot core models with $v_{lsr} \geq 6.5$ km/s are identified as originating from from hot core (s). XCLASS abundances for these models are plotted in blue. The molecules are labeled along the x-axis and are roughly organized such that the cyanides are on the left side of the plot, the sulfur bearing species are in the middle, and the complex oxygen bearing organics are on the right.

3.4.3 Unidentified Lines

The residual between the observed spectrum and the full band model allowed us to estimate the number of unidentified, "U", lines. We identified channels emitted from U lines by first uniformly smoothing the data to a velocity resolution of ~ 1 km/s to increase the S/N. Residuals between the full band model and data were then computed by stepping across the spectrum in frequency intervals corresponding roughly to 1000 km/s. At each interval, we calculated the RMS noise level and subtracted a local baseline. A channel was then flagged as emitting from a U line if it was greater than 3 times the local RMS in bands 1 – 5 or 5 times the local RMS in bands 6 and 7 as well as 3 times the intensity level predicted by the full band model. The larger

RMS factor for bands 6 and 7 exists because of the presence of strong standing waves and baseline offsets which are more prevalent in the high frequency bands. Based on these criteria, we flagged 8261 channels in emission. If we assume a line width of 5 km/s, this corresponds to 1652 U lines. According to the full band model, we identify $\sim 1.7 \times 10^4$ at or above the 3 σ noise level, leading to a U line fraction of $\sim 10\%$.

Fig. 3.16 (upper panel) is a histogram that plots the number of U lines as a function of frequency. From the plot, we see that the number of U lines is highest at the low frequency end of the survey and quickly drops off as a function of frequency. In bands 6 and 7, we have, for the most part, identified every detected line, with the exception of a possible few (< 5). Most of the channels flagged as U lines in these bands are isolated outliers or lines from known molecules not fit very well by the full band model. The lower panel of Fig. 3.16 plots the fraction of U line channels as a function of frequency. That is, the number of U line channels, x_{ul}, divided by $x_{ul} + x_{em}$, where x_{em} is the number of emission channels ($> 3\ \sigma$) according to the full band model. The plot shows that this fraction stays relatively constant between 6 – 9% for $\nu < 1270$ GHz. There is thus not a U line over density at the low frequency end of the survey. The increased U line fraction in the highest frequency bin ($\nu = 1759$ – 1919 GHz) is produced by the presence of a possible strong U line at approximately 1897.15 GHz.

3.5 Description of Individual Molecular Fits

We present details of individual XCLASS models in this section. Unless otherwise stated, we compute critical densities using collision rates obtained from the LAMDA database (Schöier et al., 2005). In the following discussion, the J quantum number correspond to the total angular momentum of the molecule, i.e. $\mathbf{J} = \mathbf{N} + \mathbf{S} + \mathbf{L}$ where $\mathbf{N}$, $\mathbf{S}$, and $\mathbf{L}$ are the rotation, electron spin, and electron orbital angular momentum quantum numbers. For species without electric angular momentum, $\mathbf{J} = \mathbf{N}$ and rotation transitions are referenced by ΔJ. For molecules with electric angular momentum, we label the rotation levels as N_J. Energy levels for symmetric rotors

are labeled as J_K where K corresponds to the angular momentum along the axis of symmetry. For asymmetric rotors, energy levels are labeled as $J_{Ka,Kc}$, where Ka and Kc represent the angular momentum along the axis of symmetry in the oblate and prolate symmetric top limits, respectively. In instances when we required a temperature gradient to fit the observed emission, we only report the rotation temperatures of the sub-component which dominates the flux at HIFI frequencies in the sub-sections that follow. Temperatures for the other sub-components are given Table 3.4.

3.5.1 CH_3CN

We observe methyl cyanide (CH_3CN) toward the hot core, plateau, and compact ridge. In the HIFI band, we detect transitions over an approximate range in excitation energy of 330 – 1800 K over K ladders spanning J = 27 up to 49. In the IRAM survey, we detect transitions from $E_{up} \approx 18$ K to 660 K (J = 5 to 13). We also detect emission from both ^{13}C isotopologues as well as the $\nu_8 = 1$ vibrationally excited mode from levels with excitation energies > 2000 K. We derive T_{rot} = 260, 230, and 120 K for the hot core, compact ridge, and plateau, respectively.

3.5.2 C_2H_3CN

We observe vinyl cyanide (C_2H_3CN) only toward the hot core. In the HIFI and IRAM surveys we observe transitions over ranges in E_{up} of $\sim$ 600 – 750 K and 20 – 600 K, respectively. The HIFI scan was thus only sensitive to the most highly excited emission lines. We derive a T_{rot} = 215 K toward the hot core.

3.5.3 C_2H_5CN

We observe ethyl cyanide (C_2H_5CN) exclusively toward the hot core. In the HIFI scan, we observe transitions over a range in E_{up} of $\sim$ 120 – 550 K, while in the IRAM survey we detect transitions with excitation energies as low as $\sim$ 15 K. We required 2 components with T_{rot} = 136 and 300 K, to fit the observed emission. The line profiles observed in the IRAM scan have line widths that are approximately a factor of 2 wider than observed in the HIFI data, even for transitions with similar excitation energies. Given its intricate structure, it is possible the IRAM data is pointed toward

a more turbulent region within the hot core. As a result, our model fits the HIFI data well, but tends to over predict transitions observed in the IRAM survey because of the wider line widths.

3.5.4 HC_3N

Cyanoacetylene (HC_3N) is detected toward the hot core and the plateau. In the HIFI and IRAM scans, we observe transitions from J = 53 – 52 to approximately 77 – 76 ($E_{up} \approx 620 - 1300$ K) and J = 9 – 8 to 30 – 29 ($E_{up} \approx 20 - 200$ K), respectively. In addition, we observe the $\nu_7 = 1$ vibrationally excited mode toward both spatial/velocity components up to excitation energies of $\sim$ 1320 K (J $\approx$ 67). We required a temperature gradient to fit the hot core component while the plateau is fit well by a single temperature model. We adopted a consistent set of rotation temperatures for both the $\nu = 0$ and $\nu_7 = 1$ models. Our derived rotation temperatures for the hot core and plateau are 210 K and 115 K, respectively.

3.5.5 HCN

We observe hydrogen cyanide (HCN) in all spatial velocity components. In addition to the main isotopologue, we also detect $H^{13}CN$, $HC^{15}N$, and DCN in the ground vibrational state. Transitions from J = 6 – 5 to 21 – 20 ($E_{up} \approx 90 - 980$ K) are detected in the HIFI scan. The IRAM survey contains the 1 – 0 and 2 – 1 transitions. We also observe emission in the $\nu_2 = 1$ (HCN and $H^{13}CN$) and $\nu_2 = 2$ (HCN) vibrationally excited states only toward the hot core. The $\nu_2 = 1$ HCN line profiles contain two velocity components, one wide ($\Delta v = 15$ km/s) and one more narrow ($\Delta v = 7$ km/s), both at $v_{lsr} = 5.0$ km/s, consistent with the hot core. In the $\nu_2 = 2$ state, we detect emission at excitation energies as high as $\sim$ 2400 K. We do not require temperature gradients to fit the compact or extended ridge. Additional cooler components, however, were needed to reproduce the observed IRAM line intensities in the hot core and plateau. Our derived T_{rot} values are 210 K for the hot core, 120 K for the compact ridge, 130 K for the plateau, and 40 K for the extended ridge.

3.5.6 HNC

Hydrogen isocyanide (HNC) is detected toward all spatial/velocity components in the main isotopologue. We also observe $HN^{13}C$ toward the hot core and plateau. Between the HIFI and IRAM surveys, we detect the ground state line up to approximately the J = 16 – 15 transition ($E_{up} \approx 590$ K). The $\nu_2 = 1$ vibrationally excited mode is observed toward the hot core in the main isotopologue up to excitation energies of $\sim$ 1120 (J $\sim$ 14). We required temperature gradients to fit both the hot core and plateau. The compact and extended ridge, however, were well fit by single temperature models. We used a consistent set of rotation temperatures for both detected isotopologues and the $\nu 2 = 1$ model. Our derived T_{rot} values are 220 K for the hot core, 100 K for the compact ridge, 115 K for the plateau, and 27 K for the extended ridge.

3.5.7 CN

Cyanide radical (CN) emission is detected toward the plateau and extended ridge. We do not observe hyperfine structure at HIFI frequencies, but do detect the doublets brought about by the unpaired electron. Combining the IRAM and HIFI scans, we observe from the ground rotation transition to the N = 8 – 7 doublet ($E_{up} = 196$ K). Both the plateau and extended ridge are well fit by single temperature XCLASS models, although the N = 1 – 0 lines, (detected in the IRAM scan), are somewhat under predicted in the extended ridge by no more than a factor of $\sim$ 1.5. Our derived rotation temperatures are 43 and 21 K for the plateau and extended ridge, respectively, indicating CN is probing cool material or is sub-thermally excited.

3.5.8 HNCO

We observe isocyanic acid (HNCO) along with its rarer isotopologue $HN^{13}CO$ toward the hot core and plateau. In the HIFI scan, we detect transitions over excitation energies of $\sim$ 40 – 1050 K. In the IRAM survey, we detect somewhat lower energy lines over an E_{up} range of $\sim$ 10 – 600 K. Temperature gradients were required to fit both components. We adopted a consistent set of rotation temperatures to fit

both the main and ^{13}C isotopologues using XCLASS. We derive T_{rot} values of 209 K and 168 K for the hot core and plateau, respectively. Non-LTE excitation effects are likely important for this molecule because transitions between K_a ladders are not collisionally excited. Rather, these states are pumped via the far-IR (Churchwell et al., 1986). Our derived values for T_{rot} thus may more closely couple to the dust temperature than the kinetic temperature of the gas. As a result, our LTE fits do deviate somewhat from the observations. In particular, our model tends to under predict A-type transitions and over predict B-type transitions. Nevertheless, our values for T_{rot} and N_{tot} agree well with previous spectral survey studies who have also noted this effect (see e.g. Comito et al., 2005; Schilke et al., 2001, 1997).

3.5.9 HCO^+

Formylium (HCO^+) and its rarer isotopologue $H^{13}CO^+$ are detected toward all spatial/velocity components. Between the IRAM and HIFI scans, we observe transitions from the ground state line up to J = 17 – 16 (E_{up} = 655 K). We require a temperature gradient only for the plateau. The cooler sub-component, most prominent in the IRAM survey, is significantly wider (Δv = 50 km/s) than the warmer sub-component (Δv = 30 km/s) indicating the presence of higher velocity material. We used a consistent set of rotation temperatures for the main and ^{13}C isotopologues. Our derived rotation temperatures are 190 K for the hot core (s), 80 K for the compact ridge, 135 K for the plateau, and 27 K for the extended ridge. For the compact ridge, we needed a source size larger than 10″, our adopted standard θ_s for this region. Specifically, fits with θ_s = 10″ always under predicted emission from the main isotopologue because the modeled emission became too optically thick before the observed peak intensity could be reached. Consequently, we use a source size of 25″ for our XCLASS compact ridge model. This may indicate that HCO^+ is more spatially extended than other compact ridge tracers, or that emission we are attributing to the compact ridge is indeed originating from hotter than typically observed gas in the extended ridge. HCO^+ maps presented by Vogel et al. (1984), suggest the latter scenario is possible. They observe highly extended emission ($\theta_s \geq$ 45″) toward two peaks to the NE and

SW of IRc2 at $v_{lsr} \sim 11.4$ and 7.4 km/s, respectively. Comparing the position of these peaks with a similar map of SO, they argue HCO^+ is tracing a region of the extended ridge that is impeding outflowing gas. Peak line intensities toward the 7.4 km/s peak suggest gas kinetic temperatures ≥ 78 K, which is similar to the T_{rot} we derive for our compact ridge component.

3.5.10 CCH

We observe Ethynyl (CCH) emission toward the extended ridge and hot core (s). In the HIFI survey, we detect transitions from N = 6 – 5 to 10 – 9 ($E_{up} = 90 – 230$ K). While in the IRAM scan, we detect the N = 1 – 0 and 2 – 1 transitions ($E_{up} \leq 13$ K). Hyperfine components are resolved in the IRAM data but not in the HIFI scan. The doublets, however, brought about by the unpaired electron are separated enough that they are resolved in both surveys. We did not need to invoke temperature gradients to fit either the hot core, $T_{rot} = 53$ K, or extended ridge, $T_{rot} = 37$ K. The hot core rotation temperature is very low compared to other molecules detected toward this region, indicating that CCH is either probing very cool gas within the hot core or is sub-thermally excited.

3.5.11 CS

We observe carbon monosulfide (CS) along with the rarer ^{13}CS, $C^{34}S$, and $C^{33}S$ isotopologues toward all spatial velocity components. In the HIFI and IRAM scans, we detect transitions from J = 10 – 9 to 26 – 25 ($E_{up} \approx 130 – 820$ K) and 2 – 1 to 5 – 4 ($E_{up} \approx 10 – 40$ K), respectively. A temperature gradient was only required for the plateau in the main isotopologue. For the rarer isotopologues, the plateau component is only detected in the IRAM scan, which is why we only include a cool plateau sub-component for these species. We adopted a consistent set of rotation temperatures for the rarer isotopologues. We derive T_{rot} values of 100 K for the hot core (s), 225 K for the compact ridge, 155 K for the plateau, and 35 K for the extended ridge.

3.5.12 H_2S

Hydrogen sulfide (H_2S) is observed toward the hot core, plateau, and extended ridge. In addition to the main isotopologue, we also detect $H_2{}^{34}S$ and $H_2{}^{33}S$. In the HIFI scan, we observe emission over a range in excitation energies of $\sim$ 50 – 1230 K. The IRAM data contains the $1_{1,0}$ – $1_{0,1}$ transition (E_{up} = 28 K) for all three isotopologues, providing an additional constraint at low excitation. A detailed study of H_2S emission toward the hot core is presented in Chapter 4 and we use the abundance derived there. We used single temperature models for all but the plateau, which required a gradient. A consistent set of rotation temperatures was used for the rarer isotopologues. Our derived rotation temperatures are 145 K for the hot core, 115 K for the plateau, and 50 K for the extended ridge. For the hot core, we used a source size of 6″ to be consistent with the detailed analysis presented in Chapter 4 (see Sec. 4.3.2).

3.5.13 H_2CS

We observe thioformaldehyde (H_2CS) emission toward the hot core (s) and compact ridge. In the HIFI scan, we detect emission over a range in E_{up} of approximately 200 – 600 K. While in the IRAM survey, we detect transitions at lower excitation over an E_{up} range of $\sim$ 10 – 200 K. Temperature gradients were not required for either component in our XCLASS model. We derive rotation temperatures of 120 and 100 K for the hot core and compact ridge, respectively. Tercero et al. (2010) present analysis of the H_2CS emission in the IRAM survey. Despite the fact that they assume a different compact ridge source size (15″) and a different temperature for the hot core (225 K) in their analysis, we derive column densities that agree to within a factor of 2.5. They also derive a ortho/para ratio of $\sim$ 2.0 $\pm$ 0.7 for both the compact ridge and hot core (small variations existed between isotopologues), which, given the uncertainty, is consistent with the equilibrium value of 3. We used a spectroscopic catalog that did not separate the ortho and para species (CDMS catalog) and found that a single ortho + para model fit the data well, which, for the temperatures considered in our models, points to an ortho/para ratio of 3.

3.5.14 OCS

We observe carbonyl sulfide (OCS) emission toward all spatial/velocity components. In the HIFI and IRAM scans, we detect transitions from J = 40 – 39 to approximately 61 – 60 ($E_{up} \approx 480$ – 1100 K) and 7 – 6 to 23 – 22 ($E_{up} \approx 20$ – 160 K), respectively. We do not detect vibrationally excited emission in the HIFI dataset, but do in the IRAM scan ($\nu_2 = 1$). Temperature gradients were not needed to fit any component using XCLASS. Our derived rotation temperatures are 190 K for the hot core, 165 K for the compact ridge, 110 K for the plateau, and 10 K for the extended ridge. The OCS emission within the IRAM survey, including the vibrationally excited emission is analyzed in detail by Tercero et al. (2010). As a result, we do not include a vibrationally excited OCS model here. Our derived column densities agree to within a factor of 2.5 with that derived in the Tercero study.

3.5.15 SO

Sulfur monoxide (SO) is detected toward the hot core, plateau, and extended ridge. We also observe the rarer isotopologues ^{33}SO and ^{34}SO toward the hot core and plateau. In the HIFI scan, we detect transitions over a range in E_{up} of $\sim$ 10 – 900 K. While in the IRAM survey, we detect additional low energy rotation transitions with $E_{up} \lesssim 100$ K. Using XCLASS, we required temperature gradients to fit both the hot core and plateau. A consistent set of rotation temperatures was adopted for the rarer species. We derive T_{rot} values of 258 K for the hot core, 163 K for the plateau, and 60 K for the extended ridge. Line profiles are dominated by the plateau especially at low excitation. Hence, our reported extended ridge model is not very well constrained because it manifests as a small bump atop the strong plateau component. Our model reproduces the observed line intensities of the $\Delta N = 1$, $\Delta J = 1$ transitions well, which are quite strong in the HIFI scan (T_{peak} values can be as high as 25 K). We, however, note that our model systematically under predicts the less emissive $\Delta N = 1$, $\Delta J = 0$ rotation transitions (observed $T_{peak} \lesssim 3$ K). We even detect several $\Delta N = 3$ lines at the 1 K level, which our model also under predicts. The factor by which we typically under predict these lines is ~ 5, but may be higher for the weakest detected

transitions in this category.

3.5.16 SO_2

The main isotopologue of sulfur dioxide (SO_2) is observed toward all spatial velocity components. The rarer isotopologues $^{33}SO_2$ and $^{34}SO_2$ are also detected toward the hot core and plateau. Additionally, we observe the $\nu_2 = 1$ vibrationally excited mode toward the hot core. In the HIFI scan, we detect transitions with E_{up} from $\sim$ 70 K to $\sim$ 1100 K, the most highly excited lines originating from the $\nu 2 = 1$ state. The IRAM survey probes excitation energies as low as $\sim$10 K. Modeling the data with XCLASS, we were able to adopt a single set of rotation temperatures for all isotopologues. We derive T_{rot} values of 240 K for the hot core, 100 K for the compact ridge, 150 K for the plateau, and 50 K for the extended ridge. Temperature gradients were required to fit the hot core and compact ridge. We fit the $\nu_2 = 1$ emission using the same T_{rot} as the ground vibrational state.

3.5.17 HCS^+

We detect the main isotopologue of thioformylium (HCS^+) exclusively toward the compact ridge. In the HIFI scan, we observe transitions from J = 12 – 11 (E_{up} = 160 K) to approximately 20 – 19 (E_{up} = 430 K). The IRAM data contains the J = 2 – 1, 4 – 3, and 5 – 4 transitions (E_{up} = 6 – 31 K). All observed HCS^+ lines in both the IRAM and HIFI scans are weak ($T_{peak} \lesssim 1$ K). The HCS^+ emission in the IRAM scan was analyzed previously by Tercero et al. (2010). Our derived column density ($N_{tot} = 1.8 \times 10^{14}$ cm^{-2}) is a factor of 2.2 times higher than that reported by the Tercero study for the compact ridge. Our results are thus in close agreement with theirs despite our assumption of LTE and the fact that Tercero et al. (2010) assume $\theta_s = 15''$ for the compact ridge, which is likely the biggest reason our HCS^+ column density is somewhat higher than theirs.

3.5.18 SiS

We detect the main isotopologue of silicon monosulfide (SiS) toward the plateau. We observe transitions from J = 27 – 26 to approximately 41 – 40 ($E_{up} \approx$ 330 –

750 K) in the HIFI scan, while the IRAM survey contains transitions from J = 5 – 4 to 15 – 14 ($E_{up} \approx 10 - 110$ K). The observed emission is fit well by a single temperature XCLASS model with T_{rot} = 145 K. Tercero et al. (2011) analyze, in detail, the SiS emission within the IRAM dataset. In that study, they model the SiS lines by including contributions from the hot core, plateau, and the so called 15.5 km/s component. At HIFI frequencies, we only observe SiS emission from the plateau. As a result, we do not include models for the other two components. The Tercero study derives a column density of 3.5×10^{14} cm^{-2} toward the plateau, not assuming LTE. Our derived column density of 3.7×10^{14} cm^{-2} thus agrees well with the Tercero result, despite our assumption of LTE.

3.5.19 SiO

Silicon monoxide (SiO) emission is detected toward the plateau. In addition to the main isotopologue, we also detect emission from ^{29}SiO and ^{30}SiO. The HIFI survey contains transitions from J = 12 – 11 to 29 – 28 (E_{up}= 163 – 905 K) and the IRAM scan contains transitions from J = 2 – 1 to 6 – 5 (E_{up}= 6 – 44 K). We fit the line emission in XCLASS by splitting the model into high velocity plateau (v_{lsr} = 10.0 km/s, Δv = 35 km/s) and low velocity plateau (v_{lsr} = 7 – 8.0 km/s, Δv = 15 km/s) components. These two components do not necessarily correspond to the LVF and HVF as defined in Sec. 3.3.1. Both components require temperature gradients in order to fit both the HIFI and IRAM observations. We were able to adopt a consistent set of rotation temperatures for all isotopologues. We derive T_{rot} values of 120 K and 270 K for the high and low velocity plateau components, respectively. Tercero et al. (2011) modeled the SiO emission in the IRAM survey using MADEX non-LTE code in a similar way. In addition to low and high velocity plateau components, they include hot core, compact ridge, and extended ridge components to fit the line profiles. We do not observe compact or extended ridge components at HIFI frequencies and thus do not include models for those components here. It is, however, possible that the component we attribute to the low velocity plateau may include emission from the hot core. Nevertheless, we find a two component model reproduces the data well.

3.5.20 HCl

We observe the J = 1 – 0, 2 – 1, and 3 – 2 transitions of hydrochloric acid (HCl) and $H^{37}Cl$ in the HIFI scan. The line profiles are wide (Δv = 25 km/s), indicating an origin in the plateau. Because of the wide line profiles, we do not resolve the hyperfine components. The J = 2 – 1 and 3 – 2 lines show blue shifted absorption in both the main and ^{37}Cl isotopologues, while the ground state lines do not. The absorption component appears also to be wide ($\Delta v \gtrsim 15$ km/s), though it is difficult to constrain because of the blending between absorption and emission. The wide line width suggests the absorbing layer also originates from the plateau. Because our full band model is based on the continuum subtracted data, we did not fit the absorption component in this work. We did not require a temperature gradient to fit the emission, which is not surprising given that both models are based only on three lines each. Nevertheless, we derive T_{rot} = 73 K for both isotopologues. In order to reproduce the observed peak line intensities, we needed to use a 50″ source size as opposed to 30″, indicating HCl is quite extended toward the plateau. It is also possible that emission from other components, (e.g. the hot core), may also contribute. However, given the dominance of the plateau and the presence of blue shifted absorption in the excited lines, adding such components would not be meaningfully constrained.

3.5.21 NS

We observe nitric sulfide (NS) emission toward the hot core and compact ridge. In the HIFI scan, we detect NS transitions from J = 21/2 – 19/2 to approximately J = 47/2 – 45/2 (E_{up}= 134 – 960 K). In the IRAM survey, we observe emission from the J = 5/2 – 3/2 and J = 7/2 – 5/2 transitions ($E_{up} \approx$ 10 – 340 K), the hyperfine structure being visible in the IRAM scan but not at HIFI frequencies. We, however, do observe the splitting from the unpaired electron in the HIFI spectrum. We did not require temperature gradients for either component in our XCLASS model and derive T_{rot} = 105 and 200 K for the hot core and compact ridge, respectively. We note that our model systematically predicts line centers $\sim$ 10 – 20 MHz higher than observed for many transitions $\gtrsim$ 1 THz. Such differences are commensurate with the

quoted uncertainties in the line catalog (JPL database) used to produce the model, which begin to noticeably increase as a function of frequency for $\nu \gtrsim 700$ GHz.

3.5.22 NO

We observe nitric oxide (NO) emission toward all spatial/velocity components. In the HIFI scan, we detect transitions from J = 11/2 – 9/2 to approximately J = 29/2 – 27/2 ($E_{up} \approx 80$ – 540 K). In the IRAM survey, we detect hyperfine lines from the ground state rotation transition J = 3/2 – 1/2. As with the other nitrogen bearing radicals in this survey, we do not detect hyperfine structure in the HIFI scan, but do observe the doublets produced by the spin angular momentum of the unpaired electron. We did not need temperature gradients for any spatial/velocity component and derive T_{rot} values of 180 K for the hot core, 70 K for the compact ridge, 155 K for the plateau, and 60 K for the extended ridge.

3.5.23 H_2CO

We observe formaldehyde (H_2CO) emission toward the hot core, compact ridge, and plateau. We also detect the rarer isotopologue $H_2{}^{13}CO$ toward the hot core and compact ridge, as well as the singly deuterated species, HDCO, only toward the compact ridge. In the HIFI and IRAM surveys, we detect transitions over ranges in excitation energy of ~ 100 – 1000 K and ~ 10 – 90 K, respectively. Single temperature models were used for all spatial/velocity components except the plateau. For H_2CO and $H_2{}^{13}CO$, we were forced to use a source size of $15''$ for the compact ridge because models with $\theta_s = 10''$, our standard source size for the compact ridge, predicted line intensities that were too weak. We derive T_{rot} values of 135 K for the hot core, 50 K for the compact ridge, and 88 K for the plateau. A more detailed analysis of formaldehyde emission in the HIFI scan is presented by Neill et al. (2013, submitted), who use the RADEX non-LTE code (van der Tak et al., 2007) to model the formaldehyde emission toward the compact ridge in order to obtain a robust D/H ratio. As discussed in the Neill study, the HDCO line profiles differ somewhat from other compact ridge tracers in that they contain two narrow components (both with $\Delta v = 2.2$ km/s): one at

v_{lsr} = 7.7 km/s, near the canonical velocity of the compact ridge, and the other at v_{lsr} = 10.0 km/s. The detection of the higher velocity component points to the presence of a highly deuterated clump, the origin of which remains unclear. As a result, our HDCO model contains two velocity components at 7.7 and 10.0 km/s. Both of which assume a source size 12.5″ to remain consistent with the Neill study.

3.5.24 H_2CCO

We detect ketene (H_2CCO) emission only toward the compact ridge. In the HIFI scan, the observed line intensities are quite weak ($T_{peak} < 0.5$ K). Nevertheless, we detect transitions in the HIFI scan over an approximate range in E_{up} of 300 – 500 K. While in the IRAM survey we observe transitions with excitation energies from $\sim$ 20 to 150 K. The line profiles in the IRAM scan contain a wider component ($v_{lsr} \approx 6$ km/s, $\Delta v \approx 15$ km/s) that we attribute to the hot core. Because this component is only visible in the IRAM data, we do not include a hot core model in this work. We derive T_{rot} = 100 K with no temperature gradient.

3.5.25 H_2O

We detect water (H_2O) emission toward the hot core, compact ridge, and plateau. In addition to the main isotopologue, we also detect $H_2{}^{18}O$, $H_2{}^{17}O$, HDO, $HD^{18}O$, and D_2O. Absorption lines are also observed in the lower energy lines. Water abundances as well as D/H ratios toward the different spatial/velocity components are derived in Neill et al. (2013).

3.5.26 CH_2NH

Methanimine (NH_2CHO) is detected toward the hot core and extended ride. In the HIFI and IRAM scans, we detect transitions over ranges in E_{up} of $\sim$ 15 – 370 K and 5 – 50 K, respectively. No temperature gradients were required for either component. We derive T_{rot} = 130 and 40 K toward the hot core and extended ridge, respectively.

3.5.27 NH_2CHO

We observe formamide (NH_2CHO) emission only toward the compact ridge. The HIFI and IRAM scans contain transitions over ranges in excitation energy of approximately 280 – 660 K and 10 – 150 K, respectively. We detect only the more emissive a-type transitions, the b-types having over a factor of 4 lower dipole moment than the a-types. Even at low excitation, the lines are weak ($T_{peak} < 0.5$ K) in the HIFI survey. There are hints of a wider component in the IRAM scan, possibly from the hot core, but we do not include a model for that component here. A single temperature model with $T_{rot} = 190$ K fits the observed emission well. Our derived T_{rot} agrees well with that reported in Sutton et al. (1995), which we, admittedly, used as a starting point for our own fit.

3.5.28 C_2H_5OH

Ethanol (C_2H_5OH) emission is observed toward the compact ridge. In the HIFI and IRAM surveys, we detect transitions over approximate ranges in E_{up} of 100 – 470 K and 30 – 210 K, respectively. We did not need a temperature gradient to fit the observed emission and derive $T_{rot} = 110$ K. As with several other complex organics detected in this survey, the observed line profiles are weak ($T_{peak} < 1$ K).

3.5.29 CH_3OCH_3

Dimethyl ether (CH_3OCH_3) is detected toward the hot core (s) and compact ridge. In the HIFI and IRAM scans, we observe transitions over ranges in excitation energy of $\sim$ 90 – 620 K and 5 – 510 K, respectively. Single temperature models are sufficient to fit both components. We derive $T_{rot} = 100$ and 110 K for the hot core (s) and compact ridge, respectively.

3.5.30 CH_3OCHO

We observe methyl formate (CH_3OCHO) only toward the compact ridge. Transitions in the HIFI and IRAM surveys are detected over E_{up} ranges of $\sim$ 160 – 740 K and 10 – 300 K, respectively. A fraction of the more highly excited lines are from the $v_t = 1$ torsionally excited state. Favre et al. (2011) observed multiple transitions of

CH_3OCHO using the Plateau de Bure Interferometer (PdBI). In that study, they fit the observed line profiles using two velocity components, one at v_{lsr} = 7.5 km/s and the other at 9.2 km/s, both of which have Δv = 1.7 km/s. We find that a single compact ridge model, with v_{lsr} = 8.0 km/s and Δv = 2.8 km/s, reproduces the HIFI observations well, though some line profiles hint at the possibility for two components. When Favre et al. (2011) combine both of their velocity components, our derived T_{rot} agrees well with that reported in the Favre study toward MF1 (T_{rot} = 100 K), the largest methyl formate clump observed toward the compact ridge. Our derived column density is also commensurate with that derived by Favre et al. (2011) toward MF1.

3.5.31 CH_3OH

We observe methanol (CH_3OH) emission toward the hot core (s) and compact ridge. In addition to the main isotopologue, we also detect $^{13}CH_3OH$ as well as the singly deuterated CH_3OD and CH_2DOH isotopologues toward these same spatial/velocity components. In both the HIFI and IRAM surveys, we detect transitions over a range in excitation energy of approximately 20 – 1200 K. The most highly excited emission originates from torsionally excited states. Methanol is the most emissive molecule in the HIFI scan, both in terms of number of lines and total integrated flux. In fact, CH_3OH is the only complex organic detected throughout the entire HIFI scan, even at high frequencies (> 1.4 THz). Unfortunately, our derive χ^2_{red} statistics indicate that methanol and its isotopologues are not fit well by our XCLASS models indicating that LTE is not a good approximation for this species. Nevertheless, we derive T_{rot} = 128 and 140 K for hot core (s) and compact ridge.

3.5.32 HF

The J = 1 – 0 transition of hydrogen fluoride (HF) is detected in absorption toward the plateau (low velocity flow). The detection of this feature along with a column density estimate of 2.9 × 10^{13} cm^{-2}, which corresponds to an abundance of 1.0 × 10^{-10}, is reported in Phillips et al. (2010).

3.5.33 CO

We observe ^{13}CO, C^{18}O, and C^{17}O toward all spatial/velocity components and ^{13}C^{18}O toward the extended/compact ridge. In the HIFI scan, we detect transitions from 5 – 4 up to 17 – 16 (E_{up} = 80 – 810 K), while the IRAM survey contains the 1 – 0 ground state transition. Our reported T_{rot} values are the same as those used in Plume et al. (2012), who analyze the C^{18}O and C^{17}O emission in the HIFI scan to obtain robust H_2 column density measurements toward the different spatial/velocity components within Orion KL, except for the plateau, toward which we use a higher T_{rot}. These T_{rot} values are 150 K for the hot core, 125 K for the compact ridge, 130 K for the plateau, and 40 K for the extended ridge. As described in Sec. 3.3.3, we adopt these N_{H_2} estimates in this study modulo small adjustments for the plateau and compact ridge. With this said, we note that our reported plateau C^{18}O column density is a factor of 1.8 times higher than the N_{H_2} value given in Table 3.2 times 2.0×10^{-7}, our assumed CO abundance. The reason for this discrepancy is that a somewhat wider plateau line width (Δv = 25 km/s) than used in the Plume study (Δv = 20 km/s) appears to produce better agreement between the model and data. As a result, we were forced to increase the C^{18}O column density by a factor of 1.8 to properly fit the data. The main isotopologue, of course, is also detected in the HIFI scan. These lines, however, are so optically thick that an XCLASS model would be meaningless. We therefore fit Gaussian profiles to these lines and provide that as the full band model.

3.5.34 NH_2

Only the ortho species of amidogen (NH_2) is detected toward the hot core and extended ridge. In the HIFI scan, we detect from the ground state up to excitation energies of $\sim$ 375 K. No transitions are detected in the IRAM survey. We derive T_{rot} = 130 and 50 K toward the hot core and extended ridge, respectively.

3.5.35 NH_3

We observe ammonia (NH_3) toward the hot core, plateau, and extended ridge. We also detect $^{15}NH_3$ and NH_2D as well as the $\nu_2 = 1$ vibrationally excited mode. Emission from the $\nu_2 = 1$ mode and NH_2D are only detected toward the hot core, while $^{15}NH_3$ is detected toward the hot core and extended ridge. The main and ^{15}N isotopologues are observed via low energy rotation transitions which include the ground state ortho and para lines up to the $3_0 - 2_0$ ortho transition ($E_{up} \approx 170$ K). Because the deuterium atom breaks the symmetry of the ammonia molecule, we observe NH_2D transitions within and across K ladders up to excitation energies of ~ 600 K. Vibrationally excited emission is detected from energy levels as high as ~ 2000 K. A detailed analysis of the NH_2D emission in the HIFI scan is presented by Neill et al. (2013, submitted) for the purpose of obtaining a robust ammonia D/H ratio. The observed NH_3 and $^{15}NH_3$ transitions do not cover a large range in excitation energy. The lines from the main isotopologue, moreover, have a blue shifted absorption component, which we do not attempt to fit here. Based on the $\nu_2 = 1$ and NH_2D emission, we derive a $T_{rot} = 250$ K toward the hot core.

3.5.36 OH

We observe the hydroxyl radical (OH) toward the plateau and the deuterated isotopologue (OD) toward the compact ridge. For both species, we detect only the $^2\Pi_{1/2}$ J = 3/2 – 1/2 doublet in the HIFI scan. We used T_{rot} =125 K, characteristic of the compact ridge, to fit the OD lines. We, however, note that this rotation temperature is not well constrained because only one E_{up} is sampled. The OH lines are very optically thick.

3.6 Discussion

The χ^2_{red} values reported in Table 3.5, in general, indicate excellent agreement between the data and models. Most of the complex organics, in particular, have low χ^2_{red} values ($\lesssim 1$), demonstrating that LTE is a good approximation for these species, and suggests an origin in high density gas ($> 10^6$ cm^{-3}). The obvious exception to this

is the main isotopologue of methanol ($\chi^2_{\rm red} > 6$). This is likely mainly the result of the fact that CH_3OH emission is very optically thick. Moreover, given we detect torsionally excited emission, deviations from LTE may be the result of mid/far-IR pumping.

In addition to molecular abundances, our XCLASS models provide rotation temperatures for each modeled species, which, under the assumption of LTE, estimates the local gas kinetic temperature. The distribution of rotation temperatures toward each spatial/velocity component therefore yields insight into the thermal structure within each region. Fig. 3.17 shows histograms of rotation temperature in four panels, each representing a different spatial/velocity component. Within each panel, the black solid curve corresponds to the $T_{\rm rot}$ distribution of all molecules detected toward that component. The solid green, dashed red, and dashed blue lines represent cyanides, sulfur bearing molecules, and complex oxygen bearing organics, respectively. For molecules fit with a temperature gradient, we only include the $T_{\rm rot}$ which corresponds to the sub-component that dominates the emission in the HIFI survey. Molecules with multiple detected isotopologues, furthermore, were only counted once in Fig. 3.17.

The spread in $T_{\rm rot}$ is much larger toward the hot core relative to the other spatial/velocity components, suggesting the hot core is the most heterogeneous region probed by our data. Cyanides furthermore account for 5 of the 10 molecules with $T_{\rm rot} > 200$ K. We note the cyanide in the 125 – 150 K bin, C_2H_5CN with $T_{\rm rot} = 136$ K, required an additional compact 300 K sub-component to fit lines at high excitation. Sulfur bearing molecules also tend to be warmer than average toward the hot core, although less universally so than the cyanides. Specifically, sulfur bearing molecules that also contain oxygen (i.e. OCS, SO, and SO_2) are the hottest, having rotation temperatures > 175 K.

The wide distribution of rotation temperatures in the hot core suggests a more complex thermal structure than toward the other spatial/velocity components within Orion KL. In particular, there are a significant number of hot core molecules with $T_{\rm rot} > 175$ K, which is where the other distributions, (save a few species in the com-

pact ridge), terminate. Interferometric studies of molecular emission toward the hot core have certainly demonstrated that this region is both chemically and physically intricate, having structure on scales $\lesssim$ 1-2″ (Wang et al., 2010; Goddi et al., 2011). The molecules with the highest T_{rot} are likely probing the hottest gas toward the hot core. If the hot core does harbor one or more massive protostars, such gas would be closest to these self luminous sources. More discussion on the chemical implications of our results will be given in Chapter 5.

Molecules displaying high rotation temperatures toward the hot core may also have been pumped by the strong IR continuum characteristic of this region (Genzel & Stutzki, 1989; De Buizer et al., 2012). Non-LTE studies of both H_2O (Neill et al., 2013) and H_2S (Chapter 4 of this work) emission within the Orion KL HIFI scan required an enhanced continuum for $\lambda < 100$ μm, where the continuum is likely optically thick, relative to what is observed to explain the emission of both these light hydrides. Other studies have also needed to invoke strong IR radiation fields to explain NH_3 (Hermsen et al., 1988) and HDO (Jacq et al., 1990) emission toward the hot core. The presence of such a continuum may be redistributing the population levels of these molecules to reflect a T_{rot} higher than the actual kinetic temperature. Because the continuum is optically thick for much of the far-IR, this points to an origin near a heavily embedded self-luminous source or sources.

The compact ridge T_{rot} distribution is much narrower than that of the hot core with a little under half of the distribution falling in the 100 – 125 K bin, indicating a more quiescent, uniform environment. There are however, several high temperature outliers. Just as in the hot core, CH_3CN is among the hottest molecules, while HNC is significantly cooler (T_{rot} = 100 K). Unlike the hot core, however, HCN does not appear to be particularly warm (T_{rot} = 100 K). We, however, note that this temperature is not well constrained because the compact ridge was only detected in the main isotopologue and these line profiles are dominated by the plateau, which can act as an absorbing layer (e.g. H_2O and HF). Also similar to the hot core, the O/S bearing molecules OCS is markedly warm (T_{rot} = 165 K). The other S bearing species populating the high temperature part of the compact ridge distribution, on

the other hand, are NS and CS, both of which have $T_{rot} \approx 100$ K in the hot core.

To determine if the molecules displaying hotter T_{rot} values correspond to a spatially distinct region within the compact ridge, we once again employed the ALMA band 6 SV data. Fortunately emission from two molecules which have high T_{rot} measurements toward the compact ridge, OCS ($T_{rot} = 155$ K) and CS ($T_{rot} = 190$ K), were present in the ALMA survey. Fig. 3.18 plots integrated emission maps of the OCS 20 – 19 and CS 5 – 4 in the left and right panels as blue contours, respectively. The emission was integrated between $v_{lsr} = 7.6 - 8.3$ km/s to avoid contributions from the hot core and plateau. We also overlay emission from CH_3OCHO $18_{7,11}$ – $17_{7,10}$, in both panels as yellow contours. Methyl formate is a prominent compact ridge tracer with a derived $T_{rot} = 110$ K, close to the peak of the compact ridge T_{rot} distribution. The CH_3OCHO contours surround a cavity that is likely carved out by the LVF (Irvine et al., 1987; Plambeck et al., 2009; Favre et al., 2011). The two southern methyl formate peaks, furthermore, correspond to MF1 and MF3 using the labeling conventions of Favre et al. (2011). The continuum is also overlaid on both panels as a gray scale, which mainly traces IRc2, the infrared source closest to the hot core. From the plot, we see that both the OCS and CS peaks are offset from MF1 and MF3, occurring midway between the two and closer to the edge of the cavity. The higher rotation temperatures may therefore be a result of the interactions between LVF and the compact ridge.

As with the compact ridge, the plateau also has a narrower T_{rot} distribution than the hot core. Unlike the compact ridge, there is no subset of molecules with conspicuously high temperatures (> 175 K) relative to the main distribution. Unlike the hot core, cyanides are not among the hottest molecules detected toward this component. Sulfur bearing species, however, appear on the warmer end of the distribution, the hottest being SO, SO_2 (similar to the hot core), and SiS ($T_{rot} \sim 140 - 165$ K). We note that the hottest molecule detected toward the plateau is HNCO ($T_{rot} = 168$ K), which is also the only non-cyanide/non-sulfur bearing molecule detected at the high temperature end of the hot core T_{rot} distribution. This is likely the result of pumping from the far-IR, which Churchwell et al. (1986) has shown is significant for this

molecule (see Sec. 3.5.8).

Finally, the extended ridge displays the narrowest of all four temperature distributions centered at $\sim$ 40 K, exemplifying the cool, quiescent nature of this region. Although there is not much variation in T_{rot}, sulfur bearing molecules tend to be warmer than average. Cyanides, on the other hand, are on the cooler side of the distribution.

3.7 Conclusions

We have presented a full band analysis of the HIFI spectral survey toward Orion KL, which spans a frequency range from 480 to 1907 GHz. In all, we detect emission from 36 molecules (76 isotopologues). We modeled the molecular emission using the XCLASS program, which assumes LTE level populations. A χ^2_{red} analysis indicates that most models fit the data well. In particular, complex organics are well fit by LTE models which indicates that gas densities are high ($> 10^6$ cm^{-3}). According to our models, we detect $\sim 1.7 \times 10^4$ lines in the HIFI scan and estimate a U line fraction of $\sim$ 10%.

Using column densities derived from our models, we compute molecular abundances toward the hot core, compact ridge, plateau, and extended ridge. Plotting the distribution of rotation temperatures toward each spatial/velocity component indicates the HIFI scan probes a diversity of environments toward Orion KL. The T_{rot} distribution for the hot core is significantly wider than those corresponding to the other spatial/velocity components suggesting the hot core is a more heterogeneous region. Although the compact ridge T_{rot} distribution is quite narrow, it does have a high temperature tail. Interferometric maps obtained from the ALMA SV data indicate that emission from OCS and CS, two molecules at the high temperature end of the compact ridge distribution, peaks closer to the LVF. Higher temperatures thus may be the result of interactions between the LVF and compact ridge.

Table 3.1: HIFI Observations

Band	Observation Date	OD	OBSID	Frequency Range (GHz)	Int. Time (S)	RMS (mK)
1a	1 March 2010	291	1342191504	479.5 – 561.5	7565	20
1b	2 March 2010	292	1342191592	554.5 – 636.5	9551	20
2a	12 April 2010	333	1342194540	626.0 – 726.0	14221	20
2b	7 March 2010	297	1342191755	714.1 – 801.3	9052	30
3a	29 September 2010	504	1342205334	799.0 – 860.0	8113	40
3b	19 March 2010	309	1342192329	858.1 – 961.0	12590	40
4a	2 March 2010	293	1342191601	949.1 – 1061.0	11092	50
4b	3 March 2010	294	1342191649	1049.9 – 1122.0	11100	80
5a	6 March 2010	296	1342191725	1108.1 – 1242.8	14903	100
5b	19 March 2011	674	1342216387	1227.1 – 1280.0	17027	100
6a (HC)	6 March 2010	296	1342191727	1425.9 – 1535.0	14578	700
6b (HC)	22 March 2010	312	1342192562	1573.3 – 1702.8	9253	800
7a (HC)	15 April 2010	336	1342194732	1697.2 – 1797.8	10678	800
7b (HC)	23 March 2010	313	1342192673	1788.4 – 1906.5	14240	800
6a (CR)	6 March 2010	296	1342191728	1425.9 – 1535.0	14578	700
6b (CR)	22 March 2010	312	1342192563	1573.3 – 1702.8	9253	800
7a (CR)	15 April 2010	336	1342194733	1697.2 – 1797.8	10678	800
7b (CR)	23 March 2010	313	1342192674	1788.4 – 1906.5	14240	800

Table 3.2: Standard Values for θ_s and N_{H_2}

Component	θ_s ($''$)	N_{H_2} (cm^{-2})
Hot Core	10	3.1×10^{23}
Compact Ridge	10	3.9×10^{23}
Plateau	30	2.8×10^{23}
Extended Ridge	180	7.1×10^{22}

Table 3.3: Optically Thick XCLASS Models

Molecule	Hot Core	Compact Ridge	Plateau	Extended Ridge
CH_3CN	X	X	X	...
CH_3OH-A/E	X	X	...	...
^{13}CO	X	X	X	X
CS	X	X		X
H_2CO	X	X		...
$H_2{}^{17}O$	X	X	X	...
$H_2{}^{18}O$	X	X	X	...
H_2S	X	...	X	
HCN	X		X	X
$H^{13}CN$	X	...	X	
HCO^+	X	X	X	X
HNC	X		X	
HNCO	X	...	X	...
NH_3	X	...	X	X
OH	...	...	X	...
SiO	...	...	X	...
SO	X	...	X	
SO_2	X		X	

"X" indicates an optically thick model, "..." indicates a non-detection, and no mark indicates an optically thin model exists in Table 3.4.

Table 3.4: XCLASS Model Parameters

Molecule	θ_s ($''$)	T_{rot} (K)	N_{tot} (cm^{-2})	v_{lsr} (km/s)	Δv (km/s)
Hot Core					
C_2H_3CN	10	215	2.7×10^{15}	5.0	5.5
C_2H_5CN	10	136	2.1×10^{16}	5.0	7.0
C_2H_5CN	5	300	6.5×10^{15}	5.0	7.0
CH_2NH	10	130	1.3×10^{15}	6.0	8.0
CH_3CN,ν_8=1	10	260	3.7×10^{15}	6.0	6.0
$^{13}CH_3CN$	10	260	1.3×10^{14}	5.5	8.0
$CH_3{}^{13}CN$	10	260	1.3×10^{14}	5.5	8.0
$H_2{}^{34}S$	6	145	3.8×10^{16}	4.5	8.6
$H_2{}^{33}S$	6	145	1.1×10^{16}	4.5	8.6
HC_3N	20	10	1.0×10^{15}	5.5	6.5
HC_3N	10	210	1.5×10^{15}	5.5	6.5
HC_3N,ν_7=1	20	10	1.0×10^{15}	5.5	6.5
HC_3N,ν_7=1	10	210	1.5×10^{15}	5.5	6.5
HCN,ν_2=2	10	217	4.7×10^{17}	6.0	7.0
$H^{13}CN$,ν_2=1	10	157	3.5×10^{16}	5.5	6.0
$HC^{15}N$	20	20	2.0×10^{14}	4.5	10.0
$HC^{15}N$	10	210	3.5×10^{14}	4.5	10.0
DCN	20	20	9.0×10^{13}	6.0	8.0
DCN	10	210	1.8×10^{14}	5.5	8.0
HNC,ν_2=1	10	220	1.3×10^{15}	4.5	7.0
$HN^{13}C$	20	15	1.0×10^{13}	2.5	8.5
$HN^{13}C$	10	220	3.5×10^{13}	2.5	8.5
$HN^{13}CO$	20	30	4.5×10^{13}	6.3	6.2
$HN^{13}CO$	10	209	4.9×10^{14}	6.3	6.2
o-NH_2	10	130	1.3×10^{15}	6.0	12.0
NH_3,ν_2	10	250	1.3×10^{17}	6.0	5.5

NO	10	180	1.7×10^{17}	6.0	8.0
NS	10	105	2.1×10^{15}	4.2	10.5
OCS	10	190	3.2×10^{16}	6.0	8.0
^{34}SO	20	70	4.5×10^{14}	4.5	7.0
^{34}SO	10	258	1.8×10^{15}	4.5	7.0
^{33}SO	20	70	2.3×10^{14}	4.5	7.0
^{33}SO	10	258	5.0×10^{14}	4.5	7.0
SO_2,ν_2=1	10	240	9.0×10^{16}	6.0	7.0
$^{34}SO_2$	20	50	1.1×10^{15}	5.0	8.0
$^{34}SO_2$	10	240	5.0×10^{15}	5.0	8.0
$^{33}SO_2$	20	50	2.6×10^{14}	5.0	8.0
$^{33}SO_2$	10	240	1.3×10^{15}	5.0	8.0
Hot Core (S)					
CCH	10	53	2.3×10^{15}	7.0	13.5
CH_3OCH_3	10	100	2.1×10^{16}	7.2	10.0
$^{13}CH_3OH$	10	128	1.5×10^{16}	7.5	6.5
CH_3OD-A	10	128	7.8×10^{14}	7.5	6.5
CH_3OD-E	10	128	7.8×10^{14}	7.5	6.5
CH_2DOH	10	128	1.3×10^{15}	7.5	6.5
$C^{18}O$	10	150	1.9×10^{17}	6.5	9.0
$C^{17}O$	10	150	6.3×10^{16}	6.5	9.0
^{13}CS	10	100	9.7×10^{14}	6.5	10.5
$C^{34}S$	10	100	1.9×10^{15}	6.5	10.5
$C^{33}S$	10	100	6.4×10^{14}	6.5	10.5
$H_2{}^{13}CO$	10	135	8.5×10^{14}	6.5	13.0
H_2CS	10	120	4.6×10^{15}	7.5	7.5
$H^{13}CO^+$	10	190	9.0×10^{12}	8.0	10.0
Compact Ridge					
C_2H_5OH	10	110	6.5×10^{15}	7.8	2.5

CH_3CN,ν_8=1	10	230	2.8×10^{15}	7.5	4.0
$^{13}CH_3CN$	10	230	1.1×10^{14}	7.5	4.0
$CH_3{}^{13}CN$	10	230	1.1×10^{14}	7.5	4.0
CH_3OCH_3	10	110	6.5×10^{16}	8.0	3.2
CH_3OCHO	10	110	1.3×10^{17}	8.0	2.8
$^{13}CH_3OH$	10	140	1.0×10^{16}	7.8	2.5
CH_3OD-A	10	140	1.7×10^{15}	7.8	2.5
CH_3OD-E	10	140	1.7×10^{15}	7.8	2.5
CH_2DOH	10	140	8.1×10^{15}	7.8	2.5
$C^{18}O$	10	125	1.3×10^{17}	8.0	4.0
$C^{17}O$	10	125	2.0×10^{16}	8.0	4.0
$^{13}C^{18}O$	10	125	3.2×10^{15}	8.0	4.0
^{13}CS	10	225	2.0×10^{14}	7.2	4.0
$C^{34}S$	10	225	2.9×10^{14}	7.2	4.0
$C^{33}S$	10	225	1.6×10^{14}	7.2	4.0
H_2CCO	10	100	2.0×10^{15}	8.0	3.0
$H_2{}^{13}CO$	15	50	3.8×10^{14}	8.0	3.5
HDCO	12	60	1.8×10^{14}	10.0	2.2
HDCO	12	60	2.6×10^{14}	7.7	2.2
H_2CS	10	100	2.9×10^{15}	8.0	3.0
HCN	10	120	5.5×10^{14}	11.0	6.0
$H^{13}CO^+$	25	80	1.5×10^{12}	9.0	5.5
HCS^+	10	105	1.8×10^{14}	9.0	6.0
HNC	10	100	2.0×10^{13}	8.5	3.0
NH_2CHO	10	190	7.5×10^{14}	7.2	4.8
NO	10	70	3.2×10^{16}	7.2	2.5
NS	10	200	6.1×10^{14}	7.7	5.5
OCS	10	165	4.3×10^{15}	7.5	2.5
OD	10	125	2.5×10^{14}	8.0	3.5

SO_2	10	100	1.8×10^{15}	8.2	3.0
			Plateau		
$CH_3CN,\nu_8=1$	30	120	1.0×10^{16}	6.0	18.0
$^{13}CH_3CN$	30	120	6.5×10^{13}	6.0	18.0
$CH_3{}^{13}CN$	30	120	6.5×10^{13}	6.0	18.0
CN	30	43	6.3×10^{14}	8.0	20.0
$C^{18}O$	30	130	1.3×10^{17}	8.5	25.0
$C^{17}O$	30	130	3.7×10^{16}	8.5	25.0
CS	30	30	1.2×10^{15}	8.7	26.7
CS	30	155	1.8×10^{15}	8.7	26.7
^{13}CS	30	30	6.1×10^{13}	8.7	26.7
$C^{34}S$	30	30	1.5×10^{14}	8.7	26.7
$C^{33}S$	30	30	5.0×10^{13}	8.7	26.7
H_2CO	30	20	1.1×10^{15}	8.0	32.0
H_2CO	30	88	3.5×10^{15}	8.0	23.0
$H_2{}^{34}S$	30	12	2.1×10^{15}	9.0	30.0
$H_2{}^{34}S$	30	115	2.5×10^{15}	9.0	30.0
$H_2{}^{33}S$	30	12	5.6×10^{14}	9.0	30.0
$H_2{}^{33}S$	30	115	7.5×10^{14}	9.0	30.0
HC_3N	30	115	1.3×10^{15}	5.5	23.0
$HC_3N,\nu_7=1$	30	115	3.0×10^{15}	5.5	23.0
HCl	50	73	1.4×10^{15}	11.5	25.0
$H^{37}Cl$	50	73	4.9×10^{14}	11.5	25.0
$HC^{15}N$	30	25	2.3×10^{14}	7.5	28.0
$HC^{15}N$	30	130	1.0×10^{14}	8.5	28.0
DCN	30	25	3.5×10^{13}	5.5	20.0
DCN	30	130	3.2×10^{13}	8.5	20.0
$H^{13}CO^+$	30	25	1.5×10^{13}	9.0	50.0
$H^{13}CO^+$	30	135	1.7×10^{12}	8.5	30.0
$HN^{13}C$	30	20	8.0×10^{12}	7.5	28.0

$HN^{13}C$	30	115	4.3×10^{12}	7.5	25.0
$HN^{13}CO$	30	25	2.0×10^{13}	9.0	20.0
$HN^{13}CO$	30	168	4.3×10^{13}	9.0	20.0
NO	30	155	1.5×10^{17}	8.0	27.0
OCS	30	110	1.2×10^{16}	5.0	21.0
^{29}SiO	30	25	1.5×10^{14}	10.0	35.0
^{29}SiO	30	120	4.8×10^{13}	10.0	35.0
^{29}SiO	30	18	1.0×10^{14}	8.0	15.0
^{29}SiO	30	270	5.2×10^{13}	7.0	15.0
^{30}SiO	30	25	1.6×10^{14}	10.0	35.0
^{30}SiO	30	120	3.0×10^{13}	10.0	35.0
^{30}SiO	30	18	6.7×10^{13}	8.0	15.0
^{30}SiO	30	270	4.1×10^{13}	7.0	15.0
SiS	30	145	4.3×10^{14}	8.5	23.0
^{34}SO	30	65	4.6×10^{15}	10.0	26.0
^{34}SO	30	163	3.0×10^{15}	10.0	26.0
^{33}SO	30	65	1.1×10^{15}	10.0	26.0
^{33}SO	30	163	7.5×10^{14}	10.0	26.0
$^{34}SO_2$	30	20	3.0×10^{14}	9.5	30.0
$^{34}SO_2$	30	50	2.5×10^{15}	9.5	30.0
$^{34}SO_2$	30	150	4.7×10^{15}	9.5	23.0
$^{33}SO_2$	30	20	7.1×10^{13}	9.5	30.0
$^{33}SO_2$	30	50	5.9×10^{14}	9.5	30.0
$^{33}SO_2$	30	150	9.8×10^{14}	9.5	23.0
Extended Ridge					
CCH	180	37	4.5×10^{14}	8.8	3.5
CH_2NH	180	40	2.0×10^{13}	9.0	4.0
CN	180	21	2.2×10^{14}	9.0	3.5
$C^{18}O$	180	40	1.4×10^{16}	9.0	3.0
$C^{17}O$	180	40	6.2×10^{15}	9.0	3.0

$^{13}C^{18}O$	180	40	2.0×10^{14}	9.0	3.0
^{13}CS	180	35	3.7×10^{13}	8.0	4.0
$C^{34}S$	180	35	6.8×10^{13}	8.0	4.0
$C^{33}S$	180	35	1.3×10^{13}	8.0	4.0
H_2S	180	50	1.0×10^{14}	8.6	3.0
$H^{13}CN$	180	40	1.7×10^{13}	9.0	4.0
DCN	180	40	8.5×10^{12}	8.5	4.0
$H^{13}CO^+$	180	27	5.3×10^{12}	9.0	4.5
HNC	180	27	2.5×10^{13}	8.5	3.0
o-NH_2	180	50	2.0×10^{13}	8.0	3.0
NO	180	60	7.5×10^{15}	10.0	5.0
OCS	180	10	2.0×10^{15}	7.5	2.5
SO	180	60	7.8×10^{14}	10.5	5.0
SO_2	180	50	3.0×10^{14}	8.2	3.0

Table 3.5: $\chi^2_{\rm red}$ Statistics for Molecular Fits

Molecule	$\theta_{\rm eff}$ ($''$)	$N_{\rm chan}$	$\chi^2_{\rm red}$	Catalog
$^{13}C^{18}O$	100	3	...	CDMS
OD	10	2	...	JPL
$CH_3{}^{13}CN$	20	12	...	CDMS
$H^{37}Cl$	50	109	0.3	JPL
OCS	20	183	0.4	CDMS
$C^{17}O$	20	99	0.5	CDMS
$H^{13}CN,\nu_2{=}1$	10	150	0.5	CDMS
$C^{18}O$	20	286	0.5	CDMS
NO	20	1388	0.6	JPL
H_2CCO	10	24	0.6	CDMS
D_2O	3	13	0.7	CDMS
HCS^+	10	28	0.7	CDMS
$HNC,\nu_2{=}1$	10	94	0.7	CDMS
^{29}SiO	30	233	0.8	CDMS
^{13}CS	20	129	0.8	CDMS
^{13}CO	20	739	0.8	CDMS
C_2H_5OH	10	239	0.8	JPL
C_2H_3CN	10	60	0.8	CDMS
C_2H_5CN	10	1706	0.8	JPL
^{33}SO	20	796	0.9	CDMS
NH_2CHO	10	281	0.9	CDMS
HCN	20	871	0.9	CDMS
HCO^+	20	740	0.9	CDMS
CH_2NH	100	189	1.0	JPL
SiS	30	123	1.0	CDMS
SiO	30	1127	1.0	CDMS
$^{33}SO_2$	20	671	1.1	CDMS

$^{13}CH_3CN$	20	98	1.1	CDMS
CH_3OD-E	10	343	1.1	JPL
H_2CS	10	478	1.1	CDMS
CN	100	252	1.2	CDMS
CH_3CN-A	20	515	1.2	CDMS
p-NH_3	20	227	1.2	JPL
CCH	100	136	1.3	CDMS
CH_3OCHO	10	1387	1.3	JPL
HC_3N	20	118	1.4	CDMS
CH_3OD-A	10	243	1.4	JPL
$H^{13}CO^+$	20	52	1.6	CDMS
HNCO	20	1458	1.6	CDMS
HDCO	12	58	1.6	CDMS
HNC	20	558	1.6	CDMS
$^{15}NH_3$	100	49	1.6	CDMS
^{34}SO	20	2038	1.6	CDMS
$HC^{15}N$	20	214	1.7	CDMS
$C^{33}S$	20	160	1.7	CDMS
$H_2{}^{33}S$	20	307	1.7	CDMS
CS	20	905	1.8	CDMS
CH_3CN-E	20	874	1.8	CDMS
NH_3,ν_2	10	70	1.9	JPL
$H_2{}^{13}CO$	12	416	1.9	CDMS
NS	10	453	1.9	JPL
CH_3OCH_3	10	2869	2.0	CDMS
DCN	20	312	2.0	CDMS
SO_2,ν_2=1	10	544	2.0	CDMS
HCN,ν_2=2	10	72	2.1	CDMS
HCN,ν_2=1	10	320	2.2	CDMS
$^{13}CH_3OH$	10	2591	2.5	CDMS

^{30}SiO	30	298	2.6	CDMS
$H_2{}^{34}S$	20	660	2.7	CDMS
CH_3CN,ν_8=1	20	984	2.8	JPL
$H^{13}CN$	20	609	2.8	CDMS
SO	20	5799	3.0	CDMS
$HN^{13}CO$	20	68	3.0	JPL
NH_2D	10	135	3.2	CDMS
$^{34}SO_2$	20	5131	3.3	CDMS
o-NH_3	20	147	3.9	JPL
$HD^{18}O$	3	22	4.0	JPL
H_2CO	20	4201	4.3	CDMS
SO_2	20	23490	4.5	CDMS
H_2S	20	1919	5.9	CDMS
CH_2DOH	10	1224	6.9	JPL
$C^{34}S$	20	157	7.2	CDMS
CH_3OH-E	10	15268	7.3	JPL
$HN^{13}C$	20	38	9.4	CDMS
HC_3N,ν_7=1	20	45	10.3	CDMS
HDO	15	1013	12.3	JPL
H_2O,ν_2	3	88	15.0	JPL
$H_2{}^{17}O$	15	668	37.7	JPL
HCl	50	201	45.5	JPL
$H_2{}^{18}O$	15	875	97.4	JPL
o-NH_2	100	290	100.0	CDMS
OH	30	354	175.3	JPL
CH_3OH-A	10	13408	330.7	JPL

Table 3.6: Integrated Flux and Number of Lines

Molecule	N_L	$\int T_{mb} dv$ (K km s^{-1})				
		Hot Core	Compact Ridge	Plateau	Extended Ridge	Total
CO	11	0.0	0.0	61790.8	0.0	61790.8
SO_2	832	10379.1	217.3	46389.5	205.1	57191.0
CH_3OH-E	1902	23313.7	16885.8	0.0	0.0	40199.5
H_2O	35	0.0	0.0	38797.5	0.0	38797.5
CH_3OH-A	1384	22328.1	15812.1	0.0	0.0	38140.2
SO	72	1395.9	0.0	25307.2	244.6	26947.6
H_2CO	140	3520.4	2258.8	4311.1	0.0	10090.3
HCN	14	587.9	297.9	7025.5	107.6	8018.9
^{13}CO	11	1410.6	229.1	4994.3	385.2	7019.2
H_2S	75	2171.3	0.0	4112.5	75.0	6358.7
$^{34}SO_2$	411	1360.0	0.0	4097.4	0.0	5457.4
$H_2{}^{18}O$	23	609.5	67.5	4275.4	0.0	4952.4
CH_3OCH_3	671	1011.1	2982.7	0.0	0.0	3993.8
CS	19	869.4	113.2	2064.9	77.3	3124.8
^{34}SO	56	428.9	0.0	2490.3	0.0	2919.3
OH	2	0.0	0.0	2894.2	0.0	2894.2
HDO	50	1218.3	191.7	1455.7	0.0	2865.7
$^{13}CH_3OH$	890	1656.5	1139.4	0.0	0.0	2795.9
HCO^+	10	470.1	207.0	1625.5	183.9	2486.4
$H_2{}^{17}O$	15	320.2	62.8	2044.5	0.0	2427.5
SiO	17	0.0	0.0	2366.2	0.0	2366.2
NO	29	491.1	35.0	1677.6	98.6	2302.4
HNCO	225	1143.8	0.0	844.7	0.0	1988.5
CH_2DOH	1609	234.9	1493.7	0.0	0.0	1728.6
C_2H_5CN	1109	1719.8	0.0	0.0	0.0	1719.8
$H_2{}^{34}S$	46	805.9	0.0	829.2	0.0	1635.2
CH_3CN-E	205	817.7	244.5	437.6	0.0	1499.8
$H^{13}CN$	13	453.8	0.0	920.0	35.5	1409.2

HCN,ν_2=1	27	1403.9	0.0	0.0	0.0	1403.9
CH_3OCHO	1997	0.0	1279.8	0.0	0.0	1279.8
$^{33}SO_2$	224	356.5	0.0	880.9	0.0	1237.5
$C^{18}O$	7	213.6	120.6	623.6	50.2	1008.0
HNC	10	317.8	12.5	657.5	17.9	1005.8
CH_3CN-A	117	548.7	151.7	281.3	0.0	981.7
p-NH_3	6	134.7	0.0	824.2	19.8	978.8
SO_2,ν_2 =1	389	915.8	0.0	0.0	0.0	915.8
^{33}SO	45	131.0	0.0	623.0	0.0	754.0
CH_3CN,ν_8=1	344	405.3	199.9	137.0	0.0	742.3
$HC^{15}N$	10	342.0	0.0	381.6	0.0	723.5
o-NH_3	3	86.7	0.0	586.9	45.2	718.8
HCl	4	0.0	0.0	701.9	0.0	701.9
$H_2{}^{33}S$	33	310.4	0.0	226.4	0.0	536.8
CH_3OD-E	428	161.0	365.8	0.0	0.0	526.8
CH_3OD-A	394	158.3	360.4	0.0	0.0	518.8
CH_2NH	191	444.4	0.0	0.0	29.9	474.4
o-NH_2	39	391.1	0.0	0.0	77.3	468.4
H_2CS	119	323.6	137.7	0.0	0.0	461.3
$H_2{}^{13}CO$	82	363.6	69.7	0.0	0.0	433.3
C_2H_5OH	783	0.0	407.8	0.0	0.0	407.8
NS	48	222.5	159.5	0.0	0.0	382.0
NH_2D	80	359.7	0.0	0.0	0.0	359.7
$C^{34}S$	16	216.0	99.8	5.0	13.2	333.9
$C^{17}O$	6	81.6	23.1	187.0	22.6	314.2
NH_2CHO	319	0.0	311.5	0.0	0.0	311.5
^{29}SiO	17	0.0	0.0	293.5	0.0	293.5
DCN	11	171.1	0.0	103.8	13.6	288.6
$H^{37}Cl$	2	0.0	0.0	285.6	0.0	285.6
C_2H_3CN	263	269.8	0.0	0.0	0.0	269.8
^{30}SiO	18	0.0	0.0	220.7	0.0	220.7
CN	10	0.0	0.0	156.9	24.7	181.6

^{13}CS	16	104.3	66.0	1.2	4.5	176.0
HN^{13}CO	129	125.7	0.0	48.5	0.0	174.2
H_2O,ν_2	10	173.6	0.0	0.0	0.0	173.6
OCS	29	121.3	10.9	40.7	0.0	172.9
$CH_3{}^{13}CN$	105	71.1	48.5	36.1	0.0	155.7
$^{13}CH_3CN$	107	70.1	47.9	37.3	0.0	155.3
C^{33}S	16	80.1	56.2	1.6	2.5	140.5
HNC,ν_2=1	16	133.7	0.0	0.0	0.0	133.7
HC_3N	34	91.6	0.0	38.7	0.0	130.3
$^{15}NH_3$	7	86.7	0.0	38.3	5.2	130.2
HCN,ν_2=2	24	112.7	0.0	0.0	0.0	112.7
NH_3,ν_2	30	92.7	0.0	0.0	0.0	92.7
H^{13}CN,ν_2=1	18	89.6	0.0	0.0	0.0	89.6
CCH	10	35.1	0.0	0.0	52.5	87.5
SiS	16	0.0	0.0	76.5	0.0	76.5
HDCO	80	0.0	73.0	0.0	0.0	73.0
HN^{13}C	9	39.1	0.0	14.8	0.0	53.9
HD^{18}O	12	52.0	0.0	0.0	0.0	52.0
HC_3N,ν_7=1	44	40.0	0.0	10.8	0.0	50.8
H$^{13}CO^+$	7	15.4	4.6	15.4	7.1	42.5
D_2O	13	32.2	0.0	0.0	0.0	32.2
H_2CCO	50	0.0	20.5	0.0	0.0	20.5
HCS^+	11	0.0	19.2	0.0	0.0	19.2
OD	2	0.0	5.3	0.0	0.0	5.3
$^{13}C^{18}O$	6	0.0	3.8	0.0	0.8	4.6

Table 3.7: Abundances: $N_{tot}(X)/N_{H_2}$

Molecule	Hot Core	Compact Ridge	Plateau	Extended Ridge
CH_3CN	1.89×10^{-8}	1.27×10^{-8}	1.04×10^{-8}	...
C_2H_3CN	8.71×10^{-9}	...	...	...
C_2H_5CN	6.77×10^{-8}	...	...	...
HC_3N	4.84×10^{-9}	...	4.64×10^{-9}	...
HCN	2.64×10^{-7}	1.41×10^{-9}	8.36×10^{-8}	1.08×10^{-8}
HNC	5.08×10^{-9}	5.13×10^{-11}	6.91×10^{-10}	3.52×10^{-10}
CN	...	...	2.25×10^{-9}	3.10×10^{-9}
HNCO	7.11×10^{-8}	...	6.91×10^{-9}	...
NH_2	1.68×10^{-8}	...	...	1.13×10^{-9}
HCO^+	9.68×10^{-10}	1.92×10^{-10}	9.29×10^{-10}	1.97×10^{-9}
CCH	7.42×10^{-9}	...	...	6.34×10^{-9}
CS	1.39×10^{-7}	2.29×10^{-8}	6.43×10^{-9}	1.88×10^{-8}
H_2S	3.06×10^{-6}	...	1.90×10^{-7}	1.41×10^{-9}
H_2CS	1.48×10^{-8}	7.44×10^{-9}	...	...
OCS	1.03×10^{-7}	1.10×10^{-8}	4.29×10^{-8}	2.82×10^{-8}
SO	1.19×10^{-7}	...	2.08×10^{-7}	1.10×10^{-8}
SO_2	3.19×10^{-7}	4.62×10^{-9}	2.99×10^{-7}	4.23×10^{-9}
HCS^+	...	4.62×10^{-10}	...	...
SiS	...	...	1.54×10^{-9}	...
SiO	...	...	3.67×10^{-9}	...
HCl	...	...	5.48×10^{-9}	...
NS	6.77×10^{-9}	1.56×10^{-9}	...	...
NO	5.48×10^{-7}	8.21×10^{-8}	5.36×10^{-7}	1.06×10^{-7}
H_2CO	1.23×10^{-7}	4.38×10^{-8}	1.25×10^{-8}	...
H_2CCO	...	5.13×10^{-9}	...	...
H_2O	6.50×10^{-4}	4.50×10^{-6}	4.80×10^{-6}	...
CH_2NH	4.19×10^{-9}	...	...	2.82×10^{-10}
NH_2CHO	...	1.92×10^{-9}	...	...
C_2H_5OH	...	1.67×10^{-8}	...	...

CH_3OCH_3	6.77×10^{-8}	1.67×10^{-7}	...	...
CH_3OCHO	...	3.33×10^{-7}	...	...
CH_3OH	2.18×10^{-6}	1.15×10^{-6}	...	...
CO[a]	1.00×10^{-4}	1.00×10^{-4}	1.00×10^{-4}	1.00×10^{-4}

[a] assumed abundance (see Sec. 3.3.3)

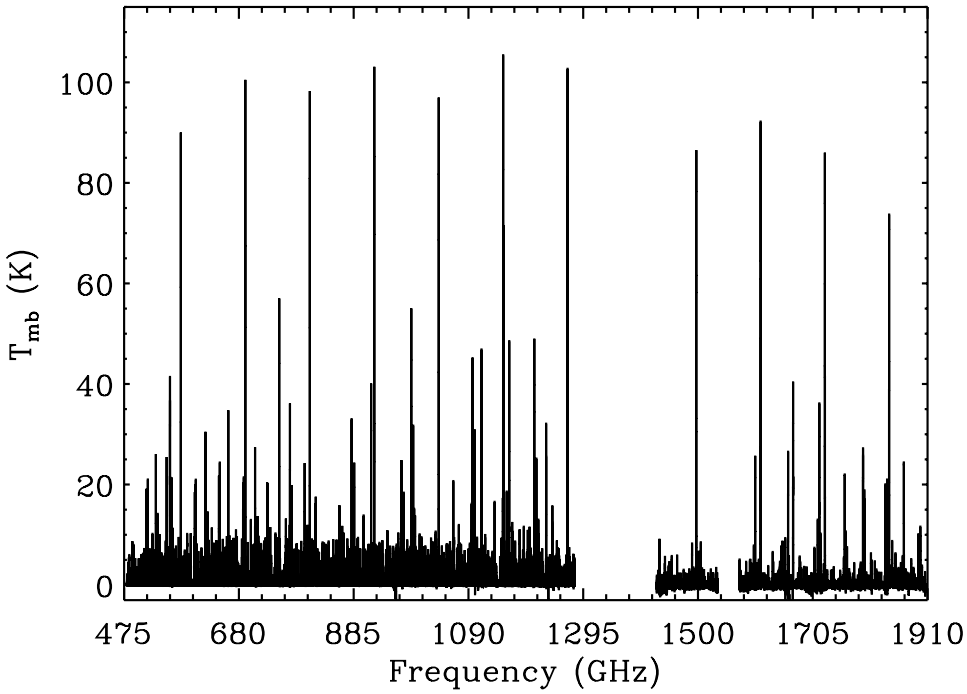

Figure 3.1: The Orion KL HIFI spectral survey is plotted after baseline subtraction. For bands 6 and 7, the hot core pointing is plotted. The data are resampled uniformly to a velocity resolution of $\sim$ 10 km/s to improve the appearance at this scale.

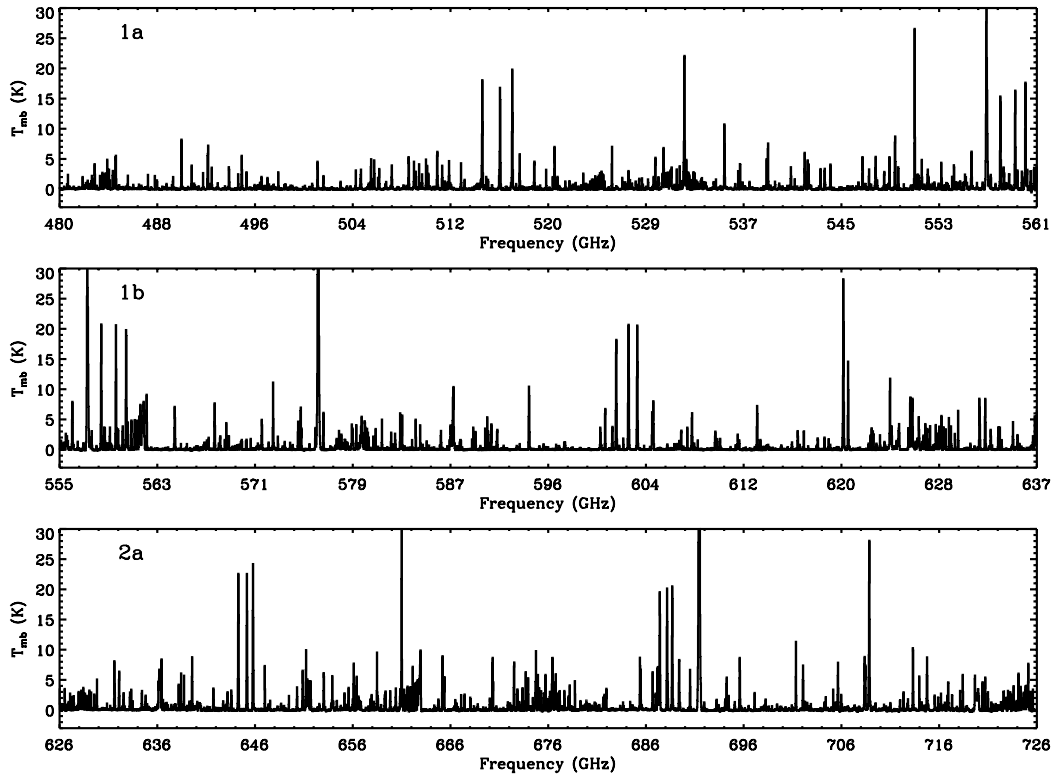

Figure 3.2: Bands 1a, 1b, and 2a of the HIFI spectral survey toward Orion KL are plotted in different panels. The data are resampled to a velocity resolution of $\sim$ 10 km/s to improve the appearance at this scale. Each band is labeled in the upper left hand corner of each panel.

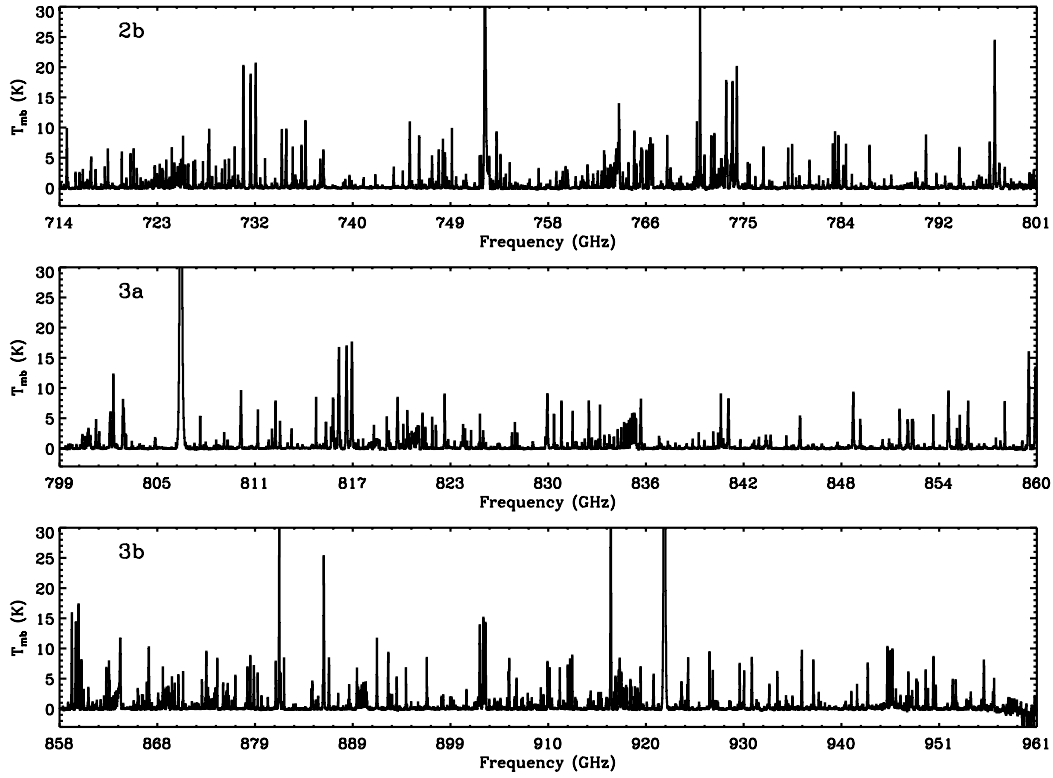

Figure 3.3: Same as Fig. 3.2 for bands 2b, 3a, and 3b.

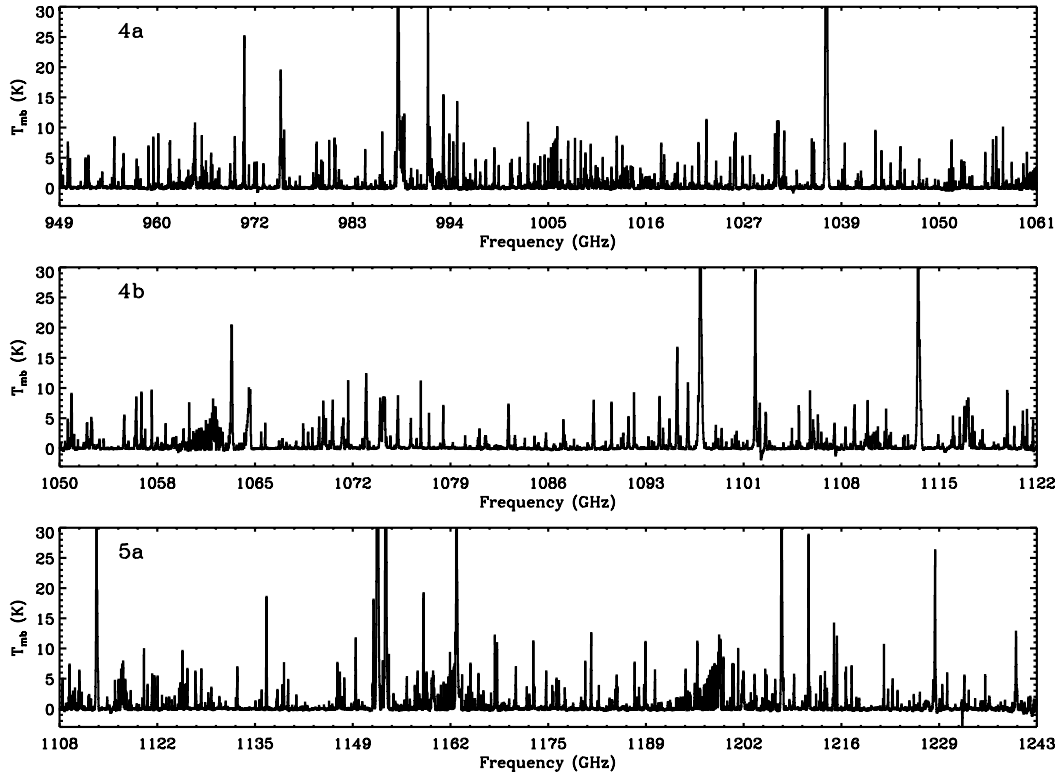

Figure 3.4: Same as Fig. 3.2 for bands 4a, 4b, and 5a.

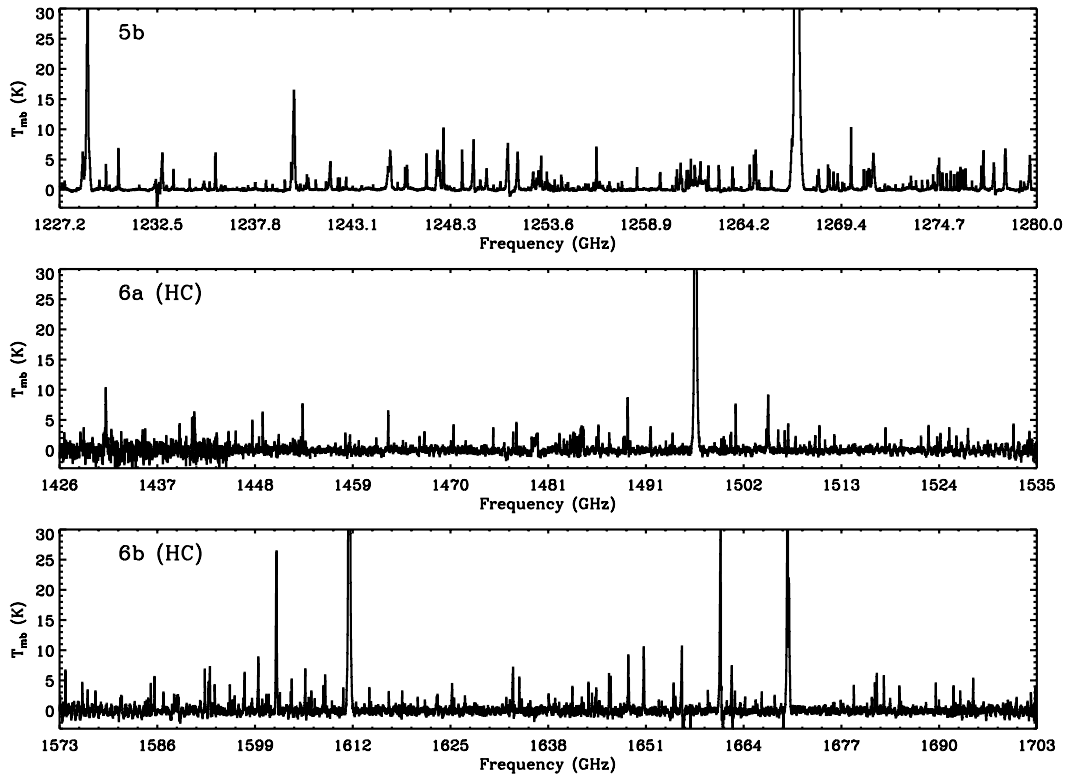

Figure 3.5: Same as Fig. 3.2 for bands 5b, 6a, and 6b. The hot core pointing is plotted for band 6.

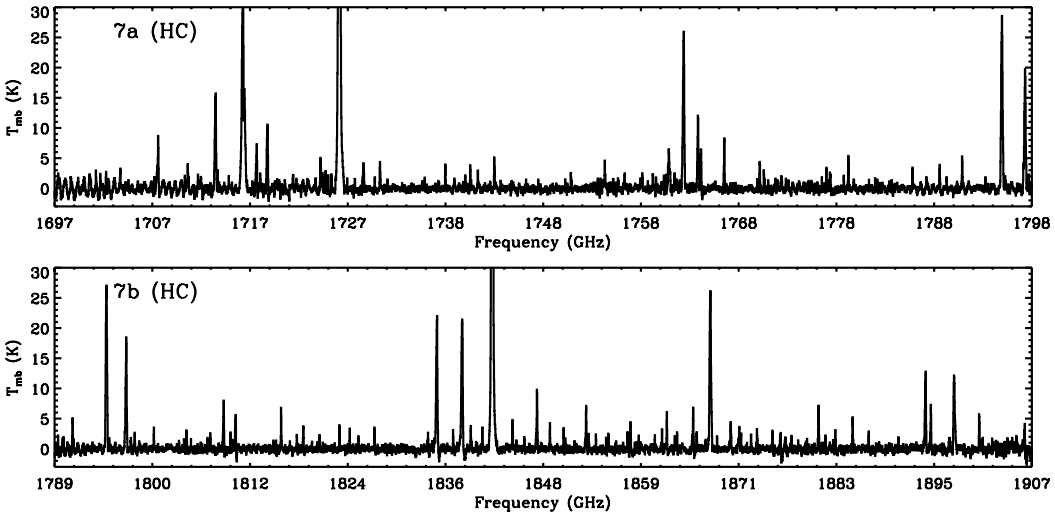

Figure 3.6: Same as Fig. 3.2 for bands 7a and 7b. Only the hot core pointing is plotted.

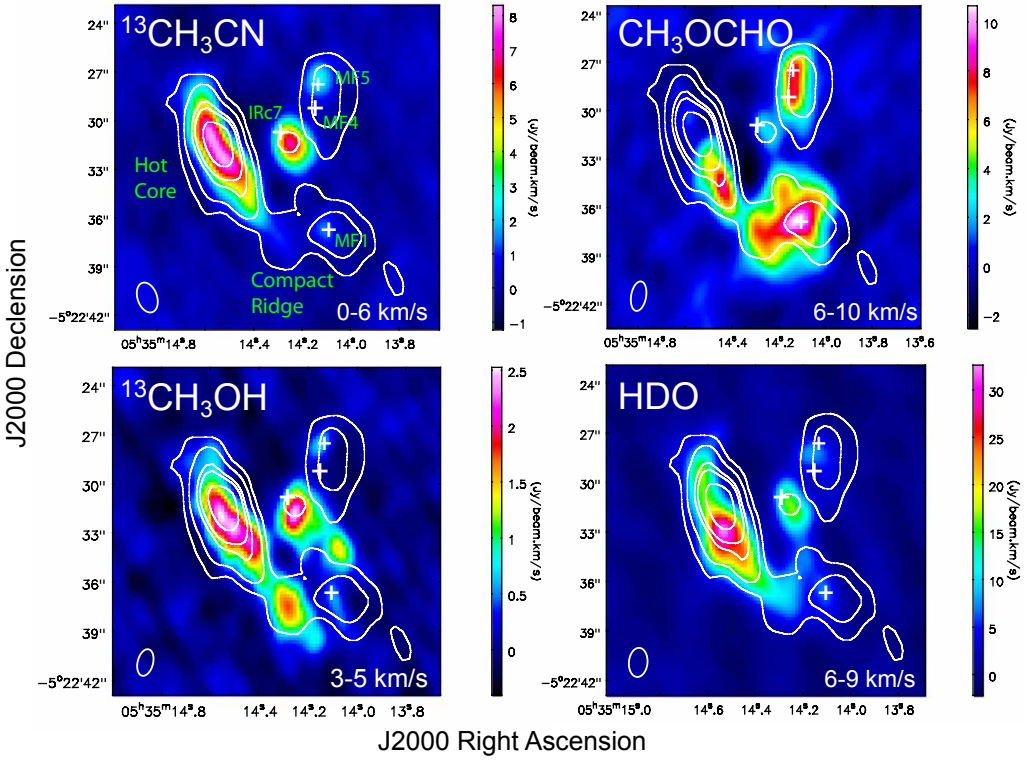

Figure 3.7: Integrated intensity maps obtained from lines in the ALMA-SV dataset are plotted in four different panels as a color scale. The velocity range over which the intensity is integrated is given in each panel. The transitions plotted are $^{13}CH_3CN$ $13_2 - 12_2$ (upper left), $^{13}CH_3OH$-E $5_2 - 4_2$ (lower left), HDO $3_{1,2} - 2_{2,1}$ (lower right), and CH_3OCHO $19_{6,13} - 18_{6,12}$ (upper right). We only show integrated emission in the range 3 – 5 km/s for $^{13}CH_3OH$ because we wanted to avoid contamination from the compact ridge. The continuum at 230.9 GHz is overlaid in each panel as white contours. The contour levels correspond to (0.1, 0.2, 0.4, 0.5, 0.75) × 1.334 Jy beam^{-1}. The continuum peaks corresponding to the hot core and compact ridge are labeled in the upper left panel. The positions of IRc7 and several methyl formate (MF) peaks according to Favre et al. (2011) are indicated by white crosses and labeled in the upper left panel. The synthesized beam size is indicated by an oval in the lower left corner of each panel.

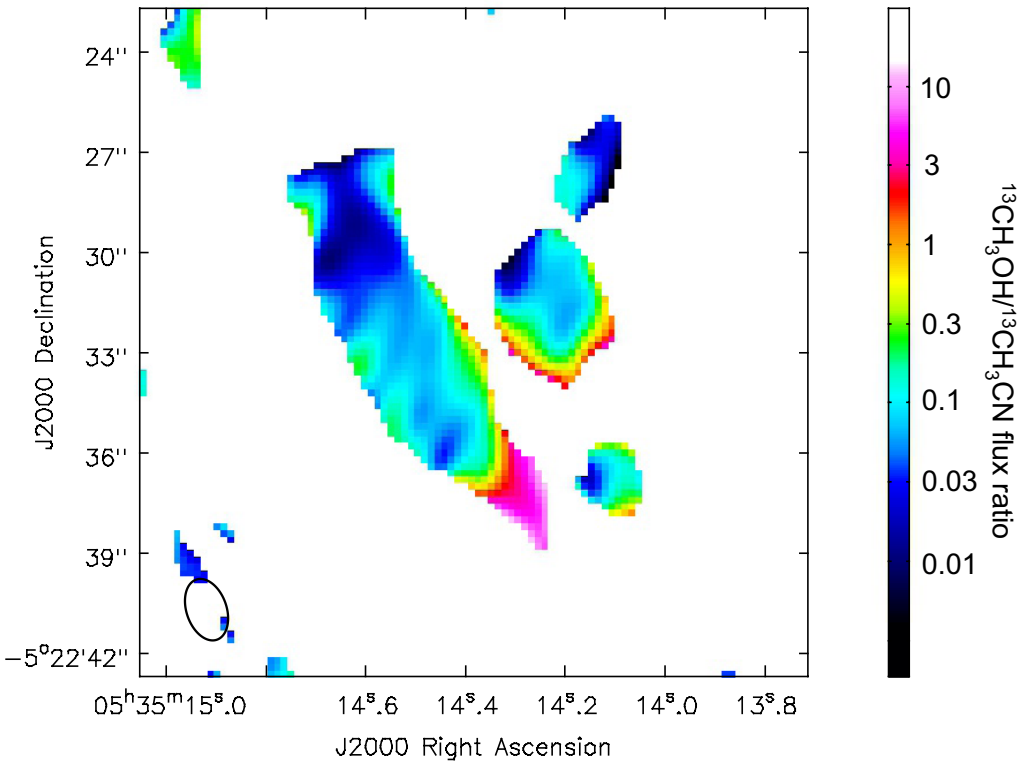

Figure 3.8: The integrated intensity ratio of the $^{13}CH_3OH$-E map to $^{13}CH_3CN$ given in Fig. 3.7 showing the increase in methanol emission relative to methyl cyanide from north to south. The synthesized beam size is indicated by an oval in the lower left corner of each panel.

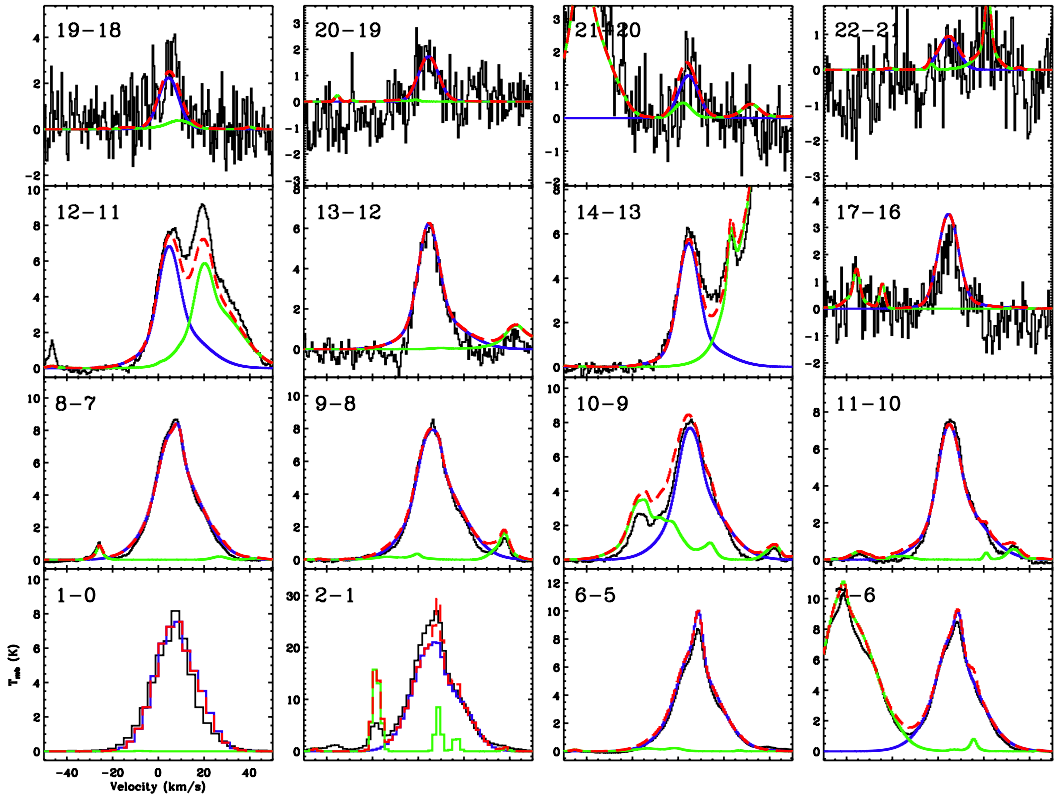

Figure 3.9: Individual lines of $H^{13}CN$ detected in the HIFI and IRAM surveys are plotted in each panel. The data are plotted in black, the $H^{13}CN$ model is overlaid in blue, emission from all other molecules is plotted in green, and the total model is overlaid as a red dashed line. Excitation energy increases from the lower left panel to the upper right and transitions are labeled in the upper left corner of each panel.

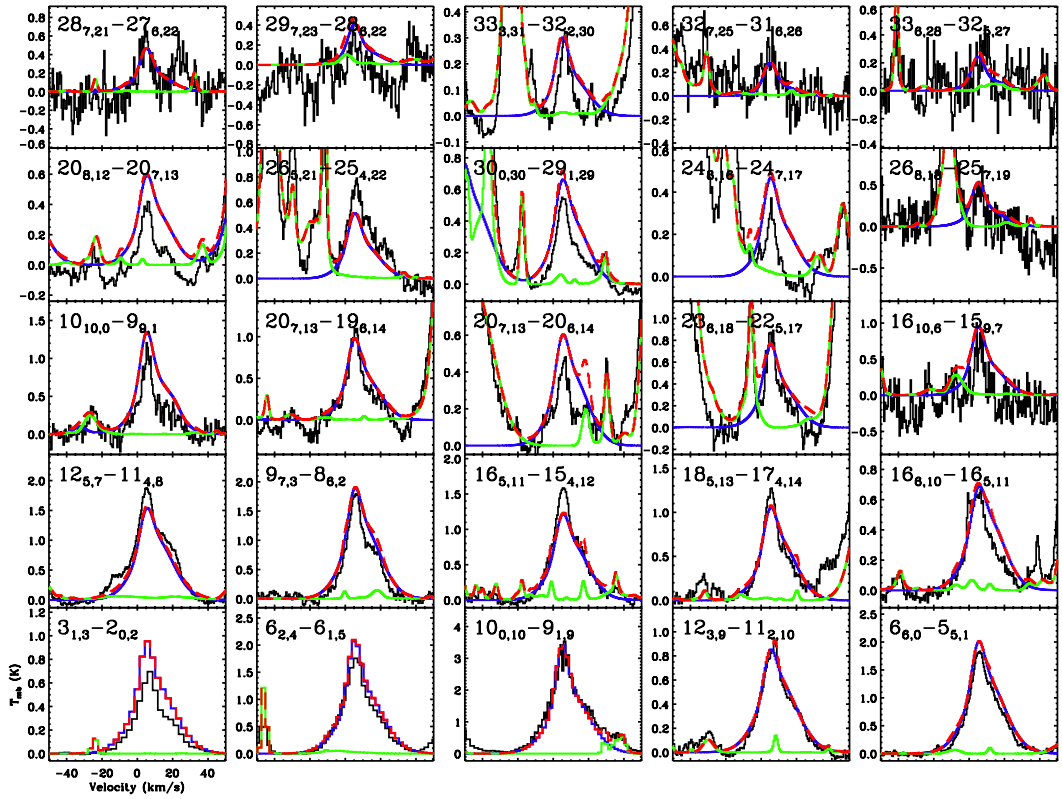

Figure 3.10: A sample of $^{34}SO_2$ lines detected in the HIFI and IRAM surveys. Conventions are the same as Fig. 3.9. Quantum numbers labeling each transition are $J_{Ka,Kc}$.

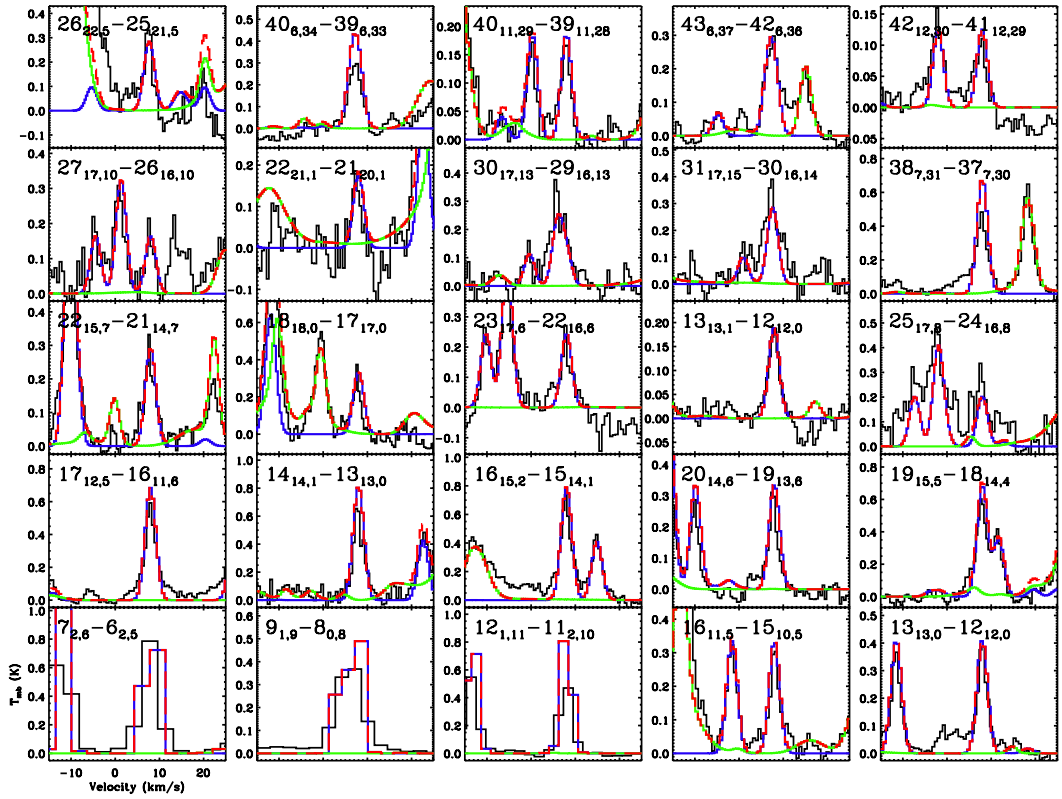

Figure 3.11: A sample of CH_3OCHO lines detected in the HIFI and IRAM surveys. Conventions are the same as Fig. 3.9. Because of the high line density of this molecule, multiple transitions often appear in the same panel. The central line is the one that corresponds to the label. Quantum numbers labeling each transition are $J_{Ka,Kc}$.

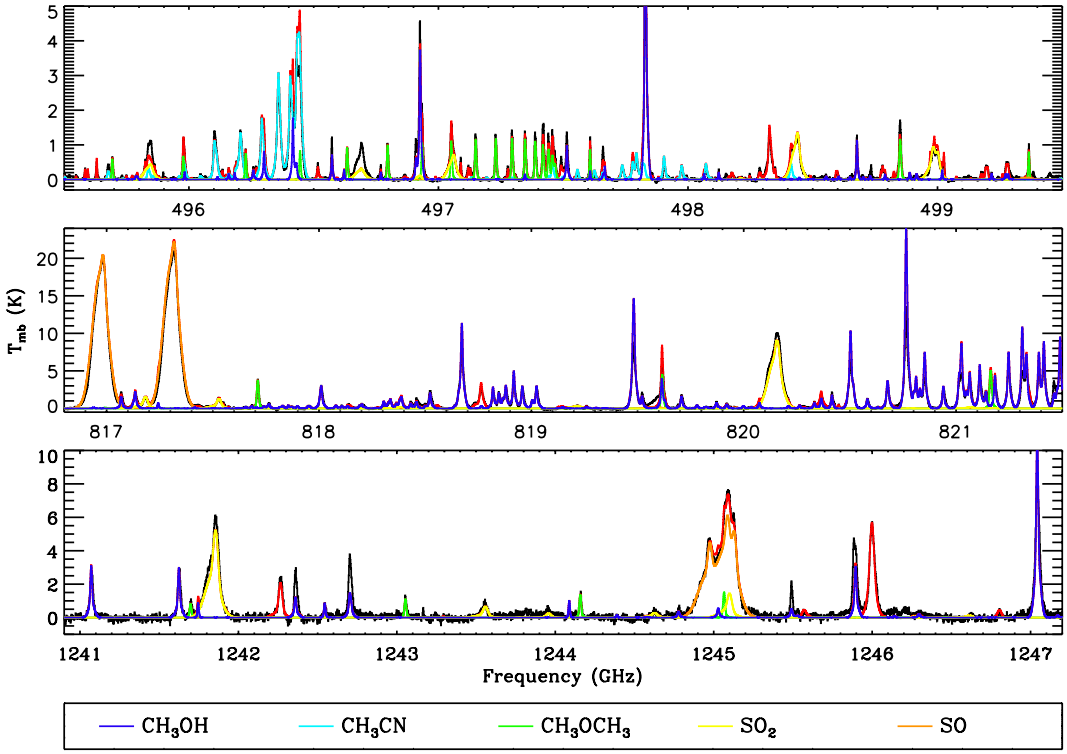

Figure 3.12: A spectral region from the HIFI survey is plotted in each panel. The data are plotted in black and the full band model is plotted in red. Individual molecular fits are overlaid as different colors. A legend is given at the bottom of the plot. The overlaid individual fits include emission from all detected isotopologues and vibrationally excited states for the labeled molecule.

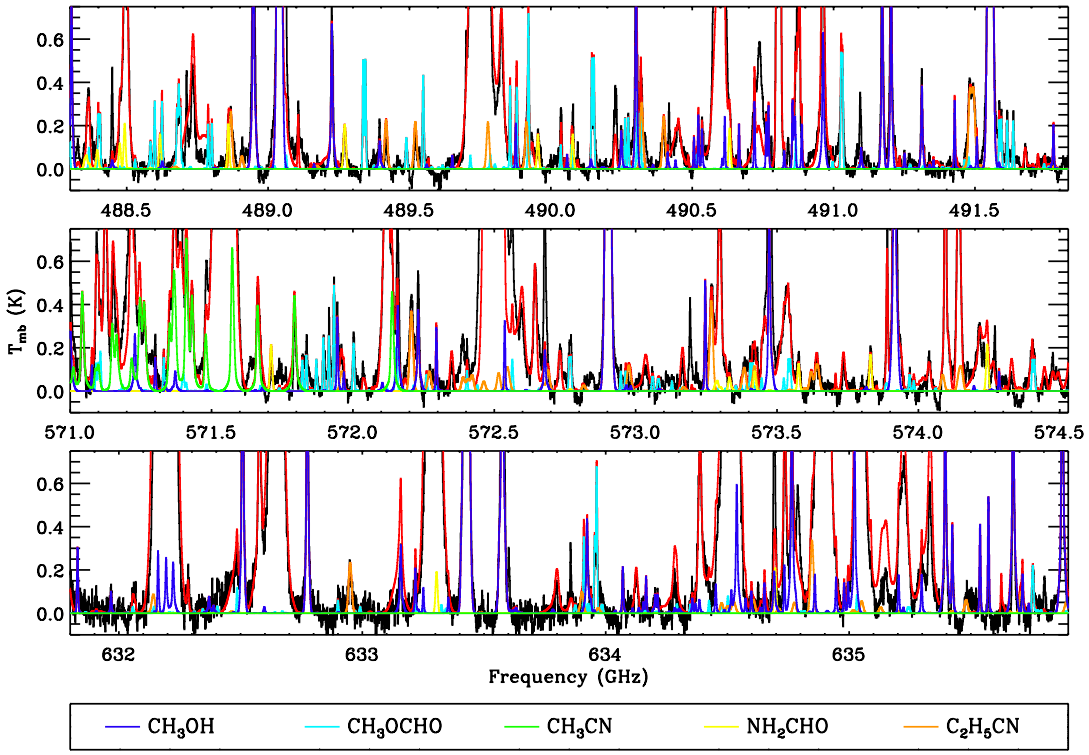

Figure 3.13: A spectral region from the HIFI survey is plotted in each panel. The same conventions as Fig. 3.12 are followed here. This figure, however, highlight weak emission ($T_{mb} < 1$ K) originating principally from complex organics.

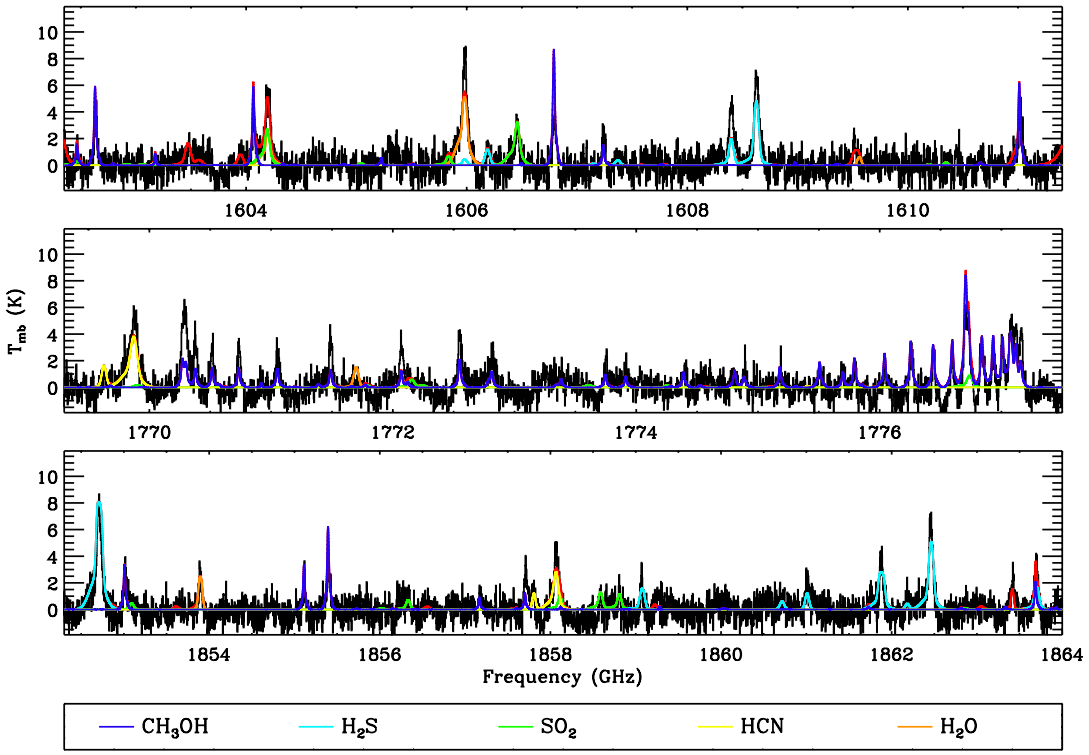

Figure 3.14: A spectral region from the HIFI survey is plotted in each panel. The same conventions as Fig. 3.12 are followed here. These regions are from bands 6 and 7.

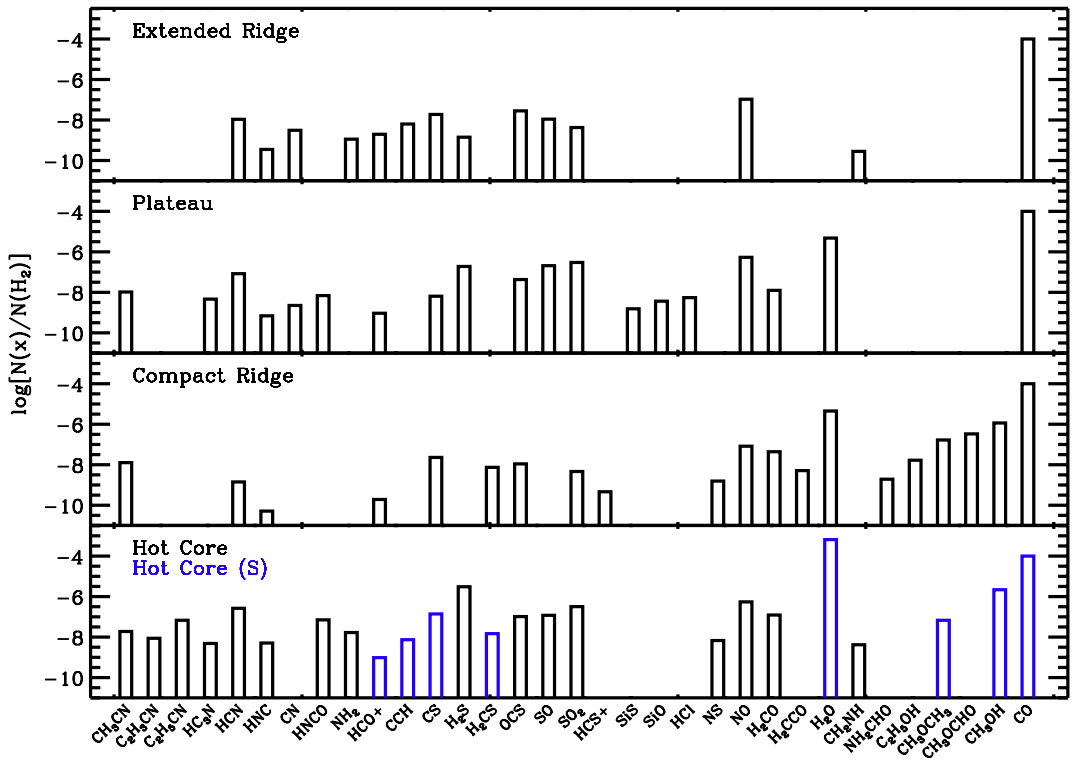

Figure 3.15: Derived abundances are plotted as a function of molecule. Each panel corresponds to a different spatial/velocity component which is labeled in the upper left hand corner of each panel. Abundances plotted in blue indicate an origin from hot core (s).

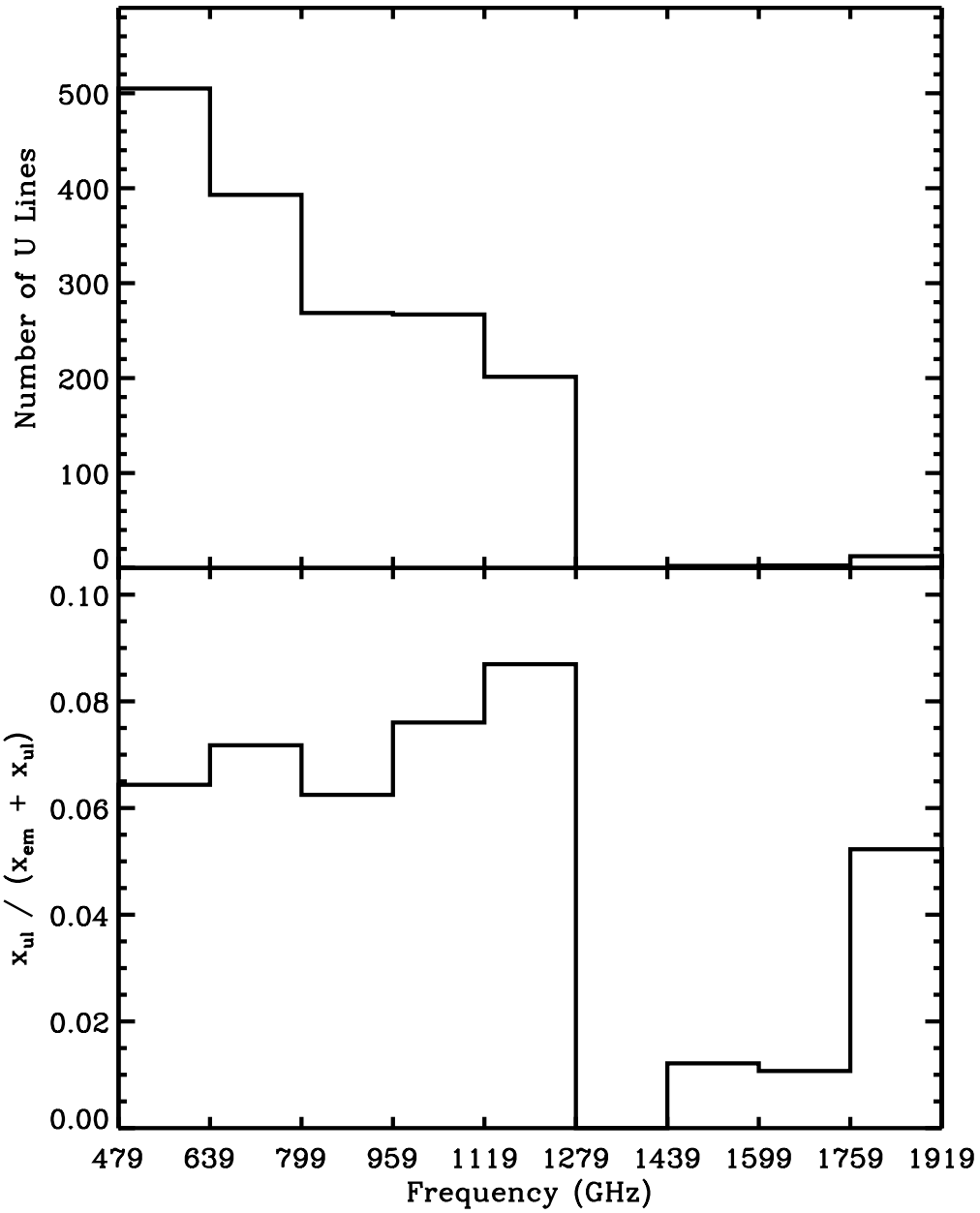

Figure 3.16: The top panel is a histogram of the number of U lines as a function of frequency. The lower panel plots the fraction of U line channels as a function of frequency.

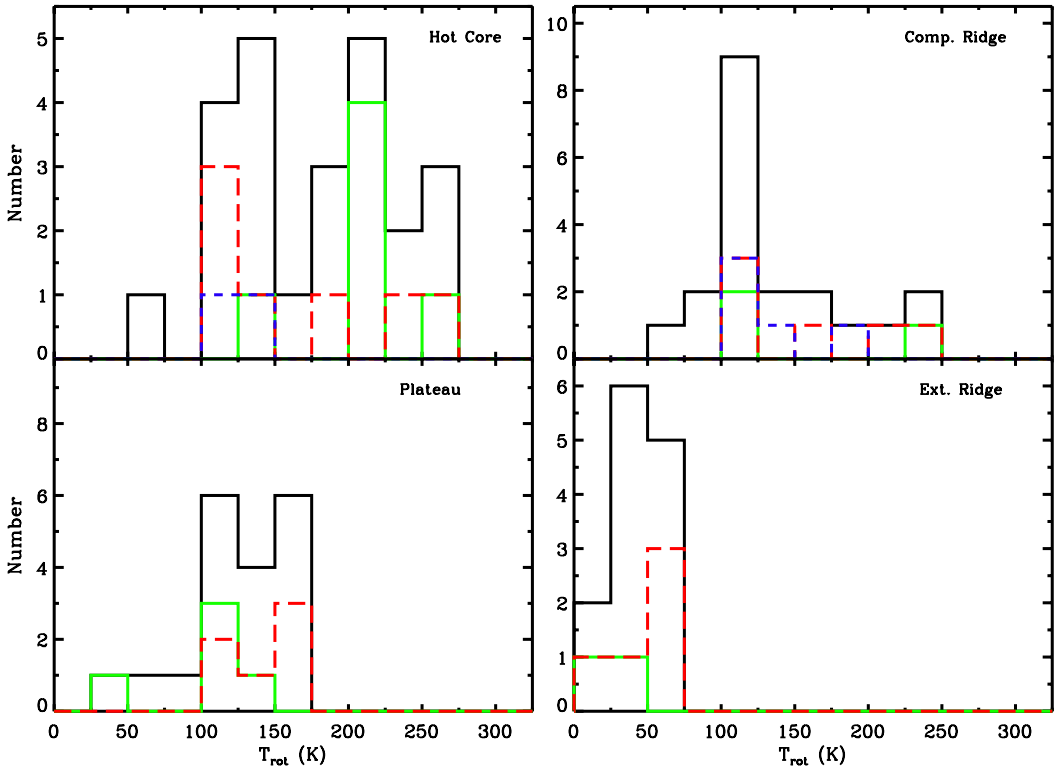

Figure 3.17: Rotation temperature histograms originating from the individual spatial/velocity components are plotted in different panels. Rotation temperatures from cyanides, sulfur bearing molecules, and complex oxygen bearing organics are plotted as solid green, dashed red, and dashed blue lines, respectively. T_{rot} values from all molecules are plotted as a black solid line.

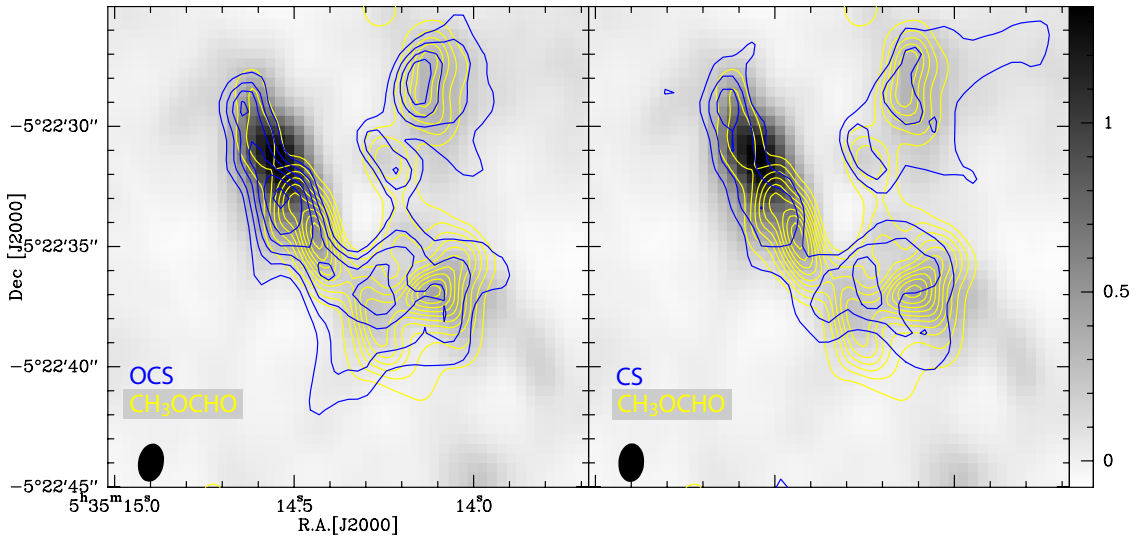

Figure 3.18: Integrated intensity maps of OCS 20 – 19 and CS 5 – 4 between v_{lsr} = 7.6 – 8.3 km/s are plotted as blue contours in the left and right panels, respectively. The first contour corresponds to 1.32 Jy beam^{-1} km s^{-1} and higher contours increase in steps of 1.28 Jy beam^{-1} km s^{-1}. The yellow contours in both panels correspond to a channel map of CH_3OCHO $18_{7,11}$ – $17_{7,10}$ at v_{lsr} = 7.8 km/s. The first contour is 337 mJy beam^{-1}, which is also the contour step. The 1 mm continuum in Jy beam^{-1} is overlaid as a greyscale.

CHAPTER 4

H_2S as a Probe of Dense Gas and Possibly Hidden Luminosity toward the Orion KL Hot Core

4.1 Introduction

The sub-mm and far-IR are fruitful parts of the electromagnetic spectrum to study light hydride molecules. Due to their low molecular weight, the rotation transitions of these species are more widely spaced and occur at higher frequencies than their more complex counterparts. Sub-mm and mm wave observations show that light hydrides (e.g. H_2O, NH_3, HCl, H_2S, etc...) are common in the interstellar medium (ISM; Phillips, 1987). However, the use of these molecules as physical probes has been hindered primarily by atmospheric absorption. Although many light hydrides have low lying rotation (or inversion) transitions at wavelengths that are accessible through open atmospheric windows, observations of higher energy lines occur at frequencies > 1 THz, where the atmosphere is completely opaque. As a result, unambiguous constraints on molecular emissions of many key light hydrides are rare. The HIFI instrument (de Graauw et al., 2010) on board the *Herschel* Space Observatory (Pilbratt et al., 2010), however, provides the first opportunity to access this part of the electromagnetic spectrum at high spectral resolution, making light hydrides available as physical probes of molecular gas.

In this study, we investigate and model the emission of H_2S toward the hot core within the Orion Kleinmann-Low nebula (Orion KL), the paradigmatic massive star forming region in our Galaxy. Historically H_2S has been used primarily as a probe of sulfur chemistry in the ISM. A number of studies have measured H_2S abundances toward a wide variety of environments including dark clouds (Minh et al., 1989),

low density molecular clouds (Tieftrunk et al., 1994), low mass protostars (Buckle & Fuller, 2003), hot cores (Hatchell et al., 1998; van der Tak et al., 2003; Herpin et al., 2009), and shocks (Minh et al., 1990, 1991). In this study, however, we explore the utility of H_2S more generally as a probe of the gas physical state. As a light hydride, H_2S has a high dipole moment (0.97 D) and widely spaced energy states. Furthermore, many transitions have critical densities in excess of 10^{7-8} cm^{-3}. Consequently, H_2S is very sensitive to both the gas temperature and density.

The data presented here were taken from the full *Herschel*/HIFI spectral scan of Orion KL obtained as part of the guaranteed time key program entitled *Herschel Observations of EXtra Ordinary Sources* (HEXOS). Because of the unprecedented frequency coverage provided by this dataset ($\sim$1.2 THz), we had access to over 90 transitions from $H_2{}^{32}S$ and its two rarer isotopologues $H_2{}^{33}S$ and $H_2{}^{34}S$ over an energy range of 55 – 1233 K, many of which can not be observed from the ground because they occur at frequencies higher than 1 THz. With this comprehensive dataset, we are able to explore the viability of this molecule as a probe of the gas physical state and set direct constraints on the abundance of H_2S toward the Orion hot core.

Although we seek only to model the H_2S hot core emission because it dominates the line profiles at high excitation energies, Orion KL harbors several other spatial/velocity components (Blake et al., 1987). Despite the fact that these components are not spatially resolved by *Herschel*, they have substantially different central velocities relative to the Local Standard of Rest, v_{lsr}, and full width at half maximum line widths, Δv. We can therefore differentiate these components using the spectral resolution of HIFI. These components include the already mentioned "hot core" (v_{lsr} = 3–5 km/s, Δv = 5–10 km/s); at least two outflow components often referred to as the "plateau" (v_{lsr} = 7–8 km/s, $\Delta v \gtrsim$20 km/s); a group of dense clumps adjacent to the hot core collectively known as the "compact ridge" (v_{lsr} = 7–9 km/s, Δv = 3–6 km/s); and widespread cool, quiescent gas referred to as the "extended ridge" ($v_{lsr} \sim 9$ km/s, $\Delta v \sim 4$ km/s).

In specifying these components, we note that recent studies have questioned the designation of the so called Orion "hot core" as a *bona fide* hot core. Zapata et al.

(2011), for example, conclude that the Orion hot core is actually externally heated by an "explosive event", possibly a stellar merger. In this scenario, the hot core was a relatively dense region within the extended ridge that has been further compressed by the flow of material produced by this event. Goddi et al. (2011), on the other hand, find that the heavily embedded object radio source I may be the primary heating source for the Orion hot core. They suggest that the combined effect of source I's proper motion and outflow could be mechanically heating the gas and dust. In order to be consistent with the literature, we refer to this region as the hot core, but recognize that this may, indeed, be a misnomer.

The structure of this chapter is as follows. We detail our observations and data reduction procedure in Sec. 4.2. In Sec. 4.3 we present the results from our rotation diagram and non-LTE analyses. We also compute an ortho/para ratio and a D/H ratio upper limit for H_2S. We discuss our results in Sec. 4.4, and summarize our conclusions in Sec. 4.5.

4.2 Observations and Data Reduction

The H_2S transitions are scattered throughout the full HIFI spectral scan of Orion KL. More details on the HEXOS key program as well as HIFI spectral scans in general are given in Bergin et al. (2010). A more comprehensive description of the data product is presented in Chapter 3. As part of a global analysis, Chapter 3 also presents a spectral model for each detected molecule in the Orion KL HIFI survey assuming local thermodynamic equilibrium (LTE). The sum of all of these fits yields the total modeled molecular emission, which we refer to, in this study, as the "full band model". We, however, briefly describe the entire dataset here and outline the data reduction process. Most of the observations were obtained in March and April 2010, with the exceptions of bands 3a and 5b, which were obtained 9 September 2010 and 19 March 2011, respectively. The full dataset covers a significant bandwidth of approximately 1.2 THz in the frequency range 480–1900 GHz, with gaps between 1280–1430 GHz and 1540–1570 GHz. The data have a spectral resolution of 1.1 MHz corresponding to 0.2 – 0.7 km/s across the band. The spectral scans for each band were taken in dual

beam switch (DBS) mode, the reference beams lying 3′ east or west of the target, using the wide band spectrometer (WBS) with a redundancy of 6 or 4 for bands 1–5 and 6–7, respectively – see Bergin et al. (2010) for a definition of redundancy. For bands 1–5, the telescope was pointed toward coordinates $\alpha_{J2000} = 5^h35^m14.3^s$ and $\delta_{J2000} = -5°22'33.7''$, midway between the Orion hot core and compact ridge. For bands 6–7, where the beam size is smaller, the telescope was pointed directly toward the hot core at coordinates $\alpha_{J2000} = 5^h35^m14.5^s$ and $\delta_{J2000} = -5°22'30.9''$. We assume the nominal absolute pointing error (APE) for *Herschel* of 2.0″ (Pilbratt et al., 2010).

The data were reduced using the standard HIPE (Ott, 2010) pipeline version 5.0 (CIB 1648) for both the horizontal, H, and vertical, V, polarizations. Level 2 double sideband (DSB) scans, the final product of pipeline reduction, required additional processing before they could be deconvolved to a single sideband (SSB) spectrum. First, each DSB scan was inspected for spurious spectral features ("spurs") not identified by the pipeline. Once identified, these features were flagged by hand such that they would be ignored by the deconvolution routine. Baselines were also removed from the DSB scans using the FitBaseline task within HIPE by fitting polynomials to line free regions. In most instances we required a constant or first order polynomial; however, second order polynomials were used in some cases.

Once the baselines were removed, we deconvolved the DSB scans to produce an SSB spectrum for each band. The deconvolution was performed using the *doDeconvolution* task within HIPE. We did not apply a gain correction or use channel weighting. The deconvolution was done in three stages. First, the data were deconvolved with the strongest lines ($T_A^* > 10$ K) removed. This reduced the probability of strong ghost lines appearing in the SSB spectrum (see e.g. Comito & Schilke, 2002) but resulted in channel values of zero at strong line frequencies in the SSB spectrum. Second, we performed another deconvolution with the strongest lines present to recover the data at strong line frequencies. And third, the strong lines were incorporated into the the weak line deconvolution by replacing the zero value channels with the strong line deconvolution.

The SSB spectra were exported from HIPE to FITS format using *HiClass*. These files were then imported to CLASS (Continuum and Line Analysis Single-dish Software) and converted to CLASS format. All subsequent data reduction procedures were performed using this program. The H and V polarizations were averaged together and aperture efficiency corrections were applied using Eq. 1 and 2 from Roelfsema et al. (2012) with the reference wavelength equal to the central wavelength of each band. For bands 1–5, we use the aperture efficiency correction, which is more coupled to a point source, because the *Herschel* beam size is large relative to the size of the hot core ($\sim$ 3–10$''$). For bands 6–7, on the other hand, we use the main beam efficiency, because it is more coupled to an extended source. For simplicity, however, we will refer to line intensities as main beam temperatures, T_{mb}, regardless of the band in which a line falls. The H/V averaged, efficiency corrected, SSB spectra represent the final product of our data reduction procedure.

4.3 Results

4.3.1 Measuring Line Intensities

We identify 70 transitions of $H_2{}^{32}S$, the main isotopologue of H_2S, spanning a range in upper state energy, E_{up}, of 55–1233 K. We also detect emission from the two rarer isotopologues $H_2{}^{34}S$ and $H_2{}^{33}S$, the former being more abundant than the latter. From these rarer species, we identify 44 and 21 transitions of $H_2{}^{34}S$ and $H_2{}^{33}S$ spanning ranges in E_{up} of 55–700 K and 55–328 K, respectively. Fig. 4.1 plots a sample of nine $H_2{}^{32}S$ transitions over the full energy range over which emission is detected. Each panel plots a different transition, labeled in the upper left hand corner, with E_{up} (also labeled) increasing from upper left to lower right. From the figure, we see that the most highly excited lines ($E_{up} \gtrsim 700$ K) are simple and consistent with emission from the hot core. At lower excitation, however, the line profiles become more complex indicating emission from additional components. The wide component ($\Delta v \sim 30$ km/s) clearly originates from the plateau, while the narrow component ($\Delta v \sim 3$ km/s) is consistent with either the extended or compact ridge.

Fig. 4.1 also overlays Gaussian fits to each component, from which we obtain the v_{lsr}, Δv, peak line intensity, T_{peak}, and integrated intensity, $\int T_{mb} dv$, for each spatial/velocity component. We used CLASS to fit the observed line profiles after uniformly smoothing the data to ∼0.5 km/s, in order to increase the S/N, and fitting a local baseline. This was a relatively straightforward process at high energies because the hot core was the only emissive component. At lower energies, however, where multiple components were visible, different combinations of Gaussians could reproduce the observed profiles. In most instances, we allowed all of the parameters to vary during the fitting process. Although, care was taken to make sure that the Gaussian fits conformed to canonical values for v_{lsr} and Δv typical of the hot core, plateau, and extended ridge. In rare cases, allowing all of the parameters to vary resulted in fits not in line with these known spatial/velocity components and the v_{lsr} was held fixed to ensure a reasonable fit.

Because Orion KL is an extremely line rich source in the sub-mm, a fraction of the potentially detected lines had to be excluded from our analysis due to strong line blends from other molecules. Blended H_2S lines were identified by overlaying the full band model, which includes emission from all other identified species in the Orion KL HIFI scan (Chapter 3), to those spectral regions where we observe H_2S emission. We split the observed lines into three categories: (1) lines that were not blended or any blending line predicted by the full band model had a peak flux $\lesssim 10\%$ that of H_2S, (2) lines that were blended but could be separated by Gaussian fitting, and (3) heavily blended lines from which reliable Gaussian fits could not be derived. We emphasize that these categories were determined by eye. We only include transitions from categories 1 and 2 in our analysis which amount to 52, 24, and 8 transitions from $H_2{}^{32}S$, $H_2{}^{34}S$, and $H_2{}^{33}S$, respectively. We report the results of our Gaussian fits for the hot core, plateau, and extended/compact ridge in Tables 4.1, 4.2, and 4.3, respectively for categories 1 and 2 defined above. As stated in Sec. 4.1, we seek only to investigate the hot core emission in this work, but we include our measurements for the extended ridge and plateau here for completeness. Instances when the v_{lsr} was held fixed for a particular component during Gaussian fitting are indicated in

Tables 4.1 – 4.3.

Fig. 4.2 is an energy level diagram for $H_2{}^{32}S$. The lines connecting the levels are black, blue, or red corresponding, respectively, to categories 1, 2, and 3. The red transitions, therefore, are detected but do not provide any useful information for the present study because these lines are so blended that a reliable Gaussian fit could not be derived. Examination of this diagram reveals two things. First, that in spite of the prevalence of blending, we still are able to extract useful flux information over the energy range that H_2S emission is detected. And second, that our primary probe of H_2S for $E_{up} \gtrsim 350$ K are the $\Delta J = 0$, $\Delta K_{\pm} = \pm 1$ transitions, and for $E_{up} \lesssim 350$ K we become sensitive to $\Delta J = \pm 1$ lines. Here, J is the quantum number corresponding to the total rotational angular momentum of H_2S, while K_+ and K_- are the quantum numbers that would correspond to the angular momentum along the axis of symmetry in the limit of an oblate or prolate symmetric top, respectively. Unfortunately, we do not detect many of the J = 9 para transitions because they either occur in HIFI frequency coverage gaps or regions of high noise.

4.3.2 Measuring Upper State Column Densities

As a consequence of HIFI's wide frequency coverage, we directly measure H_2S upper state column densities, N_{up}, for a large fraction of the available states. For more detailed derivations of the equations that follow and discussions of their utility in the analysis of molecular spectroscopic data see e.g. Goldsmith & Langer (1999) and Persson et al. (2007). The analysis below requires the use of known isotopic ratios. We have carried out these calculations assuming two different sets of ratios. The first assumes solar values, $^{32}S/^{34}S = 22$ and $^{32}S/^{33}S = 125$ (Asplund et al., 2009), and the second were measured directly toward Orion KL, $^{32}S/^{34}S = 20$ and $^{32}S/^{33}S = 75$ (Tercero et al., 2010). The text that follows refers to these sets of values as "Solar" and "Orion KL" isotopic ratios, respectively.

In instances where the main isotopologue, $H_2{}^{32}S$, is optically thick but we observe the same transition with $H_2{}^{34}S$ or $H_2{}^{33}S$, we compute the upper state column by explicitly calculating an optical depth. The optical depth can be estimated as-

suming that the excitation temperature is the same for both isotopologues and that $\tau_{main} \gg \tau_{iso}$, where τ_{main} is the optical depth of the $H_2{}^{32}S$ line and τ_{iso} is the optical depth of the $H_2{}^{33}S$ or $H_2{}^{34}S$ line. With these assumptions we can write the following relation,

$$\tau_{iso} = -ln\left(1 - \frac{T_{iso}}{T_{main}}\right) \tag{4.1}$$

where T_{main} and T_{iso} are the peak line intensities for the main and rarer isotopologue, respectively. The $H_2{}^{32}S$ optical depth can then be computed using,

$$\tau_{main} = \tau_{iso}\left(\frac{^{32}S}{^{iso}S}\right). \tag{4.2}$$

The upper state column can then be computed using the relation,

$$N_u\left(H_2^{32}S\right) = \frac{8\pi k\nu^2}{hc^3 A_{ul}} \frac{\int T_{mb} d\mathrm{v}}{\eta_{bf}} \left(\frac{\tau_{main}}{1 - e^{-\tau_{main}}}\right) e^{\tau_d(\nu)} \tag{4.3}$$

where ν is the rest frequency of the transition, $\int T_{\rm mb} d\mathrm{v}$ is the integrated intensity of the line in velocity space, η_{bf} is the beam filling factor, $^{32}S/^{iso}S$ is the appropriate isotopic ratio, $\tau_{\rm d}(\nu)$ is the dust optical depth, A_{ul} is the Einstein coefficient for spontaneous emission, h is Planck's constant, k is Boltzmann's constant, and c is the speed of light. In Eq. 4.3, the beam filling factor is given by the usual expression assuming a gaussian profile for both the telescope beam and source,

$$\eta_{bf} = \frac{\theta_s^2}{\theta_s^2 + \theta_b^2} \tag{4.4}$$

where θ_s is the source size and θ_b is the telescope beam size.

We calculated the dust optical depth using the same power law assumed in Chapters 1 and 3,

$$\tau_d(\nu) = 2\mathrm{m_H}(\chi_{\rm dust})\mathrm{N_{H_2}}\kappa_{1.3\rm mm}\left(\frac{\nu}{230\ \mathrm{GHz}}\right)^{\beta} \tag{4.5}$$

where $\mathrm{m_H}$ is the mass of a hydrogen atom, $\chi_{\rm dust}$ is the dust to gas mass ratio, $\mathrm{N_{H_2}}$ is the column density of H_2 molecules, $\kappa_{1.3\rm mm}$ is the dust opacity at 1.3 mm (230 GHz), and β is the dust spectral index. We assume $\kappa_{1.3\rm mm} = 0.42$ cm^2 g^{-1}, midway be-

tween MRN and MRN with thin ice mantels (Ossenkopf & Henning, 1994), $\beta = 2$, and $\chi_{\rm dust} = 0.01$, consistent with Chapter 3. We also adopt the same N_{H_2} estimate derived in Chapter 3, 2.5×10^{24} cm^{-2}, used to compute $\tau_{\rm d}(\nu)$ toward the hot core. This N_{H_2} estimate is 8 times larger than that reported in Plume et al. (2012, $N_{H_2} = 3.1 \times 10^{23}$ cm^{-2}), which is derived from C^{18}O line observations from the HIFI spectral survey, but is more consistent with N_{H_2} measurements based on mm and sub-mm dust continuum observations (Favre et al., 2011; Mundy et al., 1986; Genzel & Stutzki, 1989), which report $N_{H_2} \gtrsim 10^{24}$ cm^{-2}. Because H_2S transitions are detected throughout the entire HIFI spectrum, $\tau_{\rm d}(\nu)$ varies approximately between 0.2 ($\nu \approx 488$ GHz) and 2.4 ($\nu \approx 1900$ GHz). When estimating an uncertainty for $\tau_{\rm d}(\nu)$, we assume a 30% error for N_{H_2}. The H_2 column density reported in Plume et al. (2012) thus lies within 3 σ of the value used in Eq. 4.5.

To compute upper state column densities, we need an estimate of the source size, which can be obtained from the extremely optically thick $H_2{}^{32}S$ lines. In the optically thick limit, the observed peak intensity of a spectral line becomes the product of the beam filling factor and the source function $J(T_{ex})$ attenuated by the dust optical depth,

$$T_{mb} = \eta_{bf} J(T_{ex}) e^{-\tau_d(\nu)}, \tag{4.6}$$

where the above expression assumes $T_{\rm ex}$ is much greater than the background temperature. Because we do not satisfy the condition $h\nu \ll kT_{ex}$ at THz frequencies, the approximation $J(T_{ex}) \approx T_{ex}$ is not valid. We must, therefore, substitute the full expression for the source function. Doing this and solving for T_{ex} we get the following expression,

$$T_{ex} = \frac{h\nu}{k} \left[ln \left(\frac{h\nu}{k} \frac{\eta_{bf}\ e^{-\tau_d(\nu)}}{T_{mb}} + 1 \right) \right]^{-1}. \tag{4.7}$$

We are thus able to estimate the source size by varying it in Eq. 4.7 until $T_{\rm ex}$ is commensurate with what we expect from the Orion hot core.

We compute a mean $T_{\rm ex}$ for all $H_2{}^{32}S$ transitions with $E_{\rm up} < 200$ K (10 lines). In addition to being the most optically thick lines in our dataset, these transitions have $A_{ul} \sim 10^{-3}$ s^{-1} and collision rates of order 10^{-11} cm^{-3}s^{-1}, yielding critical densities

$\sim 10^8$ cm^{-3}. The density of the hot core is typically estimated to be $\gtrsim 10^7$ cm^{-3} (Genzel & Stutzki, 1989) and our own non-LTE analysis of the more optically thin H_2S isotopologues (Sec. 4.3.5) requires densities $\gtrsim 10^8$ cm^{-3} in order to reproduce the observed emission. Thus, the lowest energy H_2S transitions should have level populations close to or in LTE, depending on the actual density of the H_2S emitting gas. Consequently, computed values of T_{ex} for these transitions should be commensurate with the kinetic temperature of the gas in the hot core. Kinetic temperatures toward this region have been measured previously using NH_3 inversion transitions, which have LTE level populations at hot core densities. Using states with $E_{up} \lesssim 1200$ K, previous studies have derived kinetic temperatures of $\sim$160 K toward the hot core (Hermsen et al., 1988; Wilson et al., 2000). We note that Goddi et al. (2011) derived kinetic temperatures as high as 490 K in the hot core using NH_3 inversion lines. This study, however, used transitions with $E_{up} \approx 400 - 1500$ K and is likely sensitive to hotter gas than is predominately probed by lower energy lines. For θ_s values in the range $4 - 8''$, we derive a range in mean T_{ex} of 300 – 101 K. Source sizes much smaller than $4''$ result in unreasonably high values for T_{ex}, while sizes larger than $8''$ yield T_{ex} estimates lower than 100 K indicating that the low energy H_2S transitions are out of LTE. We therefore adopt an intermediate value of $6''$, corresponding to $T_{ex} = 153$ K, with an estimated uncertainty of $\pm$ $0.7''$ ($3\ \sigma$ thus encompasses the above range in θ_s).

Table 4.4 lists values for τ_{iso} and $N_{up}(H_2{}^{32}S)$ for transitions where the optical depth could be explicitly computed and assumes a source size of $6''$. The table lists $N_{up}(H_2{}^{32}S)$ values assuming both Solar and Orion KL isotopic ratios. Examining Table 4.4, one sees that in instances when the same transition is observed by $H_2{}^{33}S$ and $H_2{}^{34}S$ (i.e. $4_{2,3}$–$4_{1,4}$, $4_{2,3}$–$3_{1,2}$, and $4_{4,1}$–$4_{3,2}$), the Orion KL ratios yield upper state columns that are in better agreement with one another. Consequently, we take the isotopic ratios derived by Tercero et al. (2010) to be more compatible with the observed emission, indicating that the $^{32}S/^{33}S$ ratio is $\sim$1.7 times smaller than Solar toward the Orion KL hot core. We note that for three transitions ($2_{1,2}$–$1_{0,1}$, $2_{2,1}$–$1_{1,0}$, and $3_{3,0}$–$2_{2,1}$) computing values for $H_2{}^{34}S/H_2{}^{32}S$ in order to obtain τ_{iso} resulted

in ratios > 1 (i.e. the $H_2{}^{34}S$ line is stronger than the corresponding $H_2{}^{32}S$ line). The likely explanation is that the $H_2{}^{34}S$ lines are still quite optically thick at low excitation. As a result, estimates of τ_{iso} and N_{up} based on $H_2{}^{34}S/H_2{}^{32}S$ line ratios may be underestimated particularly at low excitation energies. Fortunately, several low energy states are also probed by the more optically thin $H_2{}^{33}S$ isotopologue.

4.3.3 Rotation Diagram Analysis

We use the upper state column densities given in Table 4.4 to construct rotation diagrams for ortho (upper panel) and para (lower panel) H_2S in Fig. 4.3 assuming Orion KL isotopic ratios. Points were placed on the diagrams by dividing N_{up} for each state by the statistical weight, g_u. States with multiple N_{up} measurements were averaged together and the uncertainty was propagated by adding the individual errors in quadrature and dividing by the number of measurements. These values were then plotted as a function of energy in units of Kelvin. From these plots, a "rotation temperature", T_{rot}, and total $H_2{}^{32}S$ column density, N_{tot}, can be derived by performing a linear least squares fit to the points using the following relations,

$$T_{rot} = \frac{1}{m} \qquad N_{tot} = Q(T)e^b \tag{4.8}$$

where m and b are the slope and y intercept of the linear least squares fit, respectively, and Q(T) is the partition function. In the LTE limit, the points should follow a line and T_{rot} will equal the kinetic temperature.

From the figure, we immediately see that the points follow a straight line for both ortho and para H_2S, given the uncertainties, over the range in E_{up} where N_{up} values could be computed. If H_2S is indeed in LTE, the lack of curvature in these diagrams indicates that there is not a strong temperature gradient in the H_2S emitting gas. Another possibility, however, is that a strong far-IR continuum redistributes the population, particularly at higher energies, to produce the observed rotation diagrams. We investigate this possibility in Sec. 4.3.5. Weighted linear least squares fits to the points are straightforward to compute. Fitting the ortho diagram yields

$T_{rot} = 141 \pm 12$ K and N_{tot}(o-$H_2{}^{32}S$) $= 5.9 \pm 1.3 \times 10^{17}$ cm^{-2}, while the para diagram gives $T_{rot} = 133 \pm 15$ K and N_{tot}(p-$H_2{}^{32}S$) $= 2.7 \pm 0.7 \times 10^{17}$ cm^{-2}. The derived values for T_{rot}, thus, agree to within 1 σ. We, however, take the ortho rotation temperature as more reliable because upper state column densities are measured over a larger range in E_{up} for ortho H_2S. Because ortho and para H_2S should, in principle, have the same temperature, we fit the para H_2S rotation diagram again with T_{rot} fixed to a value of 141 K. Because the rotation temperatures for ortho and para H_2S are in close agreement with one another, N_{tot}(p-$H_2{}^{32}S$) shifts to a value of $2.4 \pm 0.6 \times 10^{17}$ cm^{-2}, well within 1 σ of the previous value. Adding N_{tot}(o-$H_2{}^{32}S$) and N_{tot}(p-$H_2{}^{32}S$) gives a total $H_2{}^{32}S$ column density of $8.3 \pm 1.4 \times 10^{17}$ cm^{-2}.

We emphasize that our derived values for T_{rot} and N_{tot} assume $\theta_s = 6''$ and note that our T_{rot} estimate agrees well with the mean T_{ex} we calculated in Sec. 4.3.2 for this source size. Increasing or decreasing θ_s results in a decreasing or increasing N_{up} estimate, respectively, for any given state. The magnitude of this shift depends on the change in source size and the frequency of the transition due to the dependance of telescope beam size on frequency. Because E_{up} is not a strong function of frequency, the net effect of changing the source size on the rotation diagram is a net shift toward higher or lower values for N_{tot}, with some change in the scatter. Thus, the assumed source size influences N_{tot} but has little affect on T_{rot}. If, however, the highly excited H_2S emitting gas is significantly more compact than gas traced by low energy lines, the derived values for N_{up} will be shifted up more for higher energies compared to lower ones, resulting in a hotter T_{rot}. The extent to which this is true can only be determined by interferometric maps of H_2S, which do not currently exist.

4.3.4 Ortho/Para Ratio of H_2S

We are able to estimate the ortho/para ratio of H_2S in two ways. The first method is simply dividing our measurements for N_{tot}(o-$H_2{}^{32}S$) and N_{tot}(p-$H_2{}^{32}S$) given in Sec. 4.3.3, which yields 2.5 ± 0.8 and, of course, assumes LTE and a rotation temperature of 141 K. The second method, which does not assume LTE and is temperature independent, uses the upper state column densities derived in Table 4.4 directly. In

three instances, we measured N_{up} for ortho and para states with approximately equal upper state energies. The N_{up} ratio between such a pair of states should then reflect the global ortho/para ratio. Table 4.5 gives ortho/para ratio estimates in the instances where this is possible using the Orion KL isotopic ratios. Based on Table 4.5, we compute a mean ortho/para ratio of 1.7 ± 0.8. Both methods, therefore, point to an H_2S ortho/para ratio smaller than 3, the expected value in thermal equilibrium, but are not statistically different from the equilibrium value at the 3 σ level.

4.3.5 Non-LTE Analysis

We modeled the observed emission using RADEX (van der Tak et al., 2007), which is a non-LTE code that explicitly solves the equations of statistical equilibrium. RADEX employs the escape probability method to decouple the radiative transfer and statistical equilibrium equations from one another. Because the H_2S lines have observed widths that far exceed the expected thermal width at typical hot core temperatures (e.g. $\sim$0.5 km/s at $T_{kin} \sim 150$ K), we infer that turbulent motions are significant. We therefore use the large velocity gradient (LVG) approximation when running RADEX to model the H_2S emission toward the hot core.

We had to estimate collision rates for H_2 + H_2S because they have not been measured in the laboratory. We do this in two ways. In the first method, neutral-impact collision rates are scaled in proportion to radiative line strengths so that the sum of all downward rates from each upper state is equal to the base rate of 1.35×10^{-11} cm^3 s^{-1}. This base rate value was determined from measured depopulation cross sections reported by Ball et al. (1999) for the $1_{1,0}$–$1_{0,1}$ transition for He + H_2S collisions interpolated at 10 K and scaled to the reduced mass of the H_2 + H_2S system. In the second method, we estimate collision rates by scaling existing H_2O rates from Faure et al. (2007) by a constant factor of 0.4. These rates separate collisions with ortho and para-H_2. Consequently, we assume that the H_2 populations are thermalized at the kinetic temperature. The ortho/para ratio of H_2

is thus governed by the expression,

$$\frac{o-H_2}{p-H_2} = 9e^{-170.5/T_{kin}}. \tag{4.9}$$

We will refer to the collision rates estimated using the first and second methods described above as CR1 and CR2 rates, respectively, in the text that follows. The CR2 rates, (specifically ortho-H_2, the dominant form of molecular hydrogen at hot core temperatures), are larger than the CR1 rates by a factor of $\gtrsim 2$. As a result, higher densities are required when using the CR1 rates to achieve the same level of excitation as the CR2 rates. The CR2 rates, however, have a disadvantage in that collision rates for the most highly excited lines in our dataset are not computed.

We also include a model continuum to investigate if radiation plays a significant role in the excitation of H_2S. The continuum model is based directly on observed fluxes of IRc2, the brightest "IR clump" for $\lambda \lesssim 10$ μm and also spatially close to the position of the Orion KL hot core (see e.g. De Buizer et al., 2012; Okumura et al., 2011; Greenhill et al., 2004a; Gezari et al., 1998). Our model continuum is plotted in Fig. 4.4. The observations used to construct the diagram were obtained from a variety of sources (van Dishoeck et al., 1998; Lerate et al., 2006; Lonsdale et al., 1982; Dicker et al., 2009). The shape and color of each point indicates the reference from which it was obtained. We also measured the continuum at several frequencies throughout the HIFI scan, which are plotted as red triangles. When comparing the HIFI measurements to those obtained with LWS on board ISO (blue circles), we noticed that the continuum level as measured by HIFI was higher by approximately a factor of 4 at frequencies where the two observations overlapped. This difference is likely the result of ISO's larger beam size relative to *Herschel*. Because our aim is to construct a continuum model that best describes the radiation environment of H_2S as observed by HIFI, we normalized the ISO LWS and SWS continuum observations (blue circles and squares) so that the LWS continuum matched that of HIFI at $\sim$158 μm. The normalized values are given as black circles and squares, and our final continuum model is plotted as a black dashed line. We also overlay a 65 K blackbody

in Fig. 4.4 (green, dotted line) normalized to the SWS observations at ∼44 μm, which reproduces much of the observed flux in the mid/far-IR and sub-mm.

Given a radiation field, the input parameters to the RADEX model are the kinetic temperature, T_{kin}, H_2 number density, n_{H_2}, and total H_2S column density, N_{tot}. We can limit the parameter space of N_{tot} using a method originally described by Goldsmith et al. (1997) and more recently employed by Plume et al. (2012) to compute column densities for $C^{18}O$ toward different Orion KL spatial/velocity components using the same dataset presented here. Simply put, this method allows us to compute $N_{tot}(H_2{}^{32}S)$ by summing the N_{up} measurements probed by our data (i.e. Table 4.4) and deriving a correction factor to account for the column that is not measured. States with more than one measurement for N_{up} were averaged together in the same way as described in Sec. 4.3.3 assuming Orion KL isotopic ratios. Correction factors were computed by running RADEX models over the temperature range 25 – 400 K for H_2 densities of 10^7, 10^8, and 10^9 cm^{-3}, i.e. physical conditions expected within the hot core. All models assume a column density of 5×10^{16} cm^{-2} to avoid any problems with convergence associated with very optically thick low energy lines. A correction factor, CF, was then derived for each run of the model such that,

$$CF = \frac{N'_{tot}}{N'_{obs}} \tag{4.10}$$

where N'_{tot} is the total column density used in the RADEX model (5×10^{16} cm^{-2}) and N'_{obs} is the total column probed by HIFI as predicted by RADEX, i.e. the sum of N_{up} predictions for states listed in Table 4.4. Multiplying a given correction factor by N_{obs}, the observed sum of $N_{up}(H_2{}^{32}S)$ measurements listed in Table 4.4 ($3.1 \pm 0.4 \times 10^{17}$ cm^{-2} assuming Orion KL isotopic ratios), will thus give a measurement of $N_{tot}(H_2{}^{32}S)$.

Fig. 4.5 plots values for CF as a function of temperature using both CR1 (black) and CR2 (red) collision rates. Because the CR1 rates are smaller than those corresponding to CR2, we find that the correction factor curve for $n_{H_2} = 10^7$ cm^{-3} using CR1 values is significantly higher than the others. The reason is that using these

rates, a density of $n_{H_2} = 10^7$ cm^{-3} is not high enough, even at high temperatures, to excite a significant fraction of the H_2S population above the J=1 states, which are not probed by the HIFI scan. Conversely, the $n_{H_2} = 10^9$ cm^{-3} correction factors using CR2 rates increases more steeply as a function of temperature relative to the other curves. This behavior is seen because the gas is sufficiently dense, using these collision rates and assumed background continuum, to push a significant fraction of the population to highly excited states where we are unable to derive upper state column densities.

Fitting the observed $H_2{}^{33}S$ and $H_2{}^{34}S$ emission to a grid of RADEX models indicates that the H_2S emission originates from extremely dense gas ($n_{H_2} > 10^8$ cm^{-3}; see text below and Figs. 4.6 and 4.9). We therefore take the correction factors for $n_{H_2} \geq 10^8$ cm^{-3} as most representative of the H_2S emitting gas in the Orion KL hot core. For these high densities, our derived values for CF have a maximum range of 2.6–3.5 when $T_{kin} \geq 100$ K, thus we have detected approximately 29 – 38% of the total population with the HIFI scan. Applying a correction factor of 3.05 $\pm$ 0.45, where the uncertainty encompasses the entire range in CF, yields $N_{tot}(H_2{}^{32}S) = 9.5 \pm 1.9 \times 10^{17}$ cm^{-2}. Assuming an H_2 column density of 3.1×10^{23} cm^{-2} toward the Orion hot core (Plume et al., 2012), we derive an $H_2{}^{32}S$ abundance of $3.1 \pm 0.6 \times 10^{-6}$. Assuming solar metallicity, our abundance corresponds to approximately 12% of the available sulfur in H_2S. Using an H_2 column density measurement of 2.5×10^{24} cm^{-3}, which is more in line with dust continuum observations (see Sec. 4.3.2), on the other hand, yields an $H_2{}^{32}S$ abundance of $3.8 \pm 0.8 \times 10^{-7}$, corresponding to 1% of sulfur atoms in H_2S.

Having constrained $N_{tot}(H_2{}^{32}S)$, we now determine which values of T_{kin} and n_{H_2} best reproduce the observed emission. In order to do this, we constructed a grid of RADEX models that varied T_{kin} and n_{H_2}. The grid covered the following ranges in parameter space: $n_{H_2} = 10^{7-12}$ cm^{-3}, evaluated in logarithmic steps of 0.1, and T_{kin} = 40 – 800 K, evaluated in linear steps of 20 K. Grids were computed using both the CR1 and CR2 rates. In order to compare our data to the grid, we carried out reduced chi squared, χ^2_{red}, goodness of fit calculations using T_{peak} as the fitted

parameter.

We noticed when N_{tot} approached 10^{18} cm^{-2}, commensurate with our derived value for $N_{tot}(H_2{}^{32}S)$, that RADEX either failed to properly converge or the code produced a segmentation fault for some regions in the parameter space. Furthermore, using such a high column density produced optical depths in excess of 100 in some low energy lines for certain combinations of T_{kin} and n_{H_2}. Predicted line intensities for such transitions can not be trusted when using RADEX (van der Tak et al., 2007). As a result, the χ^2_{red} was evaluated using only the $H_2{}^{33}S$ and $H_2{}^{34}S$ lines, which have lower optical depths than the main isotopologue. We thus had 32 data values with which to compare to our models[1]. There are two fitted parameters: T_{kin} and n_{H_2}, yielding 30 degrees of freedom. We set θ_s and $N_{tot}(H_2{}^{32}S)$ to our derived values of $6''$ and 9.5×10^{17} cm^{-2}, respectively. Each grid point, then, included two model realizations, one for $H_2{}^{33}S$ and $H_2{}^{34}S$, with N_{tot} values scaled according to Orion KL isotopic ratios. That is, we set $N_{tot}(H_2{}^{34}S) = 4.8 \times 10^{16}$ cm^{-2} and $N_{tot}(H_2{}^{33}S) = 1.3 \times 10^{16}$ cm^{-2}. We also set Δv equal to 8.6 km/s, the average measured line width in our dataset for the hot core.

The upper and lower panels of Fig. 4.6 are χ^2_{red} contour plots for model grids using the CR1 and CR2 rates, respectively. The contours correspond to P values of 0.317 ($\chi^2_{red} = 1.1$), 0.046 ($\chi^2_{red} = 1.5$), and 0.003 ($\chi^2_{red} = 1.9$) representing 1, 2, and 3 σ confidence intervals, respectively. Models lying outside the largest contour are thus statistically inconsistent with the data. We see from the figure that, for both sets of collision rates, high density solutions are necessary to fit the data. We constrain n_{H_2} to be $\gtrsim 3 \times 10^8$ cm^{-3} based on the CR2 rates, which require lower density solutions relative to the CR1 rates by a factor of ~ 10 to achieve the same goodness of fit. This is a result of the fact that the CR2 rates are larger than the CR1 rates. Combining the ranges in T_{kin} covered by the 1 σ contours for the CR1 and CR2 grids, we constrain $T_{kin} = 130\pm^{33}_{15}$ K. The best fit solutions produce good agreement over the entire range in upper state energy over which $H_2{}^{33}S$ and $H_2{}^{34}S$ are

[1]We exclude the $H_2{}^{33}S$ and $H_2{}^{34}S$ $6_{0,6}$–$5_{1,5}$ lines from our fit because of self-blending with the $6_{1,6}$–$5_{0,5}$ transition.

detected. Fig. 4.7 (large bottom panel) plots the ratio of predicted to observed T_{peak} as a function of E_{up}. The blue points represent T_{peak} ratios calculated using a model with T_{kin} = 130 K and $n_{H_2} = 7.0 \times 10^9$ cm^{-3}, a solution within the 1 σ confidence interval assuming the CR2 collision rates and the observed continuum (Fig. 4.6, lower panel). Fig. 4.7 (small upper panels) also plots a sample of six $H_2{}^{34}S$ lines arranged so that E_{up} increases from the lower left panel to the upper right. The same model is overlaid as a blue solid line. From the figure, we see good agreement between the data and model, given the uncertainties, over the full range in excitation that we detect emission from both $H_2{}^{33}S$ and $H_2{}^{34}S$.

The best fit solutions to the isotopic emission under predict the most highly excited $H_2{}^{32}S$ lines. Fig. 4.8 is a plot of eight highly excited $H_2{}^{32}S$ transitions (black) with four RADEX models overlaid. The models assume our derived value of $N_{tot}(H_2{}^{32}S) = 9.5 \times 10^{17}$ cm^{-2} and use CR1 rates because the CR2 values do not include collisions into these states. Different curves correspond to models with $n_{H_2} = 1.5 \times 10^{10}$ and 1.5×10^{11} cm^{-3} (blue and red lines) and T_{kin} = 140 and 300 K (dashed and solid lines). We know from our analysis in Sec. 4.3.3 that an LTE solution with $T_{rot} \approx 140$ K reproduces the observed emission. Above the critical density for these transitions we, therefore, expect RADEX to predict line intensities comparable to what is observed for $T_{kin} \approx 140$ K. Fig. 4.8 shows that this occurs at densities $\gtrsim 10^{11}$ cm^{-3} (dashed red line), though the emission is still somewhat under predicted. Assuming a distance of 414 pc (Menten et al., 2007) and that 74% of the mass is in hydrogen, a spherical clump with a 6″ diameter and uniform H_2 density $> 10^{11}$ cm^{-3} corresponds to a total clump mass $\gtrsim 6100$ M$_\odot$. Such a large value is not consistent with mm observation, which report total clump masses $\lesssim 40$ M$_\odot$ for the Orion KL hot core (e.g. Favre et al., 2011; Wright & Vogel, 1985; Wright et al., 1992). Even if our clump mass lower limit is overestimated by an order of magnitude because of uncertainties in the collision rates, we still predict values a factor of ∼15 larger than what mm-observations derive. We therefore conclude that LTE solutions require unrealistically high densities. Alternatively, Fig. 4.8 also shows that the highly excited $H_2{}^{32}S$ emission is well fit at lower densities if $T_{kin} \approx 300$ K (solid

blue line). Such solutions, however, are inconsistent with the isotopic emission. In other words, this range in parameter space (i.e. $n_{H_2} \gtrsim 10^{10}$ cm^{-3}, $T_{kin} \gtrsim 300$ K) exists outside the reduced χ^2 contour of 1.9 in Fig. 4.6.

It is clear that unrealistically high densities are required to reproduce the observed H_2S emission over the entire range in excitation. As mentioned above, our RADEX models incorporate the observed continuum toward IRc2. However, it is possible that this radiation field is an underestimate of that seen by H_2S, perhaps as a result of optical depth or geometrical dilution. Increasing the far-IR/sub-mm continuum in order to pump H_2S via the same transitions observed in our dataset tends only to push the predicted intensities of observed lines into absorption. However, if there is a source of luminosity within the hot core, deeply embedded hot dust emitting heavily in the mid-IR and the short wavelength end of the far-IR, where the hot core continuum peaks (i.e. $\lambda \lesssim 100$ μm), may be hidden because the continuum is optically thick. The dust optical depth estimates presented in Chapter 3 would certainly imply an optically thick continuum for $\lambda \lesssim 100$ μm (see Sec. 4.3.2). Using Eq. 4.5 and assuming the same values as Sec. 4.3.2, we estimate $\tau_d(100\ \mu\text{m}) \approx 6$. Genzel & Stutzki (1989), moreover, argue that the far-IR continuum may be optically thick based on the shape of the spectral energy distribution between 400 μm and 3 mm. We therefore conclude that the continuum is likely quite optically thick for $\lambda \lesssim 100$ μm toward the Orion KL hot core.

If H_2S is indeed probing heavily embedded gas near a hidden self-luminous source, the continuum seen by H_2S may be enhanced relative to what is observed especially where the continuum is most optically thick. Consequently, we enhanced the background continuum for $\lambda < 100$ μm in order to determine if this resulted in better agreement between the data and models. Fig. 4.9 is a reduced χ^2 contour plot produced using the same methodology as Fig. 4.6, except the assumed background continuum is enhanced by a factor of 8 for $\lambda < 100$ μm. We also note that when defining a radiation field within the RADEX program, the user can specify a dilution factor. For the observed continuum, we set the dilution factor to 0.25 or 1.0 for wavelengths less than or greater than 45 μm, respectively. For the enhanced continuum, we set

the dilution factor to 1.0 for all wavelengths, indicating the dust is co-spatial with the H_2S emitting gas. From Fig. 4.9, we see that, as a result of the enhanced radiation field, the 3 σ lower limit on n_{H_2} is shifted lower by approximately a factor of 3 for both the CR1 and CR2 rates. Using these contour plots in the same way as before, we constrain $n_{H_2} \gtrsim 9 \times 10^7$ cm^{-3} and $T_{kin} = 120 \pm^{13}_{10}$ K.

As with the observed continuum, the best fit solutions using the enhanced radiation field reproduce the observed $H_2{}^{33}S$ and $H_2{}^{34}S$ emission well over all excitation energies. Predicted to observed T_{peak} ratios using a model with $T_{kin} = 120$ K and $n_{H_2} = 3.0 \times 10^9$ cm^{-3} and assuming the enhanced continuum are overlaid in Fig. 4.7 as red points in the large bottom panel and as dashed red lines in the six smaller upper panels. This solution lies within the 1 σ contour in Fig. 4.9 assuming CR2 collision rates (lower panel). From the figure, we see good agreement between the data and model at all excitation energies. The enhanced continuum, furthermore, produces better agreement with the most highly excited $H_2{}^{32}S$ lines. Fig. 4.10 plots the same highly excited $H_2{}^{32}S$ lines given in Fig. 4.8. The overlaid model, which is plotted in red, corresponds to $T_{kin} = 120$ K and $n_{H_2} = 3.0 \times 10^9$ cm^{-3} using the CR1 rates. This is the same model used in Fig. 4.7 and lies within the 2 σ contour of the enhanced continuum CR1 grid (Fig. 4.9, upper panel). The plot shows good agreement between these highly excited transitions and the model, indicating that an intense far-IR ($\lambda < 100$ μm) radiation field can excite these states for densities and temperatures consistent with the isotopic emission.

The mechanism by which H_2S is pumped is illustrated in Fig. 4.11. The plot shows the same energy level diagram given in Fig. 4.2, except the lines connecting the levels are now transitions with $\lambda < 100$ μm and $\mu^2 S > 0.01$. From the plot, we see that there are a litany of $\Delta J = 1$ transitions for $J \gtrsim 3$ through which the background radiation field can excite H_2S. However, the $\lambda < 100$ μm continuum is unable to pump states below J = 3 – 4 because these transitions occur at longer wavelengths (probed by HIFI), where the continuum is more optically thin. High densities, therefore, are still required to populate states up to J = 3 – 4 in order for H_2S to be pumped to more highly excited states. This is somewhat different from traditional pumping as

seen, for example, in OH, where the ground state transitions couple directly to the intense radiation field which pumps to higher levels. In the case of H_2S, the pumping requires excitation via collisions to higher states in order for radiation to redistribute the population. We note that although we nominally increased the continuum for $\lambda < 100$ μm, the transitions plotted in Fig. 4.11 occur at wavelengths in the range 39 – 100 μm. It is thus the short wavelength end of the far-IR that is responsible for the H_2S pumping.

Fundamental vibrational transitions for H_2S occur at wavelengths $\lesssim 8.5\mu$m. In this wavelength region, the observed radiation field is weaker than the continuum responsible for pumping H_2S rotation transitions (39 – 100μm) by over an order of magnitude. Nevertheless, we searched for the presence of vibrationally excited H_2S in the HIFI scan. Vibrational transitions were obtained from the HITRAN database. Although these measurements did not include pure rotation transitions within an excited vibrational state, (and as of yet have not been measured in the laboratory), we computed approximate frequencies for several rotation lines with $J < 4$ within the ν_1, ν_2, and $\nu_3 = 1$ states by taking upper state energy differences. Given that E_{up} values for these states are reported to a precision of 1 part in 10^4, the frequencies should be accurate to within a few km/s in the HIFI scan. We searched for emission near these frequencies by plotting the data with the full band model overlaid to identify line blends. We did not detect unidentified lines at these frequencies that could be attributed to vibrationally excited H_2S, but note that many of these transitions were in spectral regions of high line density making it difficult to search for such features.

We also investigated the significance of vibrational excitation in our models by computing HITRAN versions of the CR1 and CR2 collision rates. We produced a coarse model grid with $N_{tot} = 10^{17}$ cm^{-2} and varied n_{H_2} and T_{kin} within ranges 10^7 – 10^{10} cm^{-3}, evaluated in logarithmic steps of 1, and 100 – 400 K, evaluated in 100 K steps, respectively. For each grid point, we produced a model with and without vibrational excitation and compared the predicted line fluxes. In most instances, these values agreed to within 10%, provided a given state was sufficiently populated to produce detectable emission. This agreement held when using both the observed and

enhanced continuum models. We thus conclude the presence of vibrational excitation does not significantly affect our results, assuming the two radiation fields discussed in this work. The caveat here is that if H_2S is probing gas near a hidden source of luminosity, the shape of the continuum seen by H_2S may be more strongly peaked in the mid-IR possibly producing higher levels of vibrational excitation.

4.3.6 D/H Ratio Upper Limit

We do not detect HDS emission toward Orion KL. In order to compute an upper limit for the column density of HDS, we looked at six line free regions in the HIFI scan where emissive low energy HDS lines should be present. The transitions we used are given in Table 4.6. We used the XCLASS program[2] to compute model spectra, which assumes LTE level populations. We also assumed a source size of $6''$, Δv=8.6 km/s, and T_{rot} = 141 K, in agreement with our rotation diagram analysis (Sec. 4.3.3). We then increased the column density until the peak line intensities exceeded 3 $\times$ the local RMS in all lines. This procedure yields an upper limit on the column density of $N_{tot}(HDS) < 4.7 \times 10^{15}$ cm^{-2}. Using the H_2S column density derived from our non-LTE analysis (Sec. 4.3.5), this corresponds to a D/H ratio $< 4.9 \times 10^{-3}$.

4.4 Discussion: Origin of H_2S emission

Our results indicate that H_2S is a tracer of extremely dense gas toward the Orion KL hot core and that the far-IR background continuum plays a significant role in the excitation of this molecule especially for the most highly excited transitions in our dataset. Moreover, the observed far-IR continuum ($\lambda < 100$ μm) toward IRc2 is not sufficient to reproduce the excitation that we detect. These results point to an H_2S origin in heavily embedded, dense gas close to a hidden source of luminosity that heats nearby dust which cannot be directly observed because the continuum is optically thick in the mid- and short-wavelength-far-IR. Such an object (or objects) may be the ultimate source of Orion KL's high luminosity ($\sim 10^5$ $L_\odot$; Wynn-Williams et al., 1984) and thus harbor an intense far-IR radiation field responsible for the

[2]http://www.astro.uni- koeln.de/projects/schilke/XCLASS

highly excited H_2S transitions we observe toward Orion KL.

Finding evidence for the presence of hidden self-luminous sources toward Orion KL is difficult not only because of the high IR optical depth, but also because of its elaborate physical structure. Near to mid-infrared maps reveal the presence of many IR clumps ("IRc" sources), only a small fraction of which may be self luminous (see e.g. Rieke et al., 1973; Downes et al., 1981; Lonsdale et al., 1982; Werner et al., 1983; Gezari et al., 1998; Greenhill et al., 2004a; Shuping et al., 2004; Robberto et al., 2005; Okumura et al., 2011; De Buizer et al., 2012). The situation is further complicated by the presence of radio source I (Churchwell et al., 1987), a supposed heavily embedded massive protostar, which may be externally heating nearby clumps. Okumura et al. (2011), for example, studied the interaction between radio source I and IRc2, the brightest clump in the mid-infrared and once thought to be the source of Orion KL's high luminosity. More recent observations, however, have ruled this out (Dougados et al., 1993; Gezari et al., 1998; Shuping et al., 2004). In fitting the mid-IR SED of IRc2, Okumura et al. (2011) find that they can not fit the data with a single blackbody. Instead they require two blackbody components with temperatures of 150 and 400 K, the hotter component supplying most of the flux for $\lambda \lesssim 12$ μm. The origin of the hotter component, they argue, is scattered radiation from radio source I, which lies approximately $1''$ away from IRc2, and the source toward which they detect a prominent 7.8 / 12.4 μm color temperature peak. Evidence of this hotter component can be seen in Fig. 4.4 as excess emission for $\lambda \lesssim 10$ μm. Focusing on slightly longer wavelengths, De Buizer et al. (2012) present mid-IR SOFIA maps obtained with the FORCAST camera which show 19.7 / 31.5 μm and 31.5 / 37.5 μm color temperature peaks toward IRc4 indicating that it may also be self-luminous.

Previous observations of highly excited molecular lines in the mm and sub-mm have confirmed the influence of an intense far-IR continuum within the Orion KL hot core. Hermsen et al. (1988), for example, present both metastable and non-metastable inversion transitions of NH_3 spanning a large range in excitation energy ($\sim$ 1200 K). Comparing their observations to non-LTE models which specify n_{H_2}, T_{kin}, the dust temperature, T_{dust}, and the dust optical depth at 50 μm, $\tau_d(50\ \mu m)$, they find a best

fit solution using $n_{H_2} = 10^7$ cm^{-3}, $T_{kin} = 150$ K, $T_{dust} = 200$ K, and $\tau_d(50\ \mu m) = 10$. The strong far-IR radiation field produced by the hot, optically thick dust, they argue, is necessary to explain the highly excited ($E_{up} > 700$ K) non-metastable NH_3 lines. Using a similar methodology, Jacq et al. (1990) analyzed several HDO transitions spanning a range in E_{up} of approximately 50 to 840 K toward the Orion KL hot core. Their best fit model sets $n_{H_2} = 10^7$ cm^{-3}, $T_{kin} = T_{dust} = 200$ K, and $\tau_d(50\ \mu m) = 5$, again resulting in a strong far-IR background continuum. As a consequence, this model predicts that far-IR pumping is the dominant excitation mechanism for HDO lines with $E_{up} \gtrsim 150$ K toward the Orion KL hot core. Goldsmith et al. (1983), furthermore, require a strong mid/far-IR radiation field ($\lambda \leq 44\mu$m) in order to explain their observations of vibrationally excited CH_3CN and HC_3N. Based on their computed CH_3CN vibrational excitation temperature and a scaling law from Scoville & Kwan (1976), they infer dust temperatures $\gtrsim 260$ K for $\theta < 1''$.

It is clear that the far-IR radiation field plays a significant role in the excitation not only of H_2S but several other molecular species within the Orion KL hot core. An enhancement in the far-IR continuum can be explained by the presence of hot dust. Assuming that the H_2S emission originates from embedded hot dust with a temperature of $\sim$200 K as opposed to 65 K, which is more in line with our observed radiation field (Fig. 4.4), we would expect approximately a factor of 9 enhancement at $\sim$ 85 μm assuming blackbody emission. It is possible that the CR1 collision rates are significantly underestimated for highly excited H_2S emission, creating a need for a stronger far-IR field. Such a suspicion is reasonable given that the CR1 rates are smaller than the CR2 rates. Furthermore, the presence of both density and temperature gradients may also reduce the need for such a strong enhancement in the far-IR continuum because extremely compact, hot regions may contribute to the H_2S excitation at high energies. Such an investigation is beyond the scope of this study because it requires more detailed radiative transfer calculations that would involve modeling the physical structure of the Orion KL hot core. Nevertheless, the most highly excited H_2S lines either require an exceedingly high density or an enhanced continuum. As argued above, the second scenario is more likely.

Our *Herschel*/HIFI observations contain little spatial information, the true origin of the H_2S emission therefore cannot be unambiguously determined from our dataset alone. Two pointings, however, were obtained toward Orion KL in bands 6 and 7 ($\nu > 1430$ GHz) because of the relatively small beam size at these wavelengths ($\lesssim 15''$). The first pointing, toward the hot core, is given in Sec. 4.2 and is almost coincident ($< 1''$) with radio source I. The second pointing is positioned toward the compact ridge at coordinates $\alpha_{J2000} = 5^h35^m14.1^s$ and $\delta_{J2000} = -5°22'36.5''$, and is located $8''$ SW of the hot core pointing much closer to IRc4 ($\sim 2''$ away). We also note that the main pointing for bands 1 – 5 lies midway between the hot core and compact ridge positions. The three pointings, thus, make a NE-SW line across the KL region. Fig. 4.12 plots a sample of six H_2S lines that lie in bands 6 and 7 for the hot core (black) and compact ridge (red) pointings. From the plot, we immediately see that the H_2S emission is stronger in the hot core pointing relative to the compact ridge, indicating that the H_2S emission is compact and clumpy and that the majority of the emission likely originates from a region closer to IRc2/radio source I as opposed to IRc4, the putative self luminous source reported by De Buizer et al. (2012).

Our derived H_2S abundance is at least two orders of magnitude larger than those measured toward other massive hot cores, which typically have abundances between 10^{-9} and 10^{-8} (Hatchell et al., 1998; van der Tak et al., 2003). If H_2S does indeed originate from grain surfaces as has been suggested by Charnley (1997), such a large abundance may be the result of increased evaporation from dust grains. Such an interpretation has been invoked for H_2O, a structurally similar molecule to H_2S, toward the hot core. Using the Orion KL HIFI survey, Neill et al. (2013) derive an extremely large H_2O abundance of 6.5×10^{-4} and a high water D/H ratio of 3.0×10^{-3}, which they suggest are a result of ongoing evaporation from dust grains. Our measurement of an H_2S ortho/para ratio < 3, though not at a 3 σ level, also points to H_2S formation at cold temperatures possibly on grain surfaces during an earlier, colder stage. There is, however, no direct observational evidence to support an H_2S origin on grain surfaces. Near-IR spectroscopic observations of high and low mass protostars have failed to detect H_2S or any other sulfur bearing species except,

possibly, OCS in the solid phase (Gibb et al., 2004; Boogert et al., 2000; Smith, 1991; Palumbo et al., 1995, 1997). Goicoechea et al. (2006), moreover, find evidence for low depletion levels of sulfur in the Horsehead PDR. Comparing their measured CS and HCS^+ abundances to photochemical models, they require a total gas phase sulfur abundance that is $\gtrsim 25\%$ the solar elemental abundance of sulfur. Given that our derived H_2S abundance implies $\lesssim 12\%$ of the available sulfur is in the form of H_2S, an H_2S origin on grain surfaces may not necessarily be inconsistent with the Goicoechea and near-IR studies. All currently explored H_2S gas phase formation routes are highly endothermic, with some key reactions having activation energies $\sim 10^4$ K (see e.g. Pineau des Forets et al., 1993; Mitchell, 1984, and references therein). Gas phase formation of H_2S is, therefore, possible in shocks but is difficult to explain at hot core densities and temperatures. Given, however, that high temperature sulfur chemistry is still not well understood, it is possible that H_2S may have formed in the gas phase by some, as of yet, unexplored route.

4.5 Conclusions

We have analyzed the H_2S emission toward the Orion KL hot core. In total we detect 52, 24, and 8 unblended or partially blended lines from $H_2{}^{32}S$, $H_2{}^{34}S$, and $H_2{}^{33}S$, respectively, spanning a range in E_{up} of 55 – 1233 K. Analysis of the extremely optically thick low energy $H_2{}^{32}S$ lines indicates that the H_2S emitting gas is compact ($\theta_s \sim 6''$). Measured line intensities of the same transition from different isotopologues allowed us to compute upper state column densities for individual states. Using these N_{up} measurements, we constructed rotation diagrams for ortho and para H_2S and derived $T_{rot} = 141 \pm 12$ K and $N_{tot}(H_2{}^{32}S) = 8.3 \pm 1.4 \times 10^{17}$ cm^{-2} (ortho + para H_2S). We measured the H_2S ortho/para ratio using two different methods which yield values of 2.5 ± 0.8 and 1.7 ± 0.8, both of which suggest a ratio less than the equilibrium value of 3 but are not statistically inconsistent with thermal equilibrium given the uncertainties. Although we do not detect HDS, we derive a D/H ratio upper limit of $< 4.9 \times 10^{-3}$.

We also modeled the H_2S emission using the RADEX non-LTE code assuming two

different sets of estimated collision rates. We derived a value for the total column density, $N_{tot}(H_2{}^{32}S) = 9.5 \pm 1.9 \times 10^{17}$ cm^{-2}, by computing a correction factor to account for the H_2S column not probed by HIFI. Using this column density, we constrain $n_{H_2} \gtrsim 9 \times 10^7$ cm^{-3} and $T_{kin} = 120 \pm {}^{13}_{10}$ K by comparing a grid of RADEX models to the $H_2{}^{33}S$ and $H_2{}^{34}S$ emission. These constraints require that the observed continuum be enhanced by a factor of 8 for $\lambda < 100$ μm. Enhancing the background continuum also produces good agreement between the data and models for the most highly excited $H_2{}^{32}S$ lines, which are populated primarily by pumping from the short wavelength end of the far-IR ($\lambda \approx 39$ – 100 μm), for temperatures and densities consistent with the rarer isotopic emission. We conclude that the H_2S emitting gas must be tracing markedly dense heavily irradiated gas toward the Orion KL hot core. These conditions point to an H_2S origin in heavily embedded material in close proximity to a hidden source of luminosity. The source of this luminosity remains unclear.

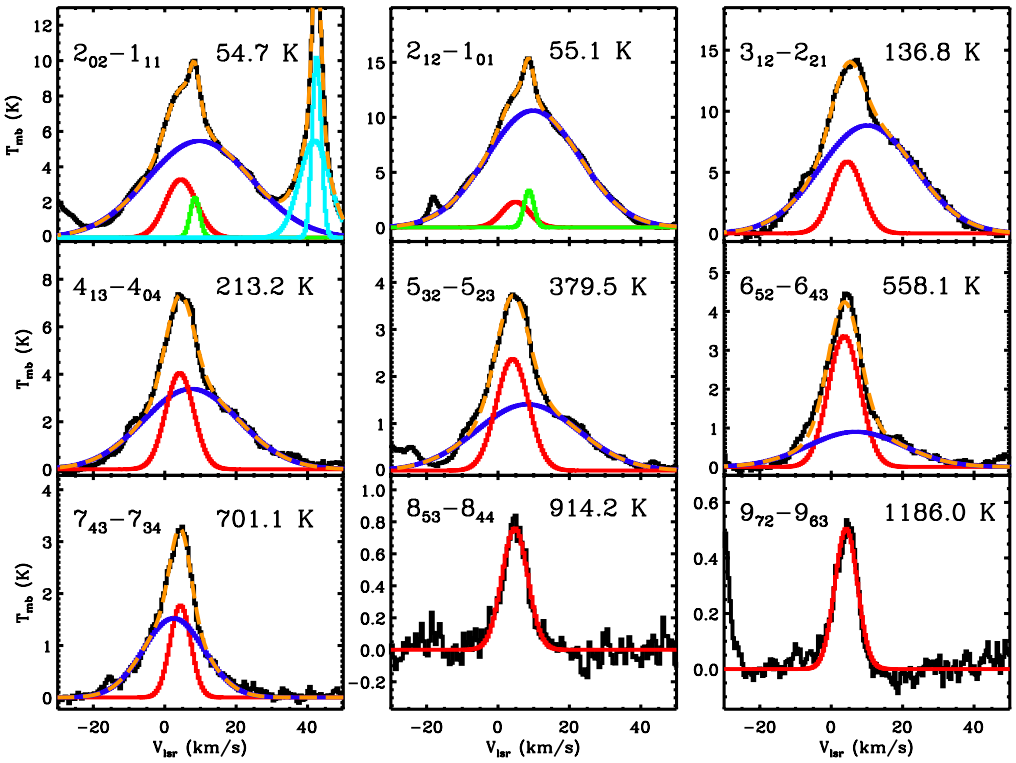

Figure 4.1: A sample of nine $H_2{}^{32}S$ lines observed in the HIFI scan with Gaussian fits to the outflow, extended ridge, and hot core spatial/velocity components overlaid in blue, green, and red, respectively. The data are plotted in black and uniformly smoothed to a resolution of ∼0.5 km/s. Blending lines that were also fit are plotted in cyan. The sum of all components is plotted as an orange dashed line. The upper state energy of the transition is given in each panel and increases from the upper left panel to the lower right.

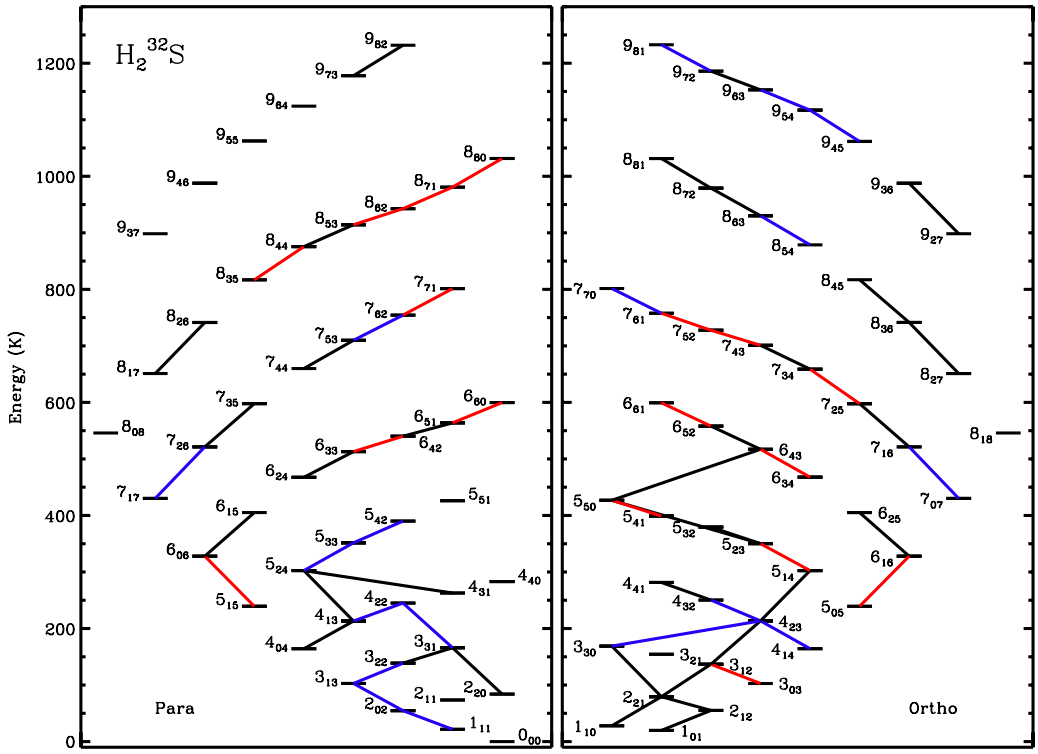

Figure 4.2: The right and left panels plot energy level diagrams for ortho and para $H_2{}^{32}S$, respectively. Transitions detected in the HIFI scan are indicated by lines connecting upper and lower states and are color coded according the how blended each transition is. Black, blue, and red correspond to categories 1 (not blended), 2 (partially blended), and 3 (heavily blended), respectively. See Sec. 4.3.1 for more details on how these categories are defined.

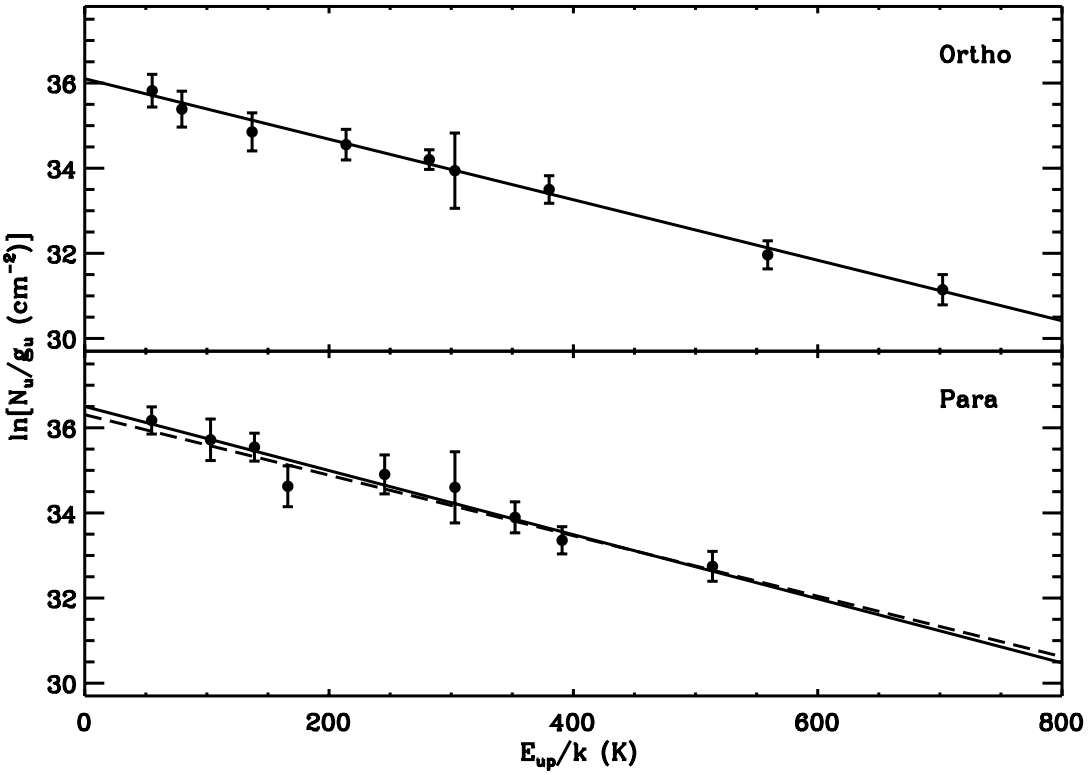

Figure 4.3: Rotation diagrams for ortho and para states where N_{up} values could be computed are given in the upper and lower panels, respectively. All points were derived assuming a source size of 6″ and Orion KL isotopic ratios. Independent linear least squares fits to the ortho and para points are plotted as solid lines in either panel. The dashed line in the bottom panel is a fit to the para points with T_{rot} fixed at 141 K, the rotation temperature derived from ortho H_2S.

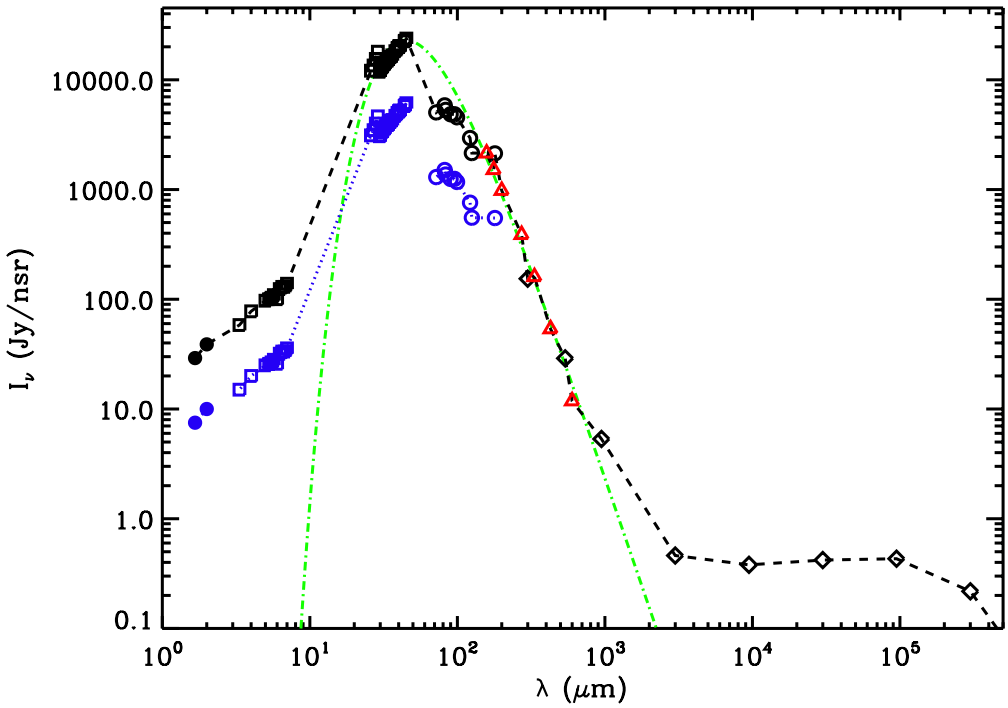

Figure 4.4: The observed continuum toward IRc2. The red triangles indicate the continuum level as measured in the HIFI scan. The blue squares and circles (not filled in) correspond to flux measurements obtained from ISO SWS (van Dishoeck et al., 1998) and LWS (Lerate et al., 2006), respectively. The blue dots (filled in) represent observations from Lonsdale et al. (1982). The black squares, circles, and dots are the same measurements as their respective blue counterparts normalized so that the LWS observations agree with the HIFI continuum at ∼158 μm. Black diamonds correspond to flux measurements presented by Dicker et al. (2009). The green dot-dashed line is a 65 K blackbody. The black dashed line represents the "observed radiation field" used in the RADEX models described in the text.

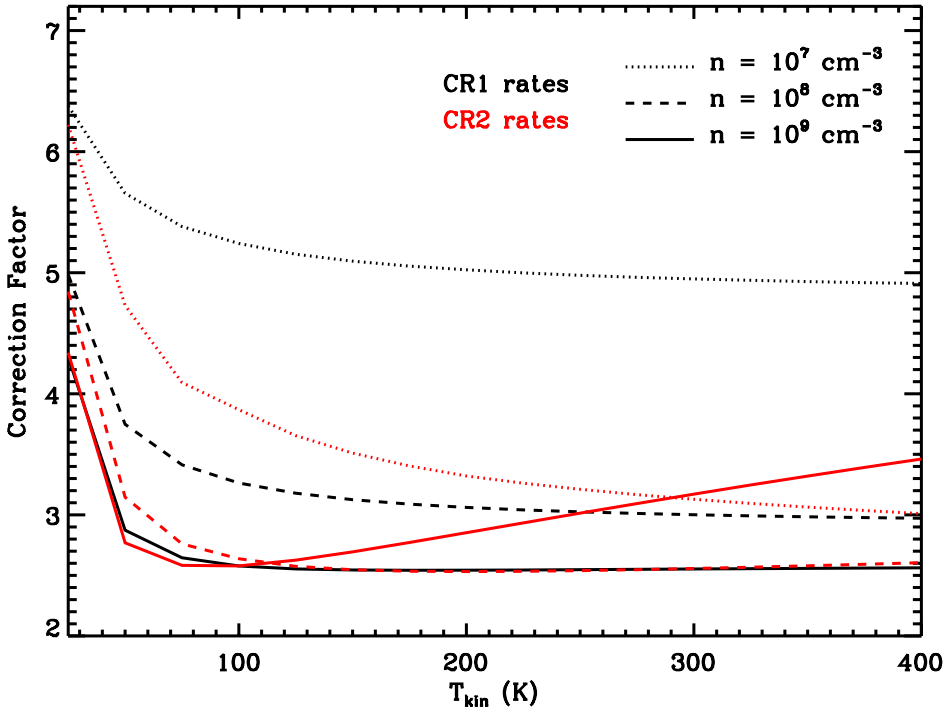

Figure 4.5: Correction factors derived using RADEX which convert N_{obs} to N_{tot}. CF values are plotted as a function of kinetic temperature with different densities plotted as different line types. Both the CR1 (black) and CR2 (red) collision rates were used. These curves were computed assuming the enhanced continuum and set $N'_{tot} = 5.0 \times 10^{16}$ cm^{-2} to avoid any convergence problems associated with high column densities.

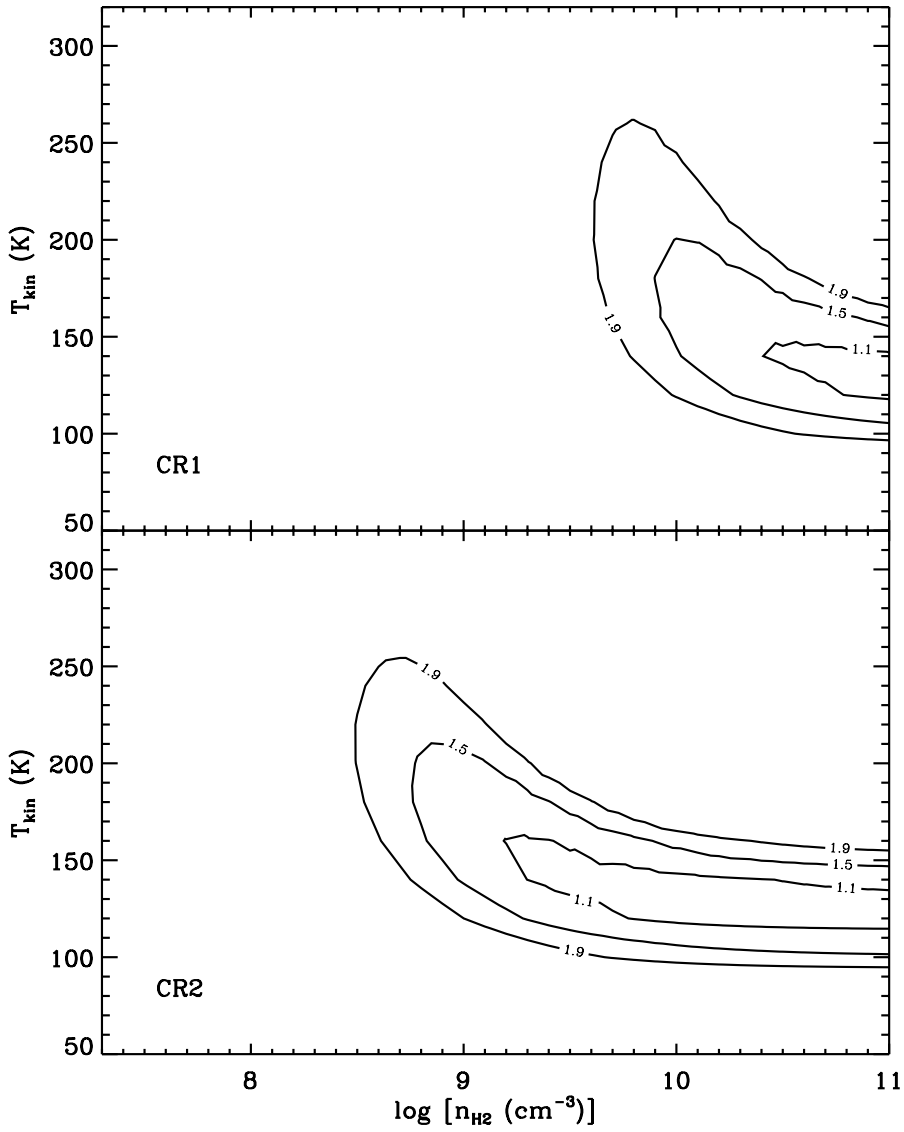

Figure 4.6: The upper and lower panels are $\chi^2_{\rm red}$ contour plots comparing $H_2{}^{33}S$ and $H_2{}^{34}S$ emission to RADEX model grids assuming CR1 and CR2 collision rates, respectively. All model realizations assume the observed radiation field, and set $\theta_s = 6''$and Δv = 8.6 km/s. We also set $N_{\rm tot}(H_2{}^{32}S) = 9.5 \times 10^{17}$ cm^{-2}, but scale the isotopic emission according to Orion KL ratios. The $\chi^2_{\rm red}$ values corresponding to each contour are labeled in the plot.

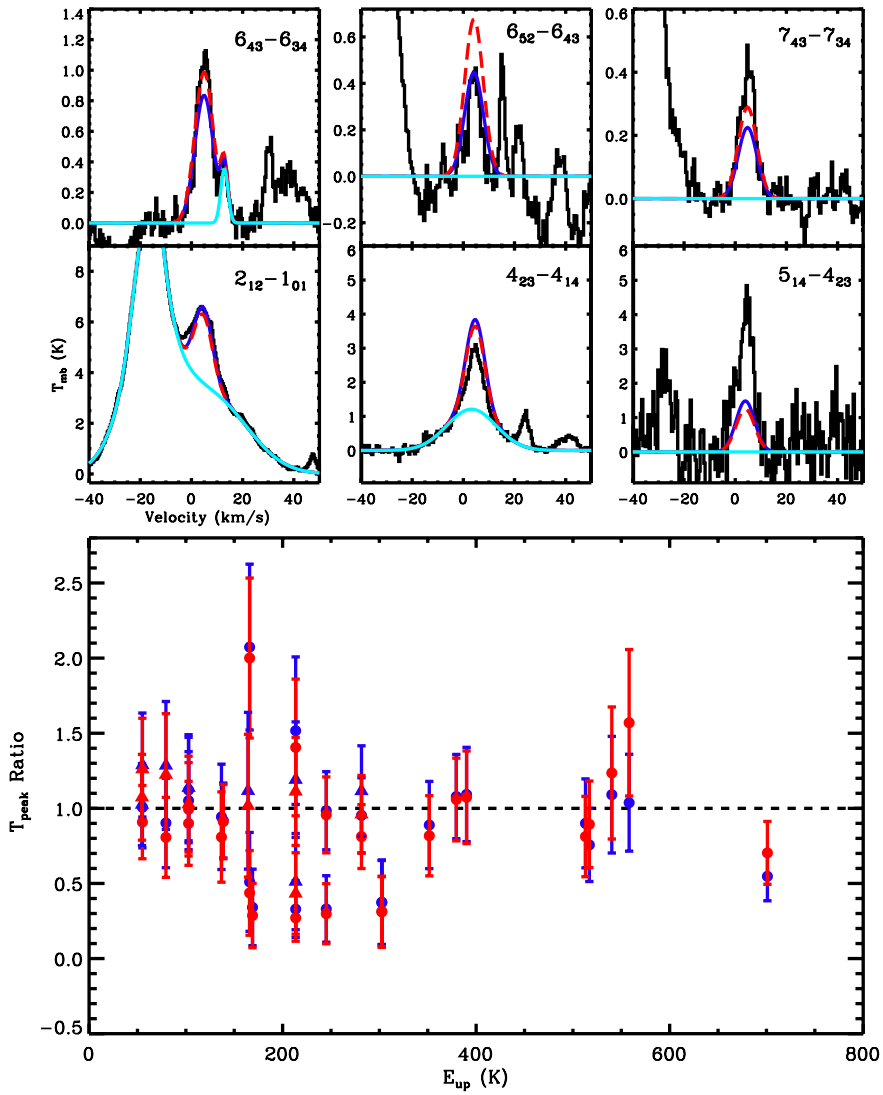

Figure 4.7: The large bottom panel plots the ratio of predicted and observed values for T_{peak} as a function of upper state energy. Blue and red points represent T_{peak} ratios computed using RADEX models that fit the data well ($\chi^2_{red} < 1.1$) assuming the observed ($n_{H_2} = 7.0 \times 10^9$ cm^{-3}, $T_{kin} = 130$ K) and enhanced ($n_{H_2} = 3.0 \times 10^9$ cm^{-3}, $T_{kin} = 120$ K) radiation fields, respectively. Dots and triangles correspond to $H_2{}^{34}S$ and $H_2{}^{33}S$ isotopologues, respectively. The upper panels plot a sample of $H_2{}^{34}S$ lines in black with the same models overlaid using the same color conventions as the lower panel (the red line is dashed because it overlaps with the blue in some instances). The transitions increase in excitation from the lower left panel to the upper right, and span the entire range in excitation over which $H_2{}^{34}S$ emission is detected. The models use CR2 collision rates and set $\theta_s = 6''$, $\Delta v = 8.6$ km/s, $N_{tot}(H_2{}^{34}S) = 4.8 \times 10^{16}$ cm^{-2}, and $N_{tot}(H_2{}^{33}S) = 1.3 \times 10^{16}$ cm^{-2}.

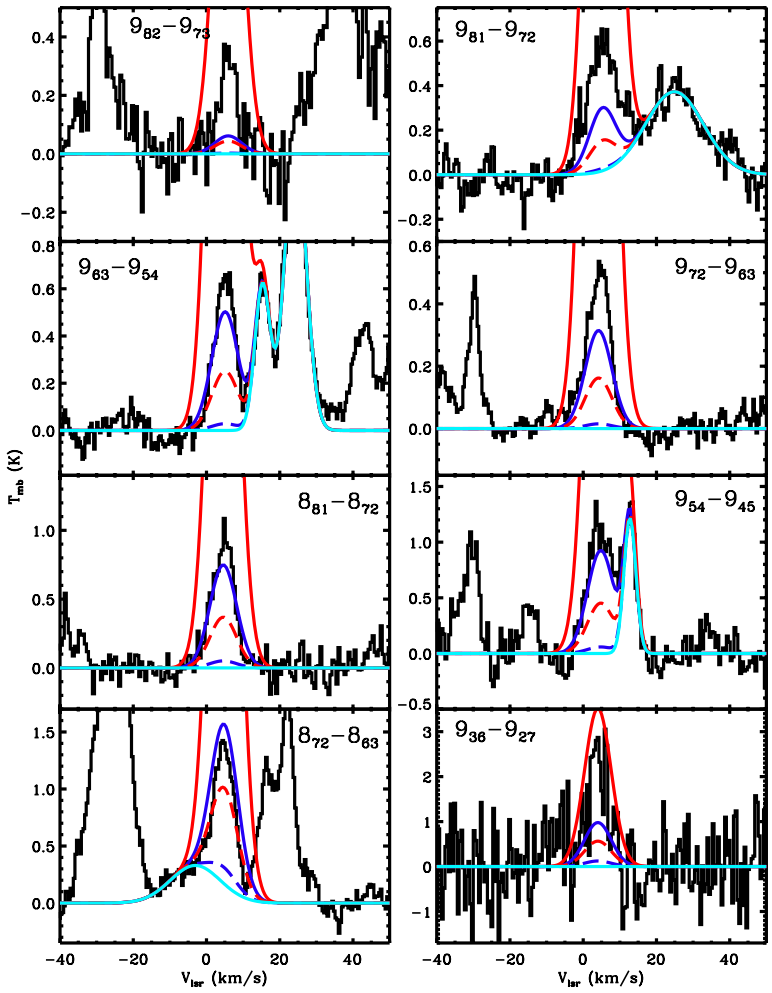

Figure 4.8: Each panel plots a highly excited $H_2{}^{32}S$ line in black. The transition is given in the upper part of each panel. RADEX models are overlaid as different colors and assume the observed radiation field. Blue and red lines correspond to models with $n_{H_2} = 1.5 \times 10^{10}$ and 1.5×10^{11} cm^{-3}, while dashed and solid lines correspond to $T_{kin} = 140$ and 300 K, respectively. All models set $\theta_s = 6''$, $\Delta v = 8.6$ km/s, $N_{tot}(H_2{}^{32}S) = 9.5 \times 10^{17}$ cm^{-2}, and use CR1 collision rates.

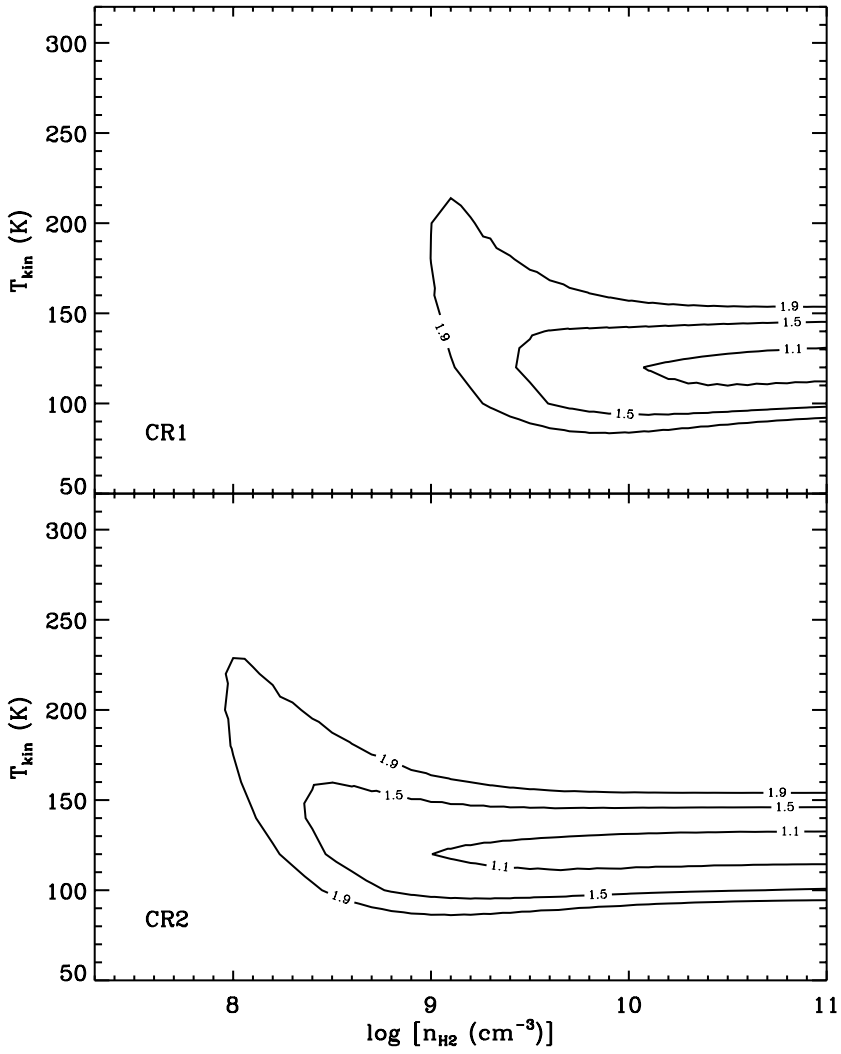

Figure 4.9: The upper and lower panels are $\chi^2_{\rm red}$ contour plots computed using the same methodology as Fig. 4.6, except the RADEX model grids used here assume a radiation field that is enhanced by a factor of 8 for $\lambda < 100$ μm. The $\chi^2_{\rm red}$ values corresponding to each contour are labeled in the plot.

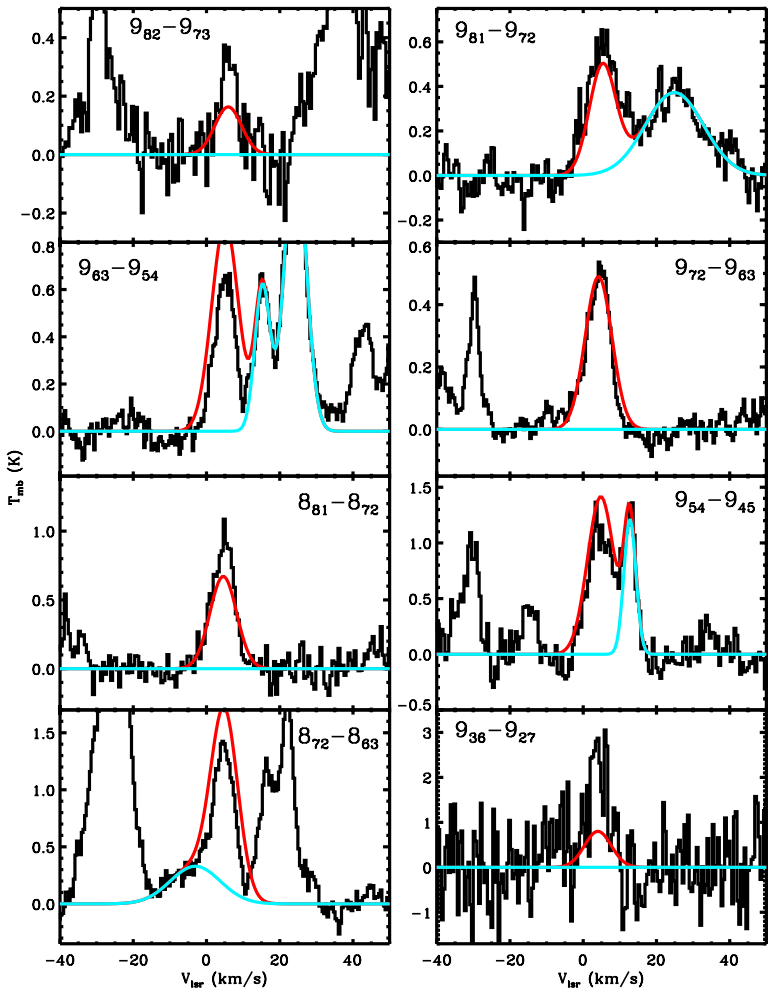

Figure 4.10: The same $H_2{}^{32}S$ transitions as Fig. 4.8 are plotted here with one RADEX model overlaid in red. This model assumes the enhanced continuum and sets $\theta_s = 6''$, $\Delta v = 8.6$ km/s, $n_{H_2} = 3.0 \times 10^9$ cm^{-3}, and $T_{kin} = 120$ K.

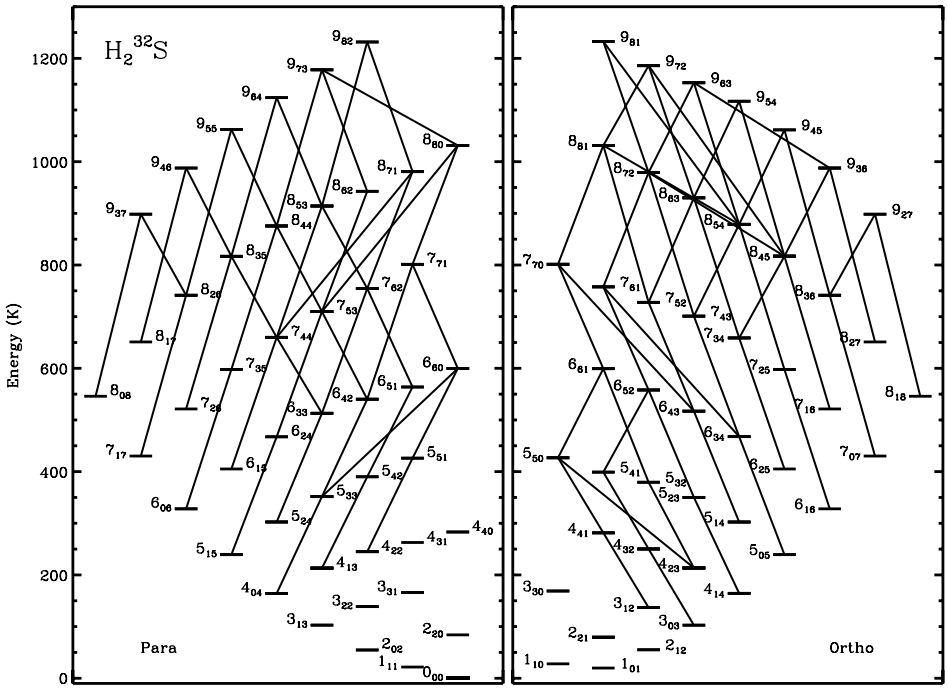

Figure 4.11: The same energy level diagram as Fig. 4.2 is plotted, except lines connecting the states represent transitions with $\lambda < 100$ μm and $\mu^2 S > 0.01$.

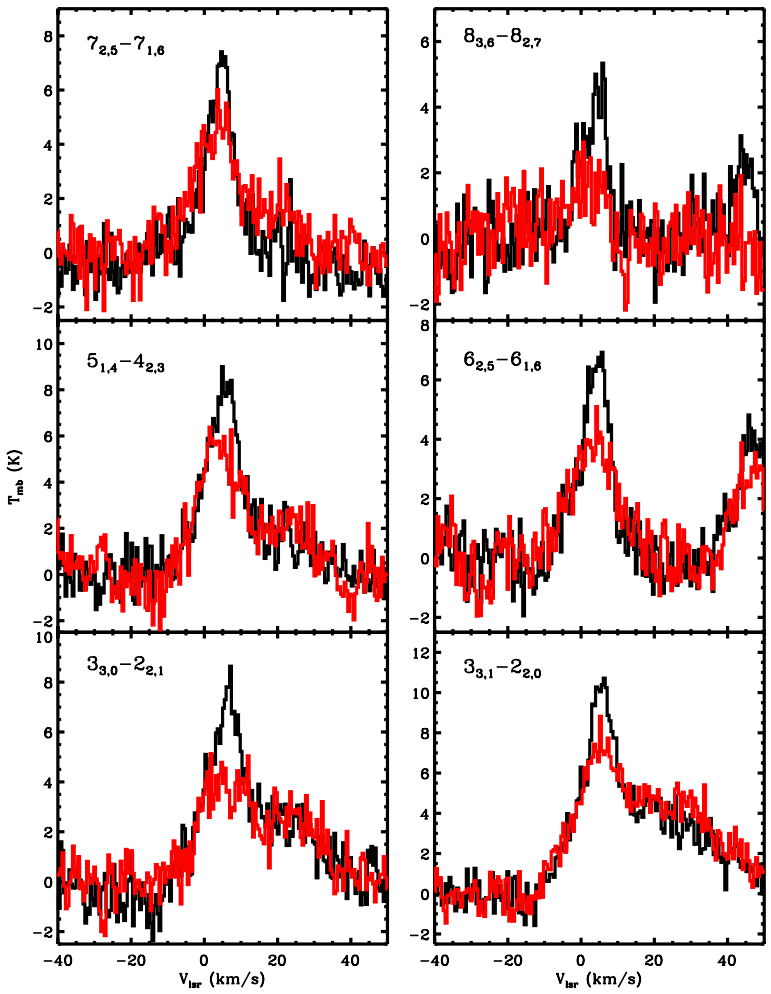

Figure 4.12: $H_2{}^{32}S$ lines from bands 6 and 7 are plotted for the hot core (black) and compact ridge (red) pointings. The lines are clearly stronger toward the hot core.

Table 4.1: Measured line parameters for the hot core

Transition (J_{K^-,K^+})	ν (GHz)	E_{up} (K)	v_{LSR} (km s^{-1})	Δv (km s^{-1})	T_{peak} (K)	$\int T_{mb} dv$ (K km s^{-1})	Notes[a]
			$H_2{}^{32}S$				
$2_{0,2}$–$1_{1,1}$	687.30	54.7	4.53 ± 0.18	10.25 ± 0.38	3.28 ± 0.03	35.84 ± 2.42	2
$2_{1,2}$–$1_{0,1}$	736.03	55.1	4.94 ± 0.03	8.86 ± 0.07	2.32 ± 0.04	21.84 ± 0.28	1
$2_{2,1}$–$2_{1,2}$	505.57	79.4	4.37 ± 0.59	11.39 ± 0.59	2.01 ± 0.02	24.33 ± 1.58	1
$2_{2,1}$–$1_{1,0}$	1072.84	79.4	3.86 ± 0.01	8.90 ± 0.09	3.42 ± 0.07	32.42 ± 0.21	1
$3_{1,3}$–$2_{0,2}$	1002.78	102.9	5.40 ± 0.01	13.22 ± 0.16	3.69 ± 0.10	51.89 ± 1.20	2
$3_{1,2}$–$2_{2,1}$	1196.01	136.8	4.49 ± 0.06	10.15 ± 0.18	5.87 ± 0.17	63.43 ± 1.72	1
$3_{2,2}$–$3_{1,3}$	747.30	138.7	4.87 ± 0.03	9.85 ± 0.16	3.57 ± 0.05	37.47 ± 0.88	2
$3_{3,1}$–$3_{2,2}$	568.05	166.0	4.61 ± 0.03	9.01 ± 0.08	1.58 ± 0.02	15.19 ± 0.19	1
$3_{3,1}$–$2_{2,0}$	1707.97	166.0	5.43 ± 0.15	6.67 ± 0.40	5.91 ± 0.64	41.97 ± 2.93	1
$3_{3,0}$–$2_{2,1}$	1865.62	169.0	5.87 ± 0.29	7.60 ± 0.75	4.17 ± 0.74	33.71 ± 4.25	1
$4_{1,3}$–$4_{0,4}$	1018.35	213.2	4.20 ± 0.09	9.29 ± 0.32	4.05 ± 0.09	40.03 ± 2.15	1
$4_{2,3}$–$3_{3,0}$	930.15	213.6	3.94 ± 0.05	8.75 ± 0.10	2.78 ± 0.06	25.93 ± 0.13	2
$4_{2,3}$–$4_{1,4}$	1026.51	213.6	3.84 ± 0.44	8.30 ± 0.44	4.33 ± 0.12	38.25 ± 1.97	2
$4_{2,3}$–$3_{1,2}$	1599.75	213.6	4.50 ± 0.17	9.70 ± 0.51	6.57 ± 0.60	67.90 ± 5.03	1
$4_{2,2}$–$4_{1,3}$	665.39	245.1	4.07 ± 0.45	10.40 ± 0.45	2.75 ± 0.05	30.40 ± 1.38	2
$4_{2,2}$–$3_{3,1}$	1648.71	245.2	3.83 ± 0.20	7.13 ± 0.65	6.50 ± 0.90	49.35 ± 6.57	2
$4_{3,2}$–$4_{2,3}$	765.94	250.3	3.21 ± 0.38	9.72 ± 0.31	3.16 ± 0.03	32.67 ± 2.83	2
$4_{4,1}$–$4_{3,2}$	650.37	281.5	4.13 ± 0.02	9.35 ± 0.06	2.38 ± 0.03	23.74 ± 0.25	1
$5_{1,4}$–$4_{2,3}$	1852.69	302.5	4.98 ± 0.18	9.35 ± 0.55	6.27 ± 0.68	62.36 ± 4.97	1
$5_{2,4}$–$4_{3,1}$	827.92	302.6	4.20 ± 0.28	7.05 ± 0.79	0.37 ± 0.06	2.81 ± 0.24	1
$5_{2,4}$–$4_{1,3}$	1862.44	302.6	5.15 ± 0.18	9.48 ± 0.48	6.54 ± 0.75	65.95 ± 2.64	1
$6_{0,6}$–$5_{1,5}$	1846.74	328.1	2.84 ± 0.19	11.17 ± 0.60	7.91 ± 0.73	94.07 ± 7.94	3
$5_{3,3}$–$5_{2,4}$	1023.12	351.7	3.86 ± 0.03	10.42 ± 0.10	4.50 ± 0.11	49.94 ± 0.71	2
$5_{3,2}$–$5_{2,3}$	611.44	379.5	4.06 ± 0.13	10.68 ± 0.39	2.37 ± 0.02	26.96 ± 1.63	1
$5_{4,2}$–$5_{3,3}$	800.85	390.1	4.01 ± 0.56	10.18 ± 0.56	2.98 ± 0.09	32.26 ± 1.28	2
$6_{1,5}$–$6_{0,6}$	1608.37	405.2	3.92 ± 0.25	9.67 ± 0.63	4.29 ± 0.76	44.13 ± 2.38	1
$6_{2,5}$–$6_{1,6}$	1608.60	405.2	3.94 ± 0.19	9.70 ± 0.50	6.37 ± 0.77	65.71 ± 2.65	1
$5_{5,0}$–$5_{2,3}$	1598.92	426.9	4.20 ± 0.81	15.48 ± 2.53	2.03 ± 0.72	33.40 ± 4.06	1
$6_{3,3}$–$6_{2,4}$	947.26	513.0	3.49 ± 0.10	11.16 ± 0.30	2.77 ± 0.18	32.92 ± 1.11	1
$6_{4,3}$–$5_{5,0}$	1879.36	517.1	4.28 ± 0.38	4.04 ± 0.82	2.18 ± 0.89	9.38 ± 1.75	1
$7_{1,6}$–$7_{0,7}$	1900.14	521.4	5.15 ± 0.80	5.96 ± 1.03	5.40 ± 0.87	34.27 ± 11.78	2

$7_{2,6}$–$7_{1,7}$	1900.18	521.4	4.76 ± 0.98	6.90 ± 1.91	5.13 ± 0.87	37.67 ± 12.77	2
$6_{5,2}$–$6_{4,3}$	854.97	558.1	3.63 ± 0.05	10.56 ± 0.13	3.36 ± 0.05	37.80 ± 0.53	1
$6_{5,1}$–$6_{4,2}$	493.36	563.9	4.78 ± 0.05	6.11 ± 0.18	0.52 ± 0.01	3.39 ± 0.17	1
$7_{2,5}$–$7_{1,6}$	1592.67	597.9	4.26 ± 0.19	9.24 ± 0.50	6.55 ± 0.88	64.44 ± 2.80	1
$7_{3,5}$–$7_{2,6}$	1593.97	597.9	2.31 ± 0.30	11.90 ± 0.75	4.52 ± 0.80	57.23 ± 3.09	1
$7_{4,3}$–$7_{3,4}$	880.06	701.1	4.40 ± 0.09	6.83 ± 0.36	1.77 ± 0.05	12.87 ± 1.34	1
$7_{5,3}$–$7_{4,4}$	1040.28	709.9	4.19 ± 0.10	8.13 ± 0.26	2.03 ± 0.15	17.59 ± 0.46	1
$8_{2,6}$–$8_{1,7}$	1882.52	741.5	4.65 ± 0.35	5.71 ± 0.86	2.44 ± 0.73	14.81 ± 1.85	1
$8_{3,6}$–$8_{2,7}$	1882.77	741.5	3.58 ± 0.28	8.70 ± 0.65	4.17 ± 0.81	38.58 ± 2.46	1
$7_{6,2}$–$7_{5,3}$	928.64	754.5	4.28 ± 0.04	8.20 ± 0.11	1.91 ± 0.06	16.67 ± 0.18	2
$7_{7,0}$–$7_{6,1}$	910.67	801.5	4.71 ± 0.08	7.05 ± 0.24	1.45 ± 0.06	10.91 ± 0.45	2
$8_{4,5}$–$8_{3,6}$	1576.44	817.1	3.31 ± 0.28	7.19 ± 0.67	4.24 ± 0.93	32.42 ± 2.56	1
$8_{5,3}$–$8_{4,4}$	804.73	914.2	4.72 ± 0.14	8.52 ± 0.38	0.76 ± 0.07	6.89 ± 0.25	1
$8_{6,3}$–$8_{5,4}$	1071.31	930.2	4.51 ± 0.07	8.53 ± 0.18	2.44 ± 0.14	22.16 ± 0.38	2
$8_{7,2}$–$8_{6,3}$	1019.45	979.1	4.92 ± 0.06	6.50 ± 0.23	1.23 ± 0.09	8.55 ± 0.61	1
$9_{3,6}$–$9_{2,7}$	1860.98	987.8	4.00 ± 0.36	6.35 ± 0.85	2.52 ± 0.74	17.03 ± 1.97	1
$8_{8,1}$–$8_{7,2}$	1091.26	1031.5	4.58 ± 0.12	7.13 ± 0.29	0.93 ± 0.08	7.07 ± 0.24	1
$9_{5,4}$–$9_{4,5}$	1154.68	1117.1	4.81 ± 0.35	8.09 ± 0.76	1.16 ± 0.14	10.01 ± 0.76	2
$9_{6,3}$–$9_{5,4}$	746.73	1152.9	5.09 ± 0.10	6.69 ± 0.23	0.65 ± 0.05	4.66 ± 0.13	2
$9_{7,2}$–$9_{6,3}$	689.12	1186.0	4.19 ± 0.09	7.49 ± 0.21	0.51 ± 0.03	4.03 ± 0.09	1
$9_{8,2}$–$9_{7,3}$	1122.64	1231.9	5.93 ± 0.31	5.38 ± 0.84	0.34 ± 0.09	1.95 ± 0.24	1
$9_{8,1}$–$9_{7,2}$	973.85	1232.7	5.28 ± 0.22	10.07 ± 0.48	0.56 ± 0.07	6.04 ± 0.30	2
			$H_2{}^{34}S$				
$2_{1,2}$–$1_{0,1}$	734.27	55.0	4.55 ± 0.15	10.15 ± 0.41	2.96 ± 0.04	32.02 ± 2.51	2
$2_{2,1}$–$1_{1,0}$	1069.37	79.2	3.73 ± 0.03	10.34 ± 0.12	4.00 ± 0.07	44.03 ± 0.86	2
$3_{0,3}$–$2_{1,2}$	991.73	102.7	3.99 ± 0.09	9.17 ± 0.23	3.49 ± 0.08	34.12 ± 1.16	2
$3_{1,3}$–$2_{0,2}$	1000.91	102.7	3.81 ± 0.05	7.58 ± 0.13	2.95 ± 0.08	23.82 ± 0.52	2
$3_{1,2}$–$2_{2,1}$	1197.18	136.7	3.74 ± 0.11	11.09 ± 0.46	3.45 ± 0.12	40.71 ± 3.10	2
$3_{2,2}$–$3_{1,3}$	745.52	138.5	3.91 ± 0.05	9.69 ± 0.10	1.30 ± 0.04	13.42 ± 0.01	1
$3_{3,1}$–$3_{2,2}$	563.68	165.5	4.72 ± 0.16	5.22 ± 0.49	0.33 ± 0.02	1.85 ± 0.26	1
$3_{3,1}$–$2_{2,0}$	1702.01	165.6	4.00 ± 0.27	7.91 ± 0.64	3.46 ± 0.62	29.18 ± 1.99	1
$3_{3,0}$–$2_{2,1}$	1861.85	168.6	4.95 ± 0.24	7.16 ± 0.59	4.26 ± 0.76	32.45 ± 2.23	1
$4_{2,3}$–$4_{1,4}$	1024.85	213.2	4.68 ± 0.07	7.29 ± 0.29	1.74 ± 0.11	13.53 ± 0.91	2
$4_{2,3}$–$3_{1,2}$	1595.98	213.3	4.78 ± 0.22	9.38 ± 0.59	5.44 ± 0.77	54.33 ± 2.76	1
$4_{2,2}$–$4_{1,3}$	666.82	244.9	4.54 ± 0.11	8.37 ± 0.29	0.87 ± 0.03	7.77 ± 0.31	2
$4_{2,2}$–$3_{3,1}$	1653.14	244.9	3.32 ± 0.72	10.84 ± 1.98	1.87 ± 0.59	21.53 ± 2.80	1

$4_{4,1}$–$4_{3,2}$	643.59	280.7	4.70 ± 0.08	8.02 ± 0.24	1.21 ± 0.03	10.30 ± 0.39	2
$5_{1,4}$–$4_{2,3}$	1849.96	302.1	3.95 ± 0.28	7.67 ± 0.66	3.98 ± 0.82	32.44 ± 2.35	1
$5_{2,4}$–$4_{1,3}$	1859.05	302.1	5.61 ± 0.23	4.71 ± 0.70	2.98 ± 0.63	14.96 ± 1.63	1
$6_{0,6}$–$5_{1,5}$	1843.77	327.5	3.75 ± 0.21	7.91 ± 0.44	4.45 ± 0.75	37.42 ± 0.54	3
$5_{3,3}$–$5_{2,4}$	1021.31	351.1	4.50 ± 0.53	7.17 ± 0.65	0.90 ± 0.07	6.90 ± 1.76	2
$5_{3,2}$–$5_{2,3}$	613.83	379.1	4.47 ± 0.05	8.29 ± 0.14	0.91 ± 0.02	8.01 ± 0.10	2
$5_{4,2}$–$5_{3,3}$	796.54	389.3	4.03 ± 0.11	6.18 ± 0.30	0.44 ± 0.04	2.91 ± 0.11	2
$6_{3,3}$–$6_{2,4}$	949.42	512.4	4.89 ± 0.20	6.22 ± 0.46	0.35 ± 0.05	2.30 ± 0.15	1
$6_{4,3}$–$6_{3,4}$	1023.49	516.3	4.94 ± 0.07	6.76 ± 0.18	1.10 ± 0.06	7.95 ± 0.18	1
$6_{4,2}$–$6_{3,3}$	568.82	539.7	3.41 ± 0.32	5.53 ± 0.57	0.12 ± 0.03	0.68 ± 0.07	2
$6_{5,2}$–$6_{4,3}$	848.36	557.0	4.15 ± 0.15	5.91 ± 0.41	0.43 ± 0.06	2.72 ± 0.15	1
$7_{4,3}$–$7_{3,4}$	884.52	700.4	4.80 ± 0.09	6.84 ± 0.22	0.41 ± 0.03	2.99 ± 0.09	1
				$H_2{}^{33}S$			
$2_{0,2}$–$1_{1,1}$	687.16	54.7	5.98 ± 0.05	9.22 ± 0.12	0.73 ± 0.02	7.13 ± 0.08	2
$2_{1,2}$–$1_{0,1}$	735.13	55.1	4.65 ± 0.02	9.52 ± 0.09	1.60 ± 0.02	16.23 ± 0.27	2
$2_{2,1}$–$1_{1,0}$	1071.05	79.3	4.27 ± 0.05	8.23 ± 0.11	2.18 ± 0.07	19.12 ± 0.23	2
$3_{0,3}$–$2_{1,2}$	992.40	102.7	4.24 ± 0.10	10.41 ± 0.33	2.70 ± 0.05	29.97 ± 1.47	1
$4_{0,4}$–$3_{1,3}$	1279.28	164.2	4.82 ± 0.32	8.15 ± 1.00	1.55 ± 0.37	13.45 ± 1.21	1
$4_{2,3}$–$4_{1,4}$	1025.65	213.4	3.57 ± 0.12	10.16 ± 0.28	0.90 ± 0.05	9.71 ± 0.23	1
$4_{2,3}$–$3_{1,2}$	1597.81	213.4	3.88 ± 0.42	10.47 ± 1.16	2.64 ± 0.75	29.41 ± 2.55	1
$4_{4,1}$–$4_{3,2}$	646.87	281.1	2.75 ± 0.12	13.80 ± 0.30	0.36 ± 0.02	5.32 ± 0.09	1
$6_{0,6}$–$5_{1,5}$	1845.21	327.8	11.67 ± 0.42	7.53 ± 1.02	2.35 ± 0.79	18.85 ± 2.15	3

Errors for v_{lsr}, Δv, and $\int T_{mb} dv$ reported in the table are those computed by the Gaussian fitter within CLASS. The T_{peak} error is the RMS in the local baseline, which we also measured in CLASS. Additional sources of error for these measurements are discussed in Appendix C.

[a] Entries of 1 or 2 correspond to categories 1 (not blended) or 2 (slightly blended) as defined in Sec. 4.3.1 for a particular transition, respectively. A value of 3 is given to the $6_{0,6}$–$5_{1,5}$ transition because it is "self-blended" with the $6_{1,6}$–$5_{0,5}$ transition from the same H_2S isotopologue.

Table 4.2: Measured line parameters for the plateau

Transition (J_{K^-,K^+})	ν (GHz)	E_{up} (K)	v_{LSR} (km s^{-1})	Δv (km s^{-1})	T_{peak} (K)	$\int T_{mb} dv$ (K km s^{-1})	Notes[a]
			$H_2{}^{32}S$				
$2_{0,2}$–$1_{1,1}$	687.30	54.7	9.73 ± 0.14	34.46 ± 0.45	5.46 ± 0.03	200.35 ± 1.55	2
$2_{1,2}$–$1_{0,1}$	736.03	55.1	9.84 ± 0.01	30.59 ± 0.03	10.62 ± 0.04	345.72 ± 0.35	2
$2_{2,1}$–$2_{1,2}$	505.57	79.4	10.67 ± 0.59	31.59 ± 0.59	4.57 ± 0.02	153.72 ± 1.58	1
$2_{2,1}$–$1_{1,0}$	1072.84	79.4	11.36 ± 0.03	30.52 ± 0.06	11.56 ± 0.07	375.52 ± 0.67	1
$3_{1,3}$–$2_{0,2}$	1002.78	102.9	10.40 ± 0.01	29.76 ± 0.12	7.91 ± 0.10	250.62 ± 1.38	2
$3_{1,2}$–$2_{2,1}$	1196.01	136.8	10.16 ± 0.09	31.44 ± 0.16	8.84 ± 0.17	295.82 ± 1.97	1
$3_{2,2}$–$3_{1,3}$	747.30	138.7	7.80 ± 0.11	34.06 ± 0.24	3.74 ± 0.05	135.57 ± 1.07	2
$3_{3,1}$–$3_{2,2}$	568.05	166.0	7.59 ± 0.01	32.78 ± 0.12	2.02 ± 0.02	70.54 ± 0.25	1
$3_{3,1}$–$2_{2,0}$	1707.97	166.0	10.00 ± 0.01[b]	36.52 ± 1.21	4.80 ± 0.64	186.77 ± 4.96	1
$3_{3,0}$–$2_{2,1}$	1865.62	169.0	10.00 ± 0.01[b]	27.01 ± 1.48	3.42 ± 0.74	98.44 ± 6.15	1
$4_{1,3}$–$4_{0,4}$	1018.35	213.2	7.42 ± 0.24	31.57 ± 0.62	3.38 ± 0.09	113.71 ± 2.28	1
$4_{2,3}$–$3_{3,0}$	930.15	213.6	7.72 ± 0.12	31.79 ± 0.72	0.98 ± 0.06	33.03 ± 0.71	2
$4_{2,3}$–$4_{1,4}$	1026.51	213.6	5.89 ± 0.44	23.80 ± 0.44	6.76 ± 0.12	171.18 ± 1.97	2
$4_{2,3}$–$3_{1,2}$	1599.75	213.6	11.61 ± 0.72	34.74 ± 1.29	3.88 ± 0.60	143.51 ± 6.27	1
$4_{2,2}$–$4_{1,3}$	665.39	245.1	9.30 ± 0.45	32.13 ± 0.45	2.18 ± 0.05	74.72 ± 1.38	2
$4_{2,2}$–$3_{3,1}$	1648.71	245.2	2.21 ± 1.33	33.60 ± 2.31	3.23 ± 0.90	115.56 ± 12.46	2
$4_{3,2}$–$4_{2,3}$	765.94	250.3	10.93 ± 0.19	38.76 ± 0.64	5.27 ± 0.03	217.40 ± 2.54	2
$4_{4,1}$–$4_{3,2}$	650.37	281.5	7.94 ± 0.03	28.09 ± 0.07	2.91 ± 0.03	86.97 ± 0.28	1
$5_{1,4}$–$4_{2,3}$	1852.69	302.5	11.76 ± 1.31	32.07 ± 2.16	2.02 ± 0.68	68.86 ± 6.32	1
$6_{0,6}$–$5_{1,5}$	1846.74	328.1	10.19 ± 1.28	31.53 ± 1.58	2.97 ± 0.73	99.62 ± 8.95	3
$5_{3,3}$–$5_{2,4}$	1023.12	351.7	7.63 ± 0.01	30.83 ± 0.50	1.86 ± 0.11	61.08 ± 0.71	2
$5_{3,2}$–$5_{2,3}$	611.44	379.5	8.26 ± 0.41	33.48 ± 1.02	1.41 ± 0.02	50.20 ± 1.60	1
$5_{4,2}$–$5_{3,3}$	800.85	390.1	9.46 ± 0.56	35.68 ± 0.56	0.85 ± 0.09	32.22 ± 1.28	2
$6_{3,3}$–$6_{2,4}$	947.26	513.0	17.06 ± 0.99	43.29 ± 1.47	0.77 ± 0.18	35.44 ± 1.55	1
$6_{5,2}$–$6_{4,3}$	854.97	558.1	6.86 ± 0.35	31.10 ± 0.91	0.90 ± 0.05	29.92 ± 0.19	1
$6_{5,1}$–$6_{4,2}$	493.36	563.9	2.42 ± 0.12	18.54 ± 0.31	0.45 ± 0.01	8.84 ± 0.17	1
$7_{4,3}$–$7_{3,4}$	880.06	701.1	2.49 ± 0.19	20.04 ± 0.89	1.52 ± 0.05	32.49 ± 1.18	1
			$H_2{}^{34}S$				
$2_{1,2}$–$1_{0,1}$	734.27	55.0	7.89 ± 0.14	33.78 ± 0.58	2.92 ± 0.04	105.11 ± 0.89	2
$2_{2,1}$–$1_{1,0}$	1069.37	79.2	8.77 ± 0.13	29.51 ± 0.23	2.42 ± 0.07	75.93 ± 0.94	2
$3_{0,3}$–$2_{1,2}$	991.73	102.7	7.66 ± 0.28	28.73 ± 0.32	2.63 ± 0.08	80.38 ± 2.35	2

$3_{1,3}$–$2_{0,2}$	1000.91	102.7	4.58 ± 0.12	29.92 ± 0.35	1.98 ± 0.08	62.90 ± 0.64	2
$3_{1,2}$–$2_{2,1}$	1197.18	136.7	8.47 ± 0.55	31.82 ± 1.30	1.67 ± 0.12	56.56 ± 3.48	2
$3_{2,2}$–$3_{1,3}$	745.52	138.5	9.00 ± 0.01[b]	25.13 ± 1.15	0.25 ± 0.04	6.63 ± 0.24	1
$3_{3,1}$–$3_{2,2}$	563.68	165.5	2.93 ± 0.31	18.63 ± 0.99	0.32 ± 0.02	6.33 ± 0.28	1
$4_{2,3}$–$4_{1,4}$	1024.85	213.2	3.17 ± 0.17	22.56 ± 0.72	1.21 ± 0.11	29.04 ± 0.86	2
				$H_2{}^{33}S$			
$2_{1,2}$–$1_{0,1}$	735.13	55.1	5.72 ± 0.05	28.49 ± 0.20	1.32 ± 0.02	40.14 ± 0.27	2
$3_{0,3}$–$2_{1,2}$	992.40	102.7	8.20 ± 0.62	35.64 ± 1.56	0.89 ± 0.05	33.77 ± 1.34	1

Errors for v_{lsr}, Δv, and $\int T_{mb} dv$ reported in the table are those computed by the Gaussian fitter within CLASS. The T_{peak} error is the RMS in the local baseline, which we also measured in CLASS. Additional sources of error for these measurements are discussed in Appendix C.

[a] Entries of 1 or 2 correspond to categories 1 (not blended) or 2 (slightly blended) as defined in Sec. 4.3.1 for a particular transition, respectively. A value of 3 is given to the $6_{0,6}$–$5_{1,5}$ transition because it is "self-blended" with the $6_{1,6}$–$5_{0,5}$ transition from the same H_2S isotopologue.

[b] The v_{lsr} was held fixed during the Gaussian fitting procedure.

Table 4.3: Measured line parameters for the extended/compact ridge

Transition (J_{K^-,K^+})	ν (GHz)	E_{up} (K)	v_{LSR} (km s^{-1})	Δv (km s^{-1})	T_{peak} (K)	$\int T_{mb} dv$ (K km s^{-1})	Notes[a]
			$H_2{}^{32}S$				
$2_{0,2}$–$1_{1,1}$	687.30	54.7	8.46 ± 0.06	3.17 ± 0.22	2.25 ± 0.03	7.62 ± 0.85	2
$2_{1,2}$–$1_{0,1}$	736.03	55.1	8.68 ± 0.01	3.29 ± 0.02	3.35 ± 0.04	11.71 ± 0.04	2
$2_{2,1}$–$2_{1,2}$	505.57	79.4	8.59 ± 0.59	3.09 ± 0.59	1.95 ± 0.02	6.41 ± 1.58	1
$2_{2,1}$–$1_{1,0}$	1072.84	79.4	8.52 ± 0.06	3.54 ± 0.13	1.70 ± 0.07	6.41 ± 0.26	1
$3_{1,3}$–$2_{0,2}$[c]	1002.78	102.9	8.84 ± 0.01	10.89 ± 0.46	1.56 ± 0.10	18.09 ± 1.64	2
			$H_2{}^{34}S$				
$3_{1,3}$–$2_{0,2}$	1000.91	102.7	4.80 ± 0.05	3.43 ± 0.08	1.97 ± 0.08	7.18 ± 0.11	2

Errors for v_{lsr}, Δv, and $\int T_{mb} dv$ reported in the table are those computed by the Gaussian fitter within CLASS. The T_{peak} error is the RMS in the local baseline, which we also measured in CLASS. Additional sources of error for these measurements are discussed in Appendix C.

[a] Entries of 1 or 2 correspond to categories 1 (not blended) or 2 (slightly blended) as defined in Sec. 4.3.1 for a particular transition, respectively.

[c] The extended ridge component for this transition is not fit well because of its relative weakness and line blending.

Table 4.4: Computed values for τ_{iso} and $N_{up}(H_2{}^{32}S)$

Transition (J_{K^-,K^+})	τ_{iso}	N_u (Solar) ($\times 10^{16}$ cm^{-2})	N_u (Orion KL) ($\times 10^{16}$ cm^{-2})	iso[a]
$2_{0,2}$–$1_{1,1}$	0.25 ± 0.04	4.27 ± 1.36	2.56 ± 0.82	$H_2{}^{33}S$
$2_{1,2}$–$1_{0,1}$	1.18 ± 0.32	9.00 ± 3.46	5.40 ± 2.08	$H_2{}^{33}S$
$2_{2,1}$–$1_{1,0}$	1.02 ± 0.27	5.84 ± 2.46	3.51 ± 1.48	$H_2{}^{33}S$
$3_{1,3}$–$2_{0,2}$	1.61 ± 0.60	2.52 ± 1.23	2.28 ± 1.11	$H_2{}^{34}S$
$3_{1,2}$–$2_{2,1}$	0.89 ± 0.22	3.18 ± 1.42	2.88 ± 1.29	$H_2{}^{34}S$
$3_{2,2}$–$3_{1,3}$	0.45 ± 0.08	2.12 ± 0.70	1.92 ± 0.63	$H_2{}^{34}S$
$3_{3,1}$–$3_{2,2}$	0.24 ± 0.04	0.66 ± 0.20	0.60 ± 0.18	$H_2{}^{34}S$
$3_{3,1}$–$2_{2,0}$	0.88 ± 0.38	1.03 ± 0.79	0.93 ± 0.71	$H_2{}^{34}S$
$4_{2,3}$–$4_{1,4}$	0.52 ± 0.11	1.70 ± 0.65	1.53 ± 0.59	$H_2{}^{34}S$
$4_{2,3}$–$4_{1,4}$	0.23 ± 0.04	4.31 ± 1.59	2.59 ± 0.95	$H_2{}^{33}S$
$4_{2,3}$–$3_{1,2}$	1.76 ± 1.13	3.61 ± 3.08	3.26 ± 2.78	$H_2{}^{34}S$
$4_{2,3}$–$3_{1,2}$	0.51 ± 0.23	5.95 ± 4.27	3.57 ± 2.56	$H_2{}^{33}S$
$4_{2,2}$–$4_{1,3}$	0.38 ± 0.07	1.20 ± 0.39	1.09 ± 0.35	$H_2{}^{34}S$
$4_{2,2}$–$3_{3,1}$	0.34 ± 0.15	1.67 ± 1.26	1.51 ± 1.14	$H_2{}^{34}S$
$4_{4,1}$–$4_{3,2}$	0.71 ± 0.15	2.28 ± 0.76	2.06 ± 0.69	$H_2{}^{34}S$
$4_{4,1}$–$4_{3,2}$	0.16 ± 0.03	3.00 ± 0.94	1.80 ± 0.56	$H_2{}^{33}S$
$5_{1,4}$–$4_{2,3}$	1.01 ± 0.51	2.01 ± 1.78	1.82 ± 1.61	$H_2{}^{34}S$
$5_{2,4}$–$4_{1,3}$	0.61 ± 0.25	1.30 ± 1.08	1.17 ± 0.98	$H_2{}^{34}S$
$5_{3,3}$–$5_{2,4}$	0.22 ± 0.04	0.64 ± 0.23	0.58 ± 0.21	$H_2{}^{34}S$
$5_{3,2}$–$5_{2,3}$	0.48 ± 0.09	1.29 ± 0.42	1.17 ± 0.38	$H_2{}^{34}S$
$5_{4,2}$–$5_{3,3}$	0.16 ± 0.03	0.37 ± 0.12	0.34 ± 0.11	$H_2{}^{34}S$
$6_{3,3}$–$6_{2,4}$	0.13 ± 0.03	0.24 ± 0.08	0.22 ± 0.08	$H_2{}^{34}S$
$6_{5,2}$–$6_{4,3}$	0.14 ± 0.03	0.32 ± 0.11	0.30 ± 0.10	$H_2{}^{34}S$
$7_{4,3}$–$7_{3,4}$	0.26 ± 0.05	0.17 ± 0.06	0.15 ± 0.05	$H_2{}^{34}S$

[a] This column indicates the isotopologue used to compute τ_{iso}.

Table 4.5: Ortho/Para Ratio Estimates

Ortho State	Para State	Ortho/Para Ratio
$2_{1,2}$	$2_{0,2}$	2.1 ± 1.1
$3_{1,2}$	$3_{2,2}$	1.5 ± 0.8
$5_{1,4}$	$5_{2,4}$	1.6 ± 1.9

The first two columns indicate the ortho and para state from which an N_{up} estimate was taken in order to compute the ortho/para ratio in the third column.

Table 4.6: Transitions Used for N_{tot}(HDS) Upper Limit

Transition (J_{K^-,K^+})	ν_{rest} (GHz)	E_{up} (K)	μ^2S (D^2)	Local RMS[a] (K)
$2_{2,0}$–$1_{1,1}$	1035.61	68.4	0.75	0.084
$3_{1,3}$–$2_{0,2}$	754.96	70.9	1.27	0.045
$3_{0,3}$–$2_{1,2}$	586.90	67.8	1.01	0.028
$3_{2,2}$–$2_{1,1}$	1166.00	103.0	0.99	0.15
$3_{2,2}$–$2_{2,1}$	732.73	103.0	0.60	0.022
$4_{1,4}$–$3_{0,3}$	920.50	112.0	1.77	0.047

[a] The RMS was computed using CLASS in the vicinity of the rest frequency.

CHAPTER 5

Chemical Implications

5.1 Introduction

Massive star forming regions stand out as being the most chemically rich environments in the Milky Way, harboring high abundances of complex organics. Though the chemistry in these regions remains poorly understood, chemical reactions on grain surfaces are now believed to be important, in part, because purely gas phase networks fail to reproduce observed abundance levels of key complex organics (Herbst & van Dishoeck, 2009). Present models indicate that the chemical evolution of hot cores is highly coupled to the thermal history. Before the formation of an embedded protostar, dust grains build up icy mantles (Garrod & Herbst, 2006; Garrod et al., 2008). Once an embedded protostar forms, a so-called "warm up" phase occurs in which the star heats the surrounding material to temperatures of 100 – 300 K driving chemical reactions on grain surfaces that are inefficient at lower temperatures and evaporating molecules into the gas phase. Molecules removed from grain surfaces in what is now a hot core participate in a hot gas phase chemistry. Eventually, ice mantels are completely evaporated and only gas phase reactions govern the chemical evolution.

In Chapter 3, we presented a full band analysis of the *Herschel*/HIFI 1.2 THz wide spectral survey toward the Orion Kleinmann-Low nebula (Orion KL), one of the brightest massive star forming regions in the Milky Way. This dataset provides near continuous spectral coverage from 480 to 1907 GHz at high spectral resolution (1.1 MHz). As part of that analysis, we modeled the molecular emission assuming local thermodynamic equilibrium, deriving robust abundances and rotation temperatures for most of the species observed in the HIFI scan. Of the 36 molecules detected

in the HIFI spectrum, 8 are complex and include both O and N-bearing species. We consider molecules with 6 atoms or more to be complex species, following the definition of Herbst & van Dishoeck (2009). In this chapter, we identify the molecules emitting in the hottest gas and discuss the chemical implications focusing on the complex organics.

This chapter is organized as follows. In Sec. 5.2, we review the LTE models fit to the Orion KL HIFI spectral scan. In Sec. 5.3, we identify those species emitting in the hottest gas. We discuss our results in Sec. 5.4, and present our conclusions in Sec. 5.5.

5.2 Observations and The Full Band Model

The full HIFI spectral survey of Orion KL is presented in Chapter 3. These data were obtained using the HIFI wide band spectrometer (WBS) on board the *Herschel* Space Observatory. The survey covers a frequency range from 480 to 1907 GHz with two gaps at 1280 – 1430 GHz and 1540 – 1570 GHz, respectively, at a spectral resolution of 1.1 MHz. Specific details concerning how the observations were taken and how the data were reduced are given in Secs. 3.2 and 4.2.

We fit model spectra to the molecular line emission within the HIFI survey using the XCLASS program, which assumes local thermodynamic equilibrium (LTE). The specific methodology we used to fit models to the data is described in Sec. 3.3. In total, we detect emission from 76 isotopologues originating from 36 molecules, each of which has its own molecular fit. Summing the modeled emission from all detected species yields the "full band" model. Our fits were also constrained at mm wavelengths using a ground based spectral survey obtained with the IRAM 30 m telescope which covers frequency ranges 80 – 116 GHz, 130 – 180 GHz, and 200 – 280 GHz. This survey along with details concerning the data reduction and how the observations were taken are presented in Tercero et al. (2010). The LTE models are thus constrained from mm to far-IR wavelengths and, in almost all cases, include low energy transitions (i.e. at or close to the ground state) up to energies were emission is no longer detected.

In this chapter, we use our molecular fits as a templates for the data, analyzing

the emission from the models rather than the data itself. Examining the HIFI scan in this way has two advantages. First, we are able to easily separate emission from different spatial/velocity components. And second, we do not have to worry about line blends because we are able to examine the emission on a per molecule basis.

5.3 Results

Rotation temperatures are useful metrics by which to characterize molecular emission. In Sec. 3.6, we plotted the distribution of rotation temperatures toward each spatial/velocity component, which showed that the hot core has a relatively wide T_{rot} distribution compared to the compact ridge, plateau, and extended ridge. Cyanides, furthermore, made up a large fraction of the molecules with $T_{rot} > 200$ K toward the hot core.

Another metric we employ here to characterize the emission is summing the integrated intensity from all T_{rot} sub-components and vibrationally excited modes for a given molecule and using it directly as a diagnostic. Those molecules emitting a larger fraction of their total line radiation from higher energy states, represent the most highly excited molecules within Orion KL and likely originate from the hottest gas. We emphasize that this metric is independent of rotation temperature and relies solely on the observed emission as predicted by our models which, according to the reduced χ^2 analysis presented in Sec. 3.4.1, generally agree quite well with the data.

For each molecule, we computed the fraction of total integrated intensity originating from states with E_{up} in ranges 0 – 200 K, 200 – 800 K, and 800 – 3000 K. Fig. 5.1, 5.2, and 5.3 plot the fractional emission from these E_{up} bins as pie charts for molecules detected toward the hot core, compact ridge, and plateau, respectively. We do not discuss emission from the extended ridge here because no complex organics were detected toward this component. The dark blue, cyan, and red slices correspond to the 0 – 200 K, 200 – 800 K, and 800 – 3000 K energy bins, respectively. Molecules displaying the most highly excited emission are readily apparent because a significant fraction of their line radiation originates from states with $E_{up} > 800$ K (red slice). The top of each panel gives the molecule represented in the pie chart. If a pie chart

includes a vibrationally excited mode fit separately in the full band model, it is indicated in the panel label. In instances when more than one isotopologue is detected for a given molecule, we represent the emission using a rarer species to avoid issues with high optical depth. However, when vibrationally excited modes are only detected in more abundant isotopologues (e.g. CH_3CN, SO_2, etc.), we adopt those spectra for Figs. 5.1 – 5.3 so that emission from vibrationally excited modes can be included in the pie charts. For the sake of simplicity in the following text, we use only main isotopologue names even if the pie chart for a particular molecule was made using the spectrum of a rarer species. The rotation temperature of the hottest component in the ground vibrational state for each species is also given in the lower right corner of each panel.

From Fig. 5.1, we see that all cyanide molecules detected toward the hot core display highly excited emission. This includes HCN, HNC, and HC_3N, as well as the complex organics CH_3CN, C_2H_3CN, and C_2H_5CN. The complex oxygen bearing species CH_3OH and CH_3OCH_3, on the other hand, are not as highly excited ($T_{rot} < 150$ K). Fig. 5.2 shows similar trends in the compact ridge. CH_3CN displays hot emission, while CH_3OH and CH_3OCH_3 are warm ($T_{rot} = 110$ – 140 K). The other complex O-bearing organics observed toward the compact ridge, C_2H_5OH and CH_3OCHO, are also warm ($T_{rot} = 110$ K) indicating they probe similar material. NH_2CHO, detected only toward the compact ridge, is quite hot ($T_{rot} = 190$ K). From Fig. 5.3, we see that CH_3CN, the only complex organic detected toward the plateau, displays the most highly excited spectrum as represented by the pie charts. We note that this is largely a result of including emission from the $\nu_8 = 1$ vibrationally excited mode.

5.4 Discussion

Our results indicate that complex cyanides along with NH_2CHO probe hotter environments than complex O-bearing organics. Recent gas-grain chemical models have shown that many complex O-bearing organics such as CH_3OCHO and CH_3OCH_3 can form efficiently on dust grains via reactions between heavy radicals during a hot core's

warm up phase (Garrod & Herbst, 2006; Garrod et al., 2008). If complex N-bearing molecules form via similar mechanisms, cyanides along with NH_2CHO may be more difficult to remove from grain surfaces than complex O-bearing organics. Within a hot core, we might then expect oxygen bearing organics to be released during an earlier, presumably cooler, epoch and/or further from the central protostar.

Previous observational studies have investigated possible differentiation between O and N-bearing organics toward other hot cores. Using single dish spectroscopic observations in the mm and sub-mm, Bisschop et al. (2007) computed the abundance and rotation temperatures for several O and N-bearing organics toward a sample of 7 hot cores. They found that the abundances between the complex "hot", which they define as $T_{rot} > 100$ K, O-bearing species CH_3OCH_3, CH_3OH, C_2H_5OH, CH_3OCHO, and H_2CO correlated with one another. However, abundances between the oxygen bearing and the N-bearing molecules HNCO and NH_2CHO, both of which trace hotter gas than the O-rich organics toward Orion KL (Fig. 5.1 and 5.2, respectively), did not correlate. Bisschop et al. (2007) argue that these results indicate that complex O and N-bearing organics originate from grain surface chemistries that are not strongly coupled to one another. Conversely, Fontani et al. (2007) carried out a similar study focusing on C_2H_5CN, C_2H_3CN, and CH_3OCH_3 using a sample of 6 hot cores. They found that abundances for all three species correlated with one another indicating that a simple oxygen/nitrogen chemical dichotomy is likely an over simplification.

Hot gas phase chemistry may also be producing the highly excited cyanides in the hot core. Wang et al. (2010), for example, argue that CH_3CN in the hot core likely forms in the gas based on the chemical models of Rodgers & Charnley (2001). These models show that at high temperatures ($T_{kin} = 300$ K), hot cores will produce CH_3CN, HC_3N and HCN in the gas phase at observed abundance levels on timescales of $\lesssim 10^5$ – 10^6 years. Similar models presented by Caselli et al. (1993) show similar results. In this scenario, cyanides naturally trace hotter material because they form efficiently in the gas phase at high temperatures. The highly excited cyanides observed toward the hot core in the HIFI scan may therefore be a result of such a high temperature gas phase chemistry.

5.5 Conclusions

In Chapter 3, we presented the full *Herschel*/HIFI 1.2 THz wide spectral survey of Orion KL along with LTE model spectra. In this chapter, we identify the complex organics that are emitting in the hottest gas. All of the cyanide molecules detected toward the hot core trace hot gas. These species include the complex organics CH_3CN, C_2H_3CN, and C_2H_5CN. The complex oxygen bearing species CH_3OH and CH_3OCH_3 are cooler toward the hot core but still trace gas with $T_{rot} \geq 100$ K. Hot gas tracers toward the compact ridge are CH_3CN and NH_2CHO. The oxygen bearing species CH_3OH, C_2H_5OH, CH_3OCH_3, and CH_3OCHO are less excited toward the compact ridge, displaying excitation levels similar to the oxygen bearing organics in the hot core. The only complex organic detected toward the plateau, CH_3CN, is also markedly hot compared to the other plateau molecules. If complex organics form on grain surfaces, our results may indicate that complex N-bearing molecules are more difficult to remove from grain surfaces than O-bearing species. The hot cyanides detected toward the hot core could possibly be explained by hot gas phase chemistry.

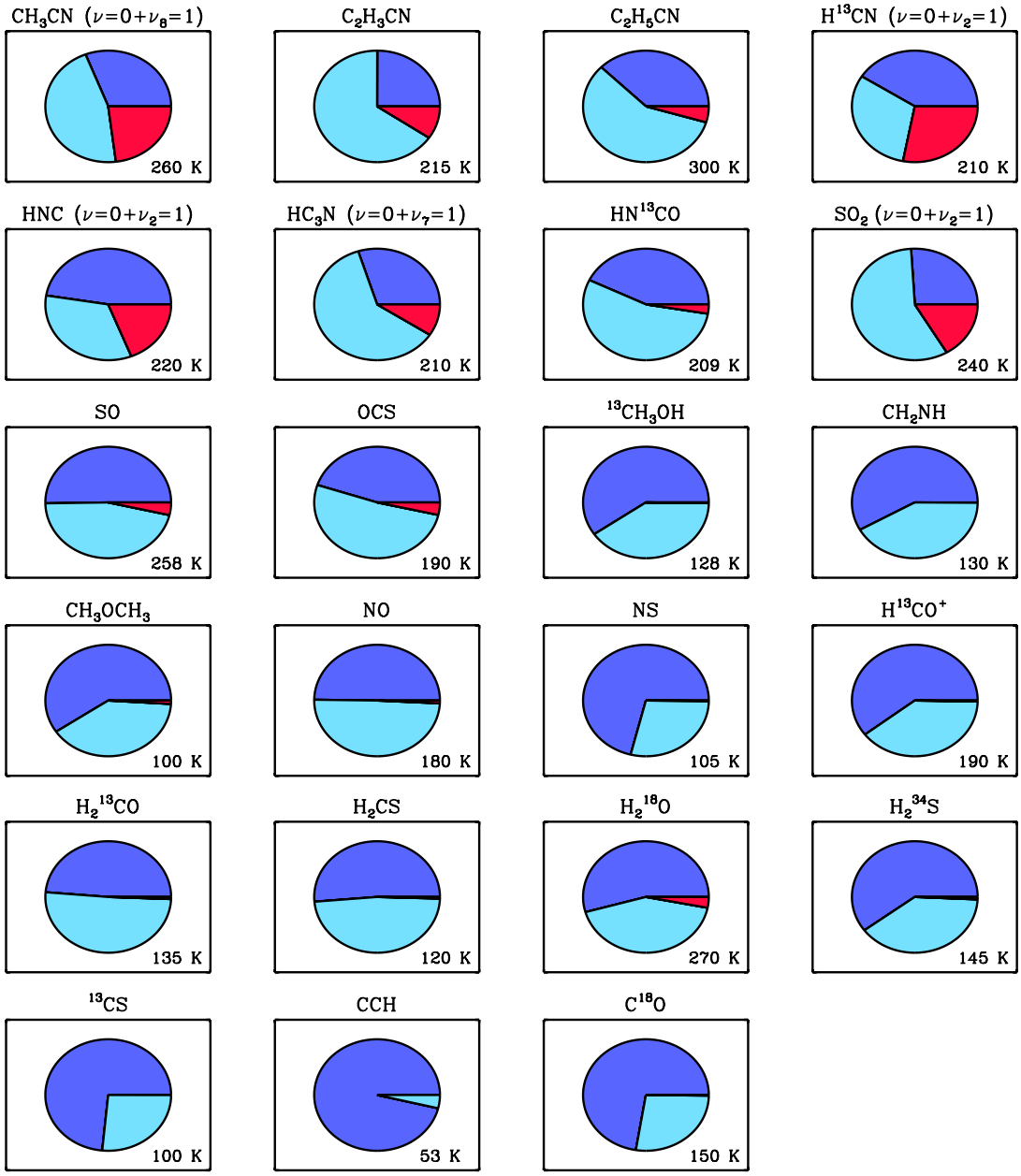

Figure 5.1: Pie charts plot the fraction of total integrated intensity originating from states in E_{up} ranges 0 – 200 K (dark blue), 200 – 800 K (cyan), and 800 – 3000 K (red) for molecules detected toward the hot core. The molecule ID is given at the top of each chart and the derived rotation temperature from Table 3.4 is given in the bottom right-hand corner of each panel.

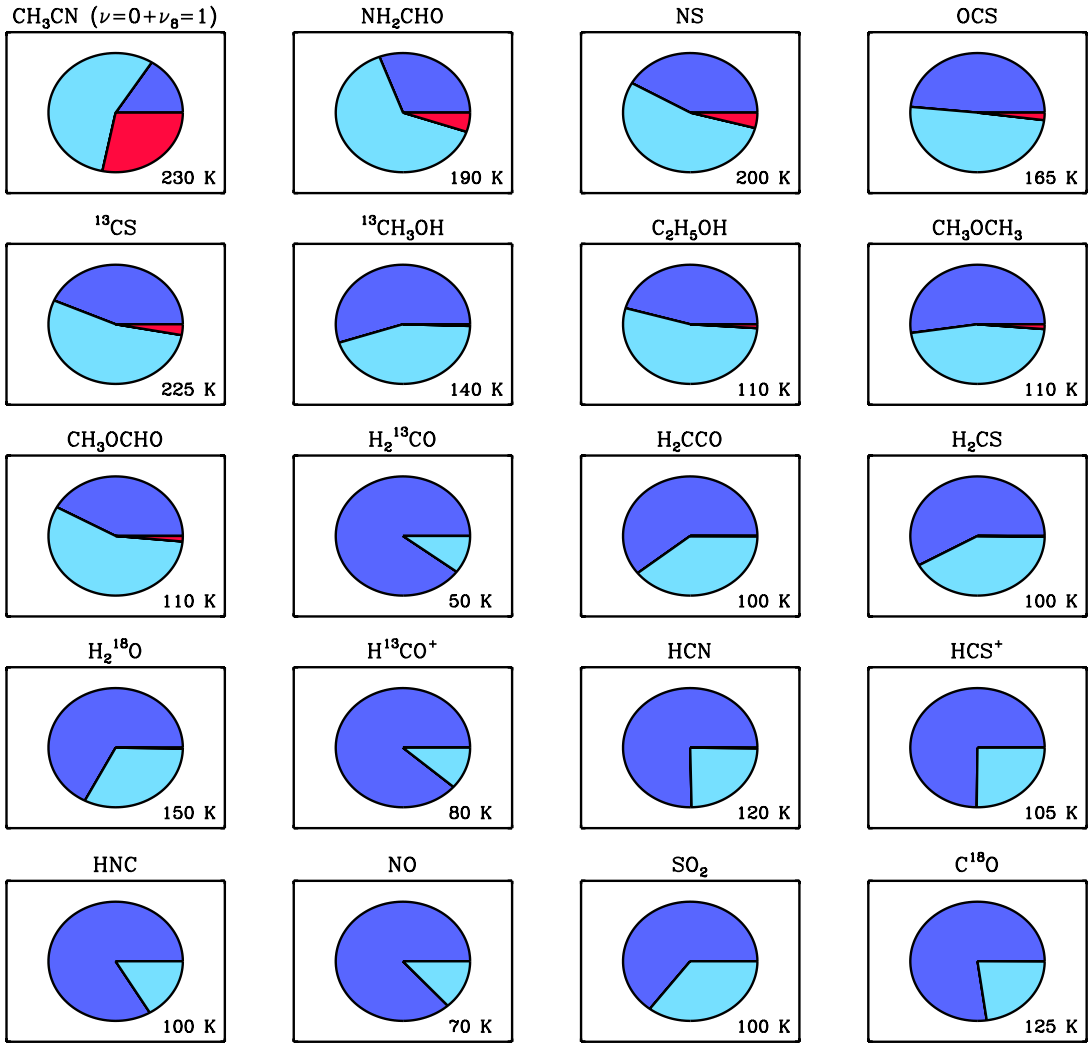

Figure 5.2: Pie charts plot the fraction of total integrated intensity originating from states in E_{up} ranges 0 – 200 K (dark blue), 200 – 800 K (cyan), and 800 – 3000 K (red) for molecules detected toward the compact ridge. The molecule ID is given at the top of each chart and the derived rotation temperature from Table 3.4 is given in the bottom right-hand corner of each panel.

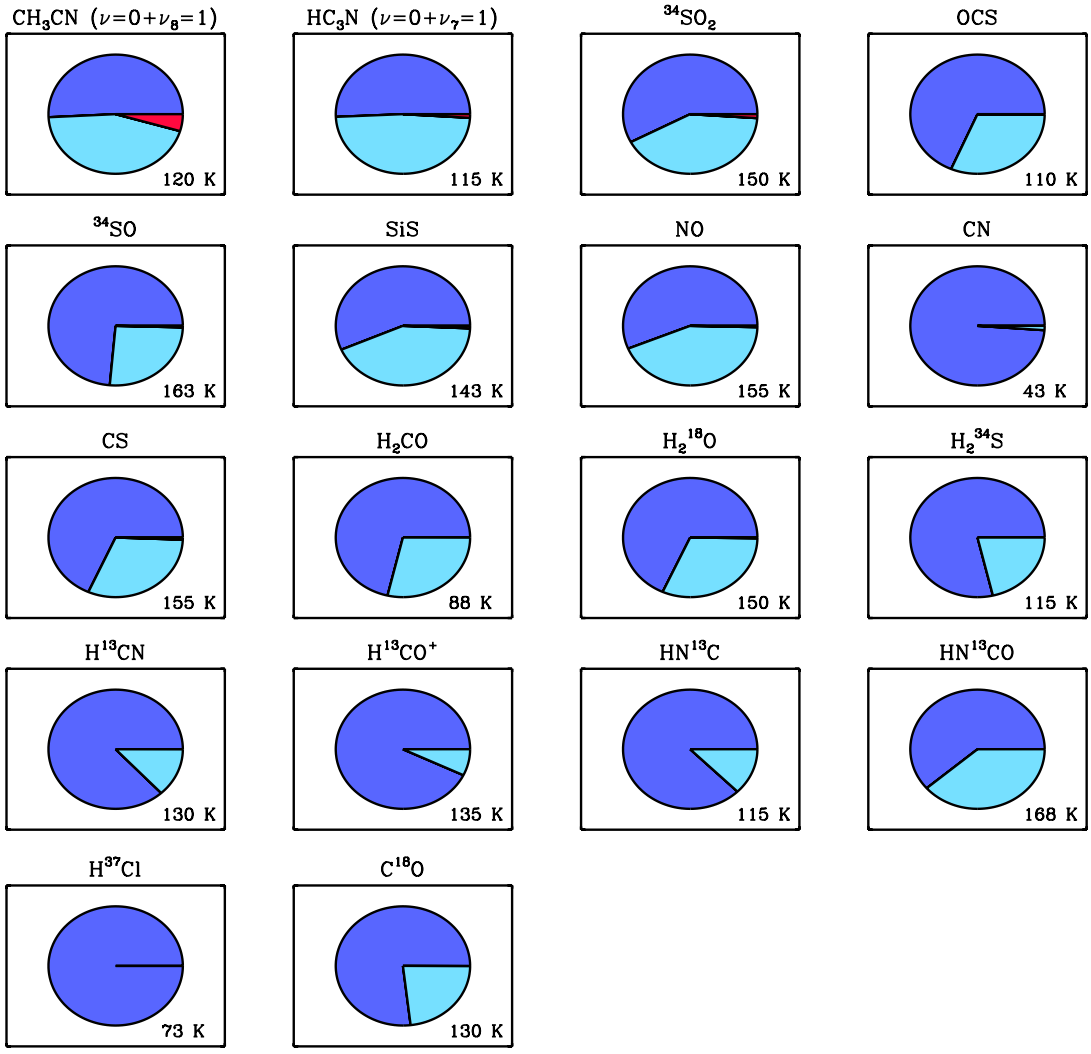

Figure 5.3: Pie charts plot the fraction of total integrated intensity originating from states in E_{up} ranges 0 – 200 K (dark blue), 200 – 800 K (cyan), and 800 – 3000 K (red) for molecules detected toward the plateau. The molecule ID is given at the top of each chart and the derived rotation temperature from Table 3.4 is given in the bottom right-hand corner of each panel.

CHAPTER 6

Conclusions and Future Prospects

6.1 Summary and Conclusions

6.1.1 Orion KL as Seen from Millimeter to Far-IR Wavelengths

The HIFI instrument, which is no longer in operation, represented a huge leap forward in our ability to view the universe at high spectral resolution from sub-mm to far-IR wavelengths. One of the major advantages of this instrument was that broad band line surveys could be obtained in relatively short amounts of time over unprecedented frequency intervals. The line survey presented in this dissertation is one of those datasets, pointed toward one of the most line rich sources in the Galaxy: Orion KL. Because of the overabundance of detected lines relative to previous surveys, new methodologies had to be developed to analyze the data which are presented in this dissertation.

HIFI provided sensitivity at frequencies beyond 1 THz, which is completely inaccessible from the ground due to atmospheric absorption. Observations at these frequencies thus represented new territory for high resolution spectral studies. In Chapter 2, I presented initial analysis of bands 6b and 7b, which cover frequencies ranges 1573 – 1703 and 1788 – 1907 GHz, respectively. These observations were the first high resolution spectra obtained toward Orion KL in the far-IR. We found that the line density in these regions is diminished relative to the sub-mm HIFI bands. This is largely a result of the drop off in the number of emissive transitions from complex organics which dominate the spectrum at lower frequencies. Higher dust optical depth in the far-IR may play a role in the lower line density, as well. In spite of this, we found that bands 6b and 7b contained strong ($T_{peak} > 7$ K) lines of CO,

H_2O, HDO, OH, CH_3OH, H_2S, HCN, and NH_3.

In Chapter 3, I presented a global analysis of the full Orion KL HIFI spectral scan. In order to constrain the emission at mm wavelengths, we combined the HIFI scan with another spectral survey presented by Tercero et al. (2010). We then fit LTE model spectra to the observed emission. For some species, multiple temperature sub-components were required to fit the observed emission indicating the presence of temperature gradients. This was only required for the hot core and plateau, while the extended ridge and compact ridge were always well fit by a single temperature component. We also identified a potentially new spatial/velocity component toward Orion KL, hot core (s), which was previously noted by Neill et al. (2013) to be associated with an HDO clump approximately 1″ south of the hot core. This component has line parameters in between that of the hot core and compact ridge, $v_{lsr} \sim 6.5$ – 8 km/s and $\Delta v \sim 5$ – 10 km/s.

Because of the wide frequency coverage, almost every molecule detected in the survey was constrained from states at or close to ground up to excitation energies that were no longer emissive. This was true not only for the complex organics, which sometimes had > 1000 observed transitions, but also for lighter species. Near complete J ladders were observed for most of the detected linear rotors (e.g. CO, HCN, etc.). The THz bands, moreover, contained many transitions of light hydrides such as H_2O that cannot be observed from the ground. This global view of the excitation allowed us to derive robust rotation temperatures and molecular abundances, which are valuable constraints on increasingly intricate chemical models that trace the chemical evolution of hot cores (Garrod & Herbst, 2006; Garrod et al., 2008).

In order to quantitatively determine which models reproduced the data best, we performed a reduced χ^2 analysis. These calculations revealed, for the most part, excellent agreement between the models and data. The complex organics, in particular, fit the data well, with most species having $\chi^2_{red} \lesssim 1.5$. LTE is thus a good approximation for these species, indicating the presence of dense ($n_{H_2} > 10^6$ cm^{-3}) gas. If the Orion KL hot core and compact ridge represent typical conditions toward massive star forming regions, analogous studies of complex organics toward other hot cores

may not require non-LTE methods to reproduce the emission.

Plotting the distribution of rotation temperatures toward the different spatial velocity components showed that the T_{rot} distribution toward the hot core was much wider compared to the other spatial velocity components, indicating a more heterogeneous thermal structure. The compact ridge T_{rot} distribution also had a conspicuous high temperature tail. Using the ALMA science verification dataset, we mapped two species, OCS and CS, present in this tail. This revealed a spatial structure significantly different than that traced by CH_3OCHO, a prominent compact ridge tracer with a rotation temperature that lies within the main T_{rot} distribution ($T_{rot} = 110$ K). Both OCS and CS peak closer to where the LVF and compact ridge intersect, suggesting the higher T_{rot} values for these species may be a result of an interaction between the LVF and compact ridge.

6.1.2 H_2S: A Possible Probe of Hidden Luminosity Toward Orion KL

In Chapter 4, I presented a detailed non-LTE analysis of H_2S emission toward the Orion KL hot core. In total, we observe 52, 24, and 8 unblended or slightly blended features from $H_2{}^{32}S$, $H_2{}^{34}S$, and $H_2{}^{33}S$, respectively. We only analyze emission from the so called hot core, but emission from the plateau, extended ridge, and/or compact ridge are also detected. Rotation diagrams for ortho and para H_2S follow straight lines given the uncertainties and yield $T_{rot} = 141 \pm 12$ K. This indicates H_2S is in LTE and is well characterized by a single kinetic temperature or an intense far-IR radiation field is redistributing the population to produce the observed trend. We argue the latter scenario is more probable and find that the most highly excited states ($E_{up} \gtrsim 1000$ K) are likely populated primarily by radiation pumping. We derive a column density, $N_{tot}(H_2{}^{32}S) = 9.5 \pm 1.9 \times 10^{17}$ cm^{-2}, gas kinetic temperature, $T_{kin} = 120 \pm^{13}_{10}$ K, and constrain the H_2 volume density, $n_{H_2} \gtrsim 9 \times 10^7$ cm^{-3}, for the H_2S emitting gas. These results point to an H_2S origin in markedly dense, heavily embedded gas, possibly in close proximity to a hidden self-luminous source (or sources), which are conceivably responsible for Orion KL's high luminosity. We also derive an H_2S ortho/para ratio of 1.7 ± 0.8 and set an upper limit for HDS/H_2S of $< 4.9 \times 10^{-3}$.

6.1.3 Chemical Implications

In Chapter 5, I presented some possible chemical implications based on our LTE model fits focusing on the complex organics. We identify the complex cyanides as well as NH_2CHO as systematically tracing hotter gas than traced by complex O-bearing organics. If these organics form predominantly on grain surfaces, then this may indicate that nitrogen bearing species are more difficult to remove from grain surfaces than O-bearing species. However, an origin in hot gas phase chemistry may also explain this dichotomy.

6.2 Future Prospects

High spatial resolution interferometric observations are required to understand both the physical and chemical structure of Orion KL. The analysis presented in this dissertation will help inform the most effective molecular tracers and transitions to help answer still outstanding questions concerning the source of Orion KL's high luminosity and chemical complexity. Advanced observing facilities such as ALMA will need to be employed to obtain observations with enough spatial resolution and sensitivity to address these questions. Specifically, among the > 90 H_2S transitions detected toward Orion KL in the HIFI survey, non-LTE modeling revealed that the $9_{7,2}$ – $9_{6,3}$ transition, which is available in ALMA band 9, is pumped by mid-IR radiation and requires continuum levels a factor of 8 times higher than observed. The source of this intense radiation field is presumably hot dust heated possibly by massive embedded protostars. ALMA maps of this highly excited transition will therefore trace those regions exposed to the strongest sources of hidden mid-IR radiation. Maps of lower energy lines, furthermore, will trace the global distribution of H_2S and provide context. If Orion KL is indeed heated internally by massive protostars, the sources identified by such observations may represent the origin of Orion KL's tremendous luminosity. We furthermore found that complex cyanides clearly traced hotter gas than complex oxygen bearing species toward both the hot core and compact ridge. The reason for this dichotomy remains unclear. High spacial resolution observations of

species such as CH_3OH, CH_3OCH_3 and CH_3CN, which trace gas toward both the hot core and compact ridge may thus shed light on different origin scenarios. Observing these species at high spatial resolution and sensitivity toward other massive hot cores will also provide a context for Orion KL.

In more general terms, this dissertation focusses on the analysis of a single broad band, line rich spectrum. The number of spectral lines present in this survey was unprecedented and required the development of methodologies that can be directly applied to similarly rich line surveys. Such datasets will become increasingly common in the "ALMA Era". Applying and building on these techniques will be a valuable resource going forward in the analysis and interpretation of these massive datasets.

APPENDICES

APPENDIX A

Individuals Who Worked on the Full Band Model

The individuals who participated in the full band analysis presented in Chapter 3 are listed below along with their current affiliations. The molecules listed next to each person are the species he or she principally modeled. This includes rarer isotopologues if they were detected for a given molecule. I participated in the modeling of all species. Some molecules are listed more than once because multiple people helped to model these species. If a molecule is not listed below, it was modeled only by me.

- Edwin Bergin (Univ. of Michigan) – C_2H_5CN and H_2O
- John H. Black (Chalmers Univ. of Technology) – H_2S
- Justin Neill (Univ. of Michigan) – CS, H_2O, NH_2, CH_2NH, C_2H_3CN, CH_3OH, NH_3, and H_2CO
- Cécile Favre (Univ. of Michigan) – CH_3OCHO
- Peter Schilke (Universität zu Köln) – C_2H_5OH
- Dariusz C. Lis (Caltech) – OCS and CH_3OCH_3
- Tom A. Bell (CSIC/INTA) – CH_3CN and NH_3
- Geoffrey Blake (Caltech) – HCl and H_2S
- José Cernicharo (CSIC/INTA) – HCN, HNC, HCO^+, SO_2, and SO
- Martin Emprechtinger (Caltech) – NH_2CHO and SiS
- Gisela B. Esplugues (CSIC/INTA) – SO_2 and SO

- Harshal Gupta (IPAC) – H_2CS, NO, and NS
- Maria Kleshcheva (Caltech) – H_2S
- Steven Lord (IPAC) – CS
- Nuria Marcelino (NRAO) – HCN, HNC, and HCO^+
- Brett A. McGuire (Caltech) – HCl
- John Pearson (JPL) – CH_3OH
- Thomas G. Phillips (Caltech) – HF
- Rene Plume (Univ. of Calgary) – CO and HCO^+
- Floris van der Tak (SRON) – H_2S
- Belén Tercero (CSIC/INTA) – HCN, HNC, HCO^+, SO_2, and SO
- Shiya Wang (Univ. of Michigan) – CH_3OH and H_2O
- Shanshan Yu (JPL) – HNCO, HCS^+, and H_2CCO

APPENDIX B

Reduced χ^2 Calculations for Chapter 3

We calculated reduced chi squared, $\chi^2_{\rm red}$, statistics for each model. This calculation was performed by first uniformly smoothing the data to a velocity resolution of $\sim$ 0.5 km/s. Residuals between the molecular fits and data were then computed by stepping across the spectrum in frequency intervals corresponding roughly to 1000 km/s. At each interval, we calculated the RMS noise level and subtracted a local baseline. For a channel to be included in the $\chi^2_{\rm red}$ calculation of a given molecular fit, the model emission had to be > 3 times the local RMS and responsible for 95% of the total flux when compared to the entire full band model. That is, the intensity ratio between the fit being considered and the full band model had to be ≥ 0.95 in order to avoid channels that contained emission from more than one molecule (i.e. blended lines). The uncertainty in each channel, σ_{tot}, was computed by adding in quadrature the contributions from several different sources of error,

$$\sigma_{tot} = \sqrt{\sigma_{bl}^2 + \sigma_{rms}^2 + \sigma_{cal}^2 + \sigma_{pt}^2 + \sigma_{bf}^2}. \tag{B.1}$$

Here, σ_{bl} is a baseline offset uncertainty, σ_{rms} is the local RMS noise level, σ_{cal} is the calibration uncertainty, σ_{pt} is the pointing error, and σ_{bf} is the error in beam filling factor brought on by the source size uncertainty. The method used to compute each error source is given below.

$\boldsymbol{\sigma_{bl}}$ – This represents offsets in the baseline that still existed despite having subtracted a baseline within each 1000 km/s interval. These offsets existed at approximately the 0.05 K level, we thus take $\sigma_{bl} = 0.05$ K.

$\boldsymbol{\sigma_{rms}}$ – This is the RMS noise level in the baseline. Emission line channels were

rejected by excluding channels predicted to be in emission by the full band model. We also used a sigma clip algorithm to remove any additional channels in emission from U lines.

$\boldsymbol{\sigma_{cal}}$ – We assume a 10% calibration uncertainty for each channel.

$\boldsymbol{\sigma_{pt}}$ – The pointing uncertainty was computed assuming a Gaussian beam and the nominal *Herschel* absolute pointing error (APE) of 2″ (Pilbratt et al., 2010). The percent error in the intensity of each channel brought on by the APE, δ_p, is thus,

$$\delta_p = 1 - exp\left[-\frac{APE^2}{2(\theta_b/2.355)^2}\right], \tag{B.2}$$

where θ_b is the beam size.

$\boldsymbol{\sigma_{bf}}$ – Because we did not vary the source size in our molecular fits, we include a beam filling factor uncertainty. We take the error in source size to be 30%. Assuming the shape of the telescope beam and source are Gaussian, the beam filling factor, η_{bf}, is,

$$\eta_{bf} = \frac{\theta_s^2}{\theta_s^2 + \theta_b^2}. \tag{B.3}$$

The beam filling factor is directly proportional to the observed intensity. Using the "error propagation equation" (Bevington & Robinson, 2003, their Eq. 3.13), we thus compute the percent error in the intensity of each channel, δ_{ss}, is

$$\delta_{ss} = 2\ \eta_{bf}(1 - \eta_{bf})\frac{\sigma_s}{\theta_s} \tag{B.4}$$

where σ_s is the error in the source size. Thus, σ_s / θ_s is the percent error in the source size (0.3).

APPENDIX C

Uncertainty Calculations for Chapter 4

All uncertainties were propagated using the standard "error propagation equation" (Bevington & Robinson, 2003, their Eq. 3.13) unless otherwise stated. The errors reported in Tables 4.1–4.3 for Δv, $\mathrm{T_{peak}}$, and $\int T_{\mathrm{mb}} d\mathrm{v}$ are those computed by the CLASS fitting algorithm. The uncertainties listed for $\mathrm{T_{peak}}$ are RMS measurements in the local baseline also calculated using CLASS. When propagating errors involving either $\mathrm{T_{peak}}$ or $\int T_{\mathrm{mb}} d\mathrm{v}$, we include a 10% calibration error and a pointing uncertainty. The pointing uncertainty is estimated using the following relation,

$$\Delta_p = 1 - exp\left[- \frac{\sigma_p^2}{2(\theta_b/2.355)^2} \right]. \tag{C.1}$$

Here, Δ_p is the percent error in either $\mathrm{T_{peak}}$ or $\int T_{\mathrm{mb}} d\mathrm{v}$ introduced by the telescope pointing error, σ_p, which we assume to be $2''$ (Pilbratt et al., 2010). In order to account for the calibration and pointing errors, we added the CLASS, calibration, and pointing uncertainties in quadrature before performing any further calculations involving $\mathrm{T_{peak}}$ or $\int T_{\mathrm{mb}} d\mathrm{v}$. We also estimate an uncertainty of $0.7''$ in our derived source size and a 30% error in the $\mathrm{N_{H_2}}$ estimate used to compute $\tau_{\mathrm{d}}(\nu)$ (see Sec. 4.3.2), both of which we include as sources of error in our computations of $\mathrm{N_{up}}$. The source size and $\mathrm{N_{H_2}}$ uncertainties were also added in quadrature with the RMS, calibration, and pointing errors when computing χ^2_{red} values for the model grids.

BIBLIOGRAPHY

Adande, G. R. & Ziurys, L. M. 2012, ApJ, 744, 194

Allen, D. A. & Burton, M. G. 1993, Nature, 363, 54

Asplund, M., Grevesse, N., Sauval, A. J., & Scott, P. 2009, ARA&A, 47, 481

Ball, C. D., Mengel, M., De Lucia, F. C., & Woon, D. E. 1999, J. Chem. Phys., 111, 8893

Bally, J., Cunningham, N. J., Moeckel, N., Burton, M. G., Smith, N., Frank, A., & Nordlund, A. 2011, ApJ, 727, 113

Becklin, E. E. & Neugebauer, G. 1967, ApJ, 147, 799

Bergin, E. A., et al. 2010, A&A, 521, L20

Beuther, H. & Nissen, H. D. 2008, ApJ, 679, L121

Beuther, H., et al. 2004, ApJ, 616, L31

Beuther, H., et al. 2005, ApJ, 632, 355

Beuther, H., et al. 2006, ApJ, 636, 323

Bevington, P. R. & Robinson, D. K. 2003, Data reduction and error analysis for the physical sciences

Bisschop, S. E., Jørgensen, J. K., van Dishoeck, E. F., & de Wachter, E. B. M. 2007, A&A, 465, 913

Blake, G. A., Mundy, L. G., Carlstrom, J. E., Padin, S., Scott, S. L., Scoville, N. Z., & Woody, D. P. 1996, ApJ, 472, L49

Blake, G. A., Sutton, E. C., Masson, C. R., & Phillips, T. G. 1987, ApJ, 315, 621

Boogert, A. C. A., Tielens, A. G. G. M., Ceccarelli, C., Boonman, A. M. S., van Dishoeck, E. F., Keane, J. V., Whittet, D. C. B., & de Graauw, T. 2000, A&A, 360, 683

Brouillet, N., et al. 2013, A&A, 550, A46

Buckle, J. V. & Fuller, G. A. 2003, A&A, 399, 567

Caselli, P., Hasegawa, T. I., & Herbst, E. 1993, ApJ, 408, 548

Charnley, S. B. 1997, ApJ, 481, 396

Charnley, S. B., Tielens, A. G. G. M., & Millar, T. J. 1992, ApJ, 399, L71

Chernin, L. M. & Wright, M. C. H. 1996, ApJ, 467, 676

Churchwell, E., Felli, M., Wood, D. O. S., & Massi, M. 1987, ApJ, 321, 516

Churchwell, E., Wood, D., Myers, P. C., & Myers, R. V. 1986, ApJ, 305, 405

Comito, C. & Schilke, P. 2002, A&A, 395, 357

Comito, C., Schilke, P., Phillips, T. G., Lis, D. C., Motte, F., & Mehringer, D. 2005, ApJS, 156, 127

Crockett, N. R., et al. 2010, A&A, 521, L21

Crockett, N. R., Bergin, E. A., Neill, J. L., Black, J. H., Blake, G. A., & Kleshcheva, M. 2013, ApJ, submitted

De Buizer, J. M., Morris, M. R., Becklin, E. E., Zinnecker, H., Herter, T. L., Adams, J. D., Shuping, R. Y., & Vacca, W. D. 2012, ApJ, 749, L23

de Graauw, T., et al. 2010, A&A, 518, L6

Dicker, S. R., et al. 2009, ApJ, 705, 226

Doi, T., O'Dell, C. R., & Hartigan, P. 2002, AJ, 124, 445

Dougados, C., Lena, P., Ridgway, S. T., Christou, J. C., & Probst, R. G. 1993, ApJ, 406, 112

Downes, D., Genzel, R., Becklin, E. E., & Wynn-Williams, C. G. 1981, ApJ, 244, 869

Faure, A., Crimier, N., Ceccarelli, C., Valiron, P., Wiesenfeld, L., & Dubernet, M. L. 2007, A&A, 472, 1029

Favre, C., Despois, D., Brouillet, N., Baudry, A., Combes, F., Guélin, M., Wootten, A., & Wlodarczak, G. 2011, A&A, 532, A32

Fontani, F., Pascucci, I., Caselli, P., Wyrowski, F., Cesaroni, R., & Walmsley, C. M. 2007, A&A, 470, 639

Friedel, D. N. & Snyder, L. E. 2008, ApJ, 672, 962

Garrod, R. T. & Herbst, E. 2006, A&A, 457, 927

Garrod, R. T., Weaver, S. L. W., & Herbst, E. 2008, ApJ, 682, 283

Genzel, R. & Stutzki, J. 1989, ARA&A, 27, 41

Gezari, D. Y., Backman, D. E., & Werner, M. W. 1998, ApJ, 509, 283

Gibb, E. L., Whittet, D. C. B., Boogert, A. C. A., & Tielens, A. G. G. M. 2004, ApJS, 151, 35

Goddi, C., Greenhill, L. J., Chandler, C. J., Humphreys, E. M. L., Matthews, L. D., & Gray, M. D. 2009a, ApJ, 698, 1165

Goddi, C., Greenhill, L. J., Humphreys, E. M. L., Chandler, C. J., & Matthews, L. D. 2011, ApJ, 739, L13

Goddi, C., Greenhill, L. J., Humphreys, E. M. L., Matthews, L. D., Tan, J. C., & Chandler, C. J. 2009b, ApJ, 691, 1254

Goicoechea, J. R., Pety, J., Gerin, M., Teyssier, D., Roueff, E., Hily-Blant, P., & Baek, S. 2006, A&A, 456, 565

Goldsmith, P. F., Bergin, E. A., & Lis, D. C. 1997, ApJ, 491, 615

Goldsmith, P. F., Krotkov, R., Snell, R. L., Brown, R. D., & Godfrey, P. 1983, ApJ, 274, 184

Goldsmith, P. F. & Langer, W. D. 1999, ApJ, 517, 209

Gómez, L., Rodríguez, L. F., Loinard, L., Lizano, S., Allen, C., Poveda, A., & Menten, K. M. 2008, ApJ, 685, 333

Gómez, L., Rodríguez, L. F., Loinard, L., Lizano, S., Poveda, A., & Allen, C. 2005, ApJ, 635, 1166

Greaves, J. S. & White, G. J. 1991, A&AS, 91, 237

Greenhill, L. J., Gezari, D. Y., Danchi, W. C., Najita, J., Monnier, J. D., & Tuthill, P. G. 2004a, ApJ, 605, L57

Greenhill, L. J., Gwinn, C. R., Schwartz, C., Moran, J. M., & Diamond, P. J. 1998, Nature, 396, 650

Greenhill, L. J., Reid, M. J., Chandler, C. J., Diamond, P. J., & Elitzur, M. 2004b, in IAU Symposium, Vol. 221, Star Formation at High Angular Resolution, ed. M. G. Burton, R. Jayawardhana, & T. L. Bourke, 155

Hatchell, J., Thompson, M. A., Millar, T. J., & MacDonald, G. H. 1998, A&A, 338, 713

Herbst, E. & Klemperer, W. 1973, ApJ, 185, 505

Herbst, E. & van Dishoeck, E. F. 2009, ARA&A, 47, 427

Hermsen, W., Wilson, T. L., Walmsley, C. M., & Henkel, C. 1988, A&A, 201, 285

Herpin, F., Marseille, M., Wakelam, V., Bontemps, S., & Lis, D. C. 2009, A&A, 504, 853

Hildebrand, R. H. 1983, QJRAS, 24, 267

Ho, P. T. P., Barrett, A. H., Myers, P. C., Matsakis, D. N., Chui, M. F., Townes, C. H., Cheung, A. C., & Yngvesson, K. S. 1979, ApJ, 234, 912

Irvine, W. M., Goldsmith, P. F., & Hjalmarson, A. 1987, in Astrophysics and Space Science Library, Vol. 134, Interstellar Processes, ed. D. J. Hollenbach & H. A. Thronson, Jr., 561–609

Jacq, T., Walmsley, C. M., Henkel, C., Baudry, A., Mauersberger, R., & Jewell, P. R. 1990, A&A, 228, 447

Jewell, P. R., Hollis, J. M., Lovas, F. J., & Snyder, L. E. 1989, ApJS, 70, 833

Johansson, L. E. B., Andersson, C., Ellder, J., Friberg, P., Hjalmarson, A., Hoglund, B., Irvine, W. M., Olofsson, H., & Rydbeck, G. 1984, A&A, 130, 227

Kleinmann, D. E. & Low, F. J. 1967, ApJ, 149, L1+

Lee, C. W. & Cho, S.-H. 2002, Journal of Korean Astronomical Society, 35, 187

Lee, C. W., Cho, S.-H., & Lee, S.-M. 2001, ApJ, 551, 333

Lerate, M. R., et al. 2006, MNRAS, 370, 597

Lonsdale, C. J., Becklin, E. E., Lee, T. J., & Stewart, J. M. 1982, AJ, 87, 1819

Menten, K. M. & Reid, M. J. 1995, ApJ, 445, L157

Menten, K. M., Reid, M. J., Forbrich, J., & Brunthaler, A. 2007, A&A, 474, 515

Menten, K. M. & Wyrowski, F. 2011, Springer Tracts in Modern Physics, 241, 27

Millar, T. J., Herbst, E., & Charnley, S. B. 1991, ApJ, 369, 147

Minh, Y. C., Irvine, W. M., McGonagle, D., & Ziurys, L. M. 1990, ApJ, 360, 136

Minh, Y. C., Irvine, W. M., & Ziurys, L. M. 1989, ApJ, 345, L63

Minh, Y. C., Ziurys, L. M., Irvine, W. M., & McGonagle, D. 1991, ApJ, 366, 192

Mitchell, G. F. 1984, ApJ, 287, 665

Müller, H. S. P., Schlöder, F., Stutzki, J., & Winnewisser, G. 2005, Journal of Molecular Structure, 742, 215

Müller, H. S. P., Thorwirth, S., Roth, D. A., & Winnewisser, G. 2001, A&A, 370, L49

Mundy, L. G., Scoville, N. Z., Baath, L. B., Masson, C. R., & Woody, D. P. 1986, ApJ, 304, L51

Neill, J. L., Wang, S., Bergin, E. A., Crockett, N. R., Favre, C., Plume, R., & Melnick, G. J. 2013, ArXiv e-prints

Nissen, H. D., Cunningham, N. J., Gustafsson, M., Bally, J., Lemaire, J.-L., Favre, C., & Field, D. 2012, A&A, 540, A119

Nissen, H. D., Gustafsson, M., Lemaire, J. L., Clénet, Y., Rouan, D., & Field, D. 2007, A&A, 466, 949

O'dell, C. R. 2001, ARA&A, 39, 99

Okumura, S.-I., Yamashita, T., Sako, S., Miyata, T., Honda, M., Kataza, H., & Okamoto, Y. K. 2011, PASJ, 63, 823

Olofsson, A. O. H., et al. 2007, A&A, 476, 791

Ossenkopf, V. & Henning, T. 1994, A&A, 291, 943

Ott, S. 2010, in Astronomical Society of the Pacific Conference Series, Vol. 434, Astronomical Data Analysis Software and Systems XIX, ed. Y. Mizumoto, K.-I. Morita, & M. Ohishi, 139

Palumbo, M. E., Geballe, T. R., & Tielens, A. G. G. M. 1997, ApJ, 479, 839

Palumbo, M. E., Tielens, A. G. G. M., & Tokunaga, A. T. 1995, ApJ, 449, 674

Peng, T.-C., Despois, D., Brouillet, N., Parise, B., & Baudry, A. 2012, A&A, 543, A152

Persson, C. M., et al. 2007, A&A, 476, 807

Phillips, T. G. 1987, in Astrophysics and Space Science Library, Vol. 134, Interstellar Processes, ed. D. J. Hollenbach & H. A. Thronson, Jr., 707–730

Phillips, T. G., et al. 2010, A&A, 518, L109

Pickett, H. M., Poynter, I. R. L., Cohen, E. A., Delitsky, M. L., Pearson, J. C., & Muller, H. S. P. 1998, Journal of Quantitative Spectroscopy and Radiative Transfer, 60, 883

Pilbratt, G. L., et al. 2010, A&A, 518, L1

Pineau des Forets, G., Roueff, E., Schilke, P., & Flower, D. R. 1993, MNRAS, 262, 915

Plambeck, R. L., Wright, M. C. H., Friedel, D. N., Widicus Weaver, S. L., Bolatto, A. D., Pound, M. W., Woody, D. P., Lamb, J. W., & Scott, S. L. 2009, ApJ, 704, L25

Plume, R., et al. 2012, ApJ, 744, 28

Rieke, G. H., Low, F. J., & Kleinmann, D. E. 1973, ApJ, 186, L7

Robberto, M., Beckwith, S. V. W., Panagia, N., Patel, S. G., Herbst, T. M., Ligori, S., Custo, A., Boccacci, P., & Bertero, M. 2005, AJ, 129, 1534

Rodgers, S. D. & Charnley, S. B. 2001, ApJ, 546, 324

Rodríguez, L. F., Poveda, A., Lizano, S., & Allen, C. 2005, ApJ, 627, L65

Roelfsema, P. R., et al. 2012, A&A, 537, A17

Schilke, P., Benford, D. J., Hunter, T. R., Lis, D. C., & Phillips, T. G. 2001, ApJS, 132, 281

Schilke, P., Groesbeck, T. D., Blake, G. A., & Phillips, T. G. 1997, ApJS, 108, 301

Schöier, F. L., van der Tak, F. F. S., van Dishoeck, E. F., & Black, J. H. 2005, A&A, 432, 369

Schultz, A. S. B., Colgan, S. W. J., Erickson, E. F., Kaufman, M. J., Hollenbach, D. J., O'dell, C. R., Young, E. T., & Chen, H. 1999, ApJ, 511, 282

Scoville, N. Z. & Kwan, J. 1976, ApJ, 206, 718

Shuping, R. Y., Morris, M., & Bally, J. 2004, AJ, 128, 363

Smith, D. 1992, Chemical Reviews, 92, 1473

Smith, R. G. 1991, MNRAS, 249, 172

Stolovy, S. R., et al. 1998, ApJ, 492, L151

Sutton, E. C., Blake, G. A., Masson, C. R., & Phillips, T. G. 1985, ApJS, 58, 341

Sutton, E. C., Peng, R., Danchi, W. C., Jaminet, P. A., Sandell, G., & Russell, A. P. G. 1995, ApJS, 97, 455

Tercero, B., Cernicharo, J., Pardo, J. R., & Goicoechea, J. R. 2010, ArXiv e-prints

Tercero, B., Vincent, L., Cernicharo, J., Viti, S., & Marcelino, N. 2011, A&A, 528, A26

Tieftrunk, A., Pineau des Forets, G., Schilke, P., & Walmsley, C. M. 1994, A&A, 289, 579

Turner, B. E. 1989, ApJS, 70, 539

van der Tak, F. F. S., Black, J. H., Schöier, F. L., Jansen, D. J., & van Dishoeck, E. F. 2007, A&A, 468, 627

van der Tak, F. F. S., Boonman, A. M. S., Braakman, R., & van Dishoeck, E. F. 2003, A&A, 412, 133

van Dishoeck, E. F., Wright, C. M., Cernicharo, J., Gonzalez-Alfonso, E., de Graauw, T., Helmich, F. P., & Vandenbussche, B. 1998, ApJ, 502, L173

Vogel, S. N., Wright, M. C. H., Plambeck, R. L., & Welch, W. J. 1984, ApJ, 283, 655

Wang, K.-S., Kuan, Y.-J., Liu, S.-Y., & Charnley, S. B. 2010, ApJ, 713, 1192

Wang, S., et al. 2011, A&A, 527, A95

Watson, W. D. 1973, ApJ, 183, L17

Werner, M. W., Capps, R. W., & Dinerstein, H. L. 1983, ApJ, 265, L13

White, G. J., Araki, M., Greaves, J. S., Ohishi, M., & Higginbottom, N. S. 2003, A&A, 407, 589

Wilson, T. L., Gaume, R. A., Gensheimer, P., & Johnston, K. J. 2000, ApJ, 538, 665

Wright, M., Sandell, G., Wilner, D. J., & Plambeck, R. L. 1992, ApJ, 393, 225

Wright, M. C. H., Plambeck, R. L., & Wilner, D. J. 1996, ApJ, 469, 216

Wright, M. C. H. & Vogel, S. N. 1985, ApJ, 297, L11

Wynn-Williams, C. G., Genzel, R., Becklin, E. E., & Downes, D. 1984, ApJ, 281, 172

Zapata, L. A., Schmid-Burgk, J., Ho, P. T. P., Rodríguez, L. F., & Menten, K. M. 2009, ApJ, 704, L45

Zapata, L. A., Schmid-Burgk, J., & Menten, K. M. 2011, A&A, 529, A24

Zernickel, A., et al. 2012, A&A, 546, A87

Ziurys, L. M. & McGonagle, D. 1993, ApJS, 89, 155